DOCTORAL DISSERTATION

Numerical simulation methods for flow resistance and sediment transport dynamics in curved and meandering rivers

[湾曲・蛇行河川における流下抵抗と土砂輸送力学の数値解析法]

March 2024

Department of Civil and Environmental Engineering

Graduate School of Advanced Science and Engineering

Hiroshima University

FIKRY PURWA LUGINA

Acknowledgements

I would like to express my deepest gratitude to all those who have contributed to the completion of this doctoral thesis. This journey has been both challenging and rewarding, and I could not have reached this milestone without the support and assistance of many individuals and institutions.

First and foremost, I am indebted to my supervisor, Uchida Sensei, for his unwavering guidance, patience, and expertise throughout this research endeavor. His mentorship has been instrumental in shaping the direction of my work and in nurturing my growth as a researcher.

I am also grateful to the members of my laboratory professors, Kawahara Sensei, Inoue Sensei and Hatono Sensei, for their valuable insights, critical feedback, and encouragement. Their collective expertise has enriched the quality of this thesis.

My appreciation extends to my colleagues and fellow researchers at Hydraulic Laboratory of Hiroshima University, whose stimulating discussions have made this academic journey all the more fulfilling. I would like to express my sincere gratitude to our diligent laboratory secretary, Mizunuma-san, for her invaluable support and organizational prowess. Your efficiency and dedication have significantly contributed to the smooth operation of my research endeavors. I would like to acknowledge the research funding provided by MEXT, which supported my studies and allowed me to carry out this research.

To my friends and family, I offer my heartfelt thanks for their unwavering support, understanding, and encouragement during this challenging period. Their belief in me sustained my motivation and kept me moving forward.

Lastly, I extend heartfelt gratitude to my parents and wife, Madam Taqiyya, for their unwavering love, encouragement, and unwavering support. Your belief in me fuels my journey, and I am grateful for the strength and joy you bring to my life.

Thank you all for being a part of this remarkable chapter in my life.

Fikry Purwa Lugina

February 2024

Hiroshima, Japan

Abstract

Flooding can be caused by more than just heavy rainfall; it can happen when the volume rate of flood water surpasses the river's capacity. Sediment transport dynamics trigger rivers' shape to change, it can be riverbed's elevation and/or river narrowing, and it will promote the decreased river capacity. When river capacity decreases, its response to flow rate/discharge becomes more prone to flooding.

Flow resistance plays a crucial role in governing the behavior of water in streams and rivers, significantly impacting flow hydraulics. It directly influences the ability of a channel to carry water by affecting the velocity of the flow and, consequently, the depth of the water. Additionally, flow resistance has a direct influence on the distribution of shear stress along the channel boundary, which, in turn, affects the extent and pattern of erosion on the channel bed and banks.

Numerical models, validated through experiments or observational datasets, prove to be cost-effective tools. While a three-dimensional (3D) numerical model is preferable for capturing complex flow patterns in meandering rivers, many such models are susceptible to numerical instability and demand substantial computational resources. Consequently, hydraulic engineers often favor simpler two-dimensional (2D) depth-averaged or one-dimensional (1D) cross-section-averaged models for practical applications. However, these models lack the capability to depict the vertical flow distribution of streamwise and transverse velocity characteristic of meandering river flows.

This study: (1) investigated flow resistance and sediment transport dynamics in meandering rivers to get a comprehensive understanding of decreased river capacity mechanisms; (2) developed a numerical model with both efficient calculation time and high accuracy. The work was divided

into three parts: developing numerical models, investigating flow resistance, and investigating sediment dynamics.

In the first part, a high momentum transfer near the wall was found by incorporating shallow water assumption for flow dynamics investigation in curved open channels. In a channel bend, the momentum transfer is attributed to the vertical velocity distribution in transverse direction. The vertical velocity distribution is frequently disregarded by a two-dimensional model, leading to inaccuracies in the main velocity distribution. The evaluation of the dispersion term becomes increasingly crucial for calculating momentum transfer attributed to the vertical velocity distribution, surpassing the importance of the advection term. In simpler terms, an incorrect discretization of the dispersion term can lead to unphysical solutions similar to those arising from the advection term, considering that the dispersion term originates from the advection term.

This study developed a numerical discretization method of an upwind scheme for dispersion terms to overcome unphysical phenomena with the shallow water assumption. The proposed method was then applied to a quasi-three-dimensional numerical, so-called bottom velocity calculation (BVC), method to investigate its applicability in reproducing flow structures. . The BVC method evaluates velocity on the bed coupled with depth-integrated continuity and horizontal momentum equations with additional equations of depth-integrated horizontal vorticity equations, momentum equations of the water surface, double integrated continuity equation over depth, and depth-integrated vertical momentum equation for non-hydrostatic pressure distribution. There are several types of BVC models employed in this study: (1) The SBVC (simplified bottom velocity calculation) method with shallow water assumption that employs hydrostatic pressure distribution and neglects the variation in vertical velocity. The SBVC2 model assumes the equilibrium

condition of water surface flow, while SBVC3 calculates the momentum equations for water surface flows. (2) The GBVC3 (general bottom velocity calculation) model is not restricted to the shallow water assumption and calculates the non-hydrostatic pressure distribution and variation in vertical velocity.

The effectivity of the proposed method was then compared to a conventional two-dimensional model and a fully three-dimensional model into sharply and mildly curved channels dataset. The proposed method effectively mitigated the occurrence of excessively high velocities near the wall. It demonstrated the capability to accurately replicate both the experimental water levels and velocity profiles within the channel bend using the experimental dataset. Furthermore, it exhibited strong agreement with the results obtained from a fully three-dimensional model. While the conventional two-dimensional model cannot predict well the water surface profile in curved channel because of the inability to consider the increase in flow resistance due to secondary flow. In addition, even with modified roughness coefficients to reproduce the increased channel resistance, the conventional two-dimensional model underestimated the water surface elevation along the outer bank.

After confirming the applicability of the method with the discretization scheme in dispersion terms, the models were then extended to be applied to the bed profile case. The BVC models results show a variation, at some cross-section there is a good agreement between BVC models, experimental dataset, and the three-dimensional model, but at some cross-section not. For overall qualitative results, BVC models are rather good compared to experimental dataset and the three-dimensional model.

For the second part, this study investigated the flow resistance resulting from shear forces in meandering channels, by integrating laboratory experiments with numerical models featuring uniform width and rectangular cross-sections. The study specifically concentrates on distortion resistance and skin resistance, while excluding the consideration of spill resistance and form drag effects. The study has two primary objectives. Firstly, to examine the impact of channel shape, aspect ratios, and bed roughness on flow resistance through laboratory experiments. In this study, a combination of factors was explored to gain a more comprehensive understanding of flow resistance. Secondly, the study aims to validate the effectiveness of the BVC method in simulating the impact of different factors on flow resistance and to investigate flow resistance in channels with different sinuosity.

Laboratory experiments and numerical model simulation were conducted to explore diverse factors influencing flow resistance. To analyze the impact of channel shape on flow resistance, experiments were conducted on both straight and meandering channels. To assess the influence of aspect ratio on flow resistance, four cases with varying aspect ratios (ranging from 2.6 to 7.0) were examined. The effect of bed roughness on flow resistance was investigated by implementing two bed conditions: a smooth concrete bed and a rough gravel bed with a particle size of 5-10 mm. The investigation into different sinuosities was carried out after validating the numerical method with experimental data.

The meandering channels exhibit higher friction factors compared to straight channels, indicating a greater resistance in meandering channels. This increase in friction factor can be attributed to the additional transverse bed shear stress component and the advective momentum transport in the vertical direction caused by secondary flow, these factors increase the velocity near

the bed and increase bed shear stress. The friction factor for smooth bed conditions decreases gradually with increasing the aspect ratio due to the decreasing in the side wall shear stress. On the other hand, in the case of rough bed conditions, the friction factor tends to rise as aspect ratio increases. This is attributed to the increase in relative roughness height as the aspect ratio increases with decreasing water depth. The larger the relative roughness height, the more dominant role bed roughness plays in determining flow resistance compared to distortion resistance.

The BVC models were in good agreement to replicate both water surface elevation and flow resistance caused by secondary flow. Meanwhile, the 2D model cannot predict well the water surface elevation and flow resistance because of the inability to consider the increase in flow resistance due to secondary flow. As for velocity distribution validation, laboratory experiment and numerical model experiment were combined. Velocity distribution close to the channel bed was measured using an Acoustic Doppler Velocimeter (ADV) (SonTek 16-MHz MicroADV), while a 3D model was applied to describe velocity close to the water surface.

Once the model validation was confirmed to be in good agreement with the experimental results, the next step involved using the models to estimate the impact of channel sinuosity on flow resistance. The numerical investigation demonstrated that as sinuosity increased, flow resistance also increased until reaching a sinuosity value of 1.75. However, beyond this point, flow resistance started to decrease. This phenomenon can be attributed to the strengthening of secondary flow, whereby a smaller curvature ratio value resulted in a more pronounced secondary flow. The numerical investigation revealed that even the 2D model can capture the increase in flow resistance caused by the distortion effect arising from the distribution of depth-averaged velocity.

And the final part, we discussed sediment transport dynamics in curved and meandering channels with sediment supply condition. Application of quasi-3D models for sediment transport analysis is still limited to simple cases, in which curved open channel and without sediment supply condition. In spite of this, the consideration of more complex channel shapes and conditions is critical, e.g., sediment-flood disasters in Japan as a result of heavy precipitation in 2018. Therefore, this research aims to investigate the applicability of quasi-3D models to predict bed deformation in meandering channel with excessive sediment supply. The models of the BVC method were validated with three different cases, strongly curved channel, mild slope meandering channel, and steep slope meandering channel. The result showed that three-dimensional flow structures have a significant role in distributing sediment in curved and meandering channels. The numerical investigation confirmed that the BVC models' results are in good agreement with experiment dataset in terms of predicting the location of scouring and deposition, however they failed to represent the magnitude of scouring and deposition.

Contents

List of Figures

List of Tables

Chapter 1 Introduction

1.1 Literature review

Rivers have long been an essential part of human life, providing crucial resources such as water for drinking, irrigation for agriculture, transportation through inland navigation, and recreational activities (Da Silva & Ebrahimi, 2017; Rhoads, 2020). Moreover, rivers play a crucial role in sustaining diverse riparian corridors and supporting aquatic life, thereby making a significant contribution to the conservation of biodiversity (Graziano et al., 2022; Naiman et al., 1993). These riverine ecosystems serve as habitats for a broad spectrum of plant and animal species, encompassing fish, amphibians, reptiles, birds, and mammals. The presence of riparian vegetation along riverbanks plays a crucial role in soil stabilization, erosion prevention, and acting as a buffer against floods. The intricate connections between rivers and their surrounding ecosystems foster ecological balance, contributing to the overall well-being and health of the environment.

However, rivers also present practical challenges and raise scientific inquiries due to their dynamic nature. Flooding, sedimentation, and changes in flow patterns can impact human settlements and infrastructure located near river systems. In the 20th century, floods claimed the lives of 6.8 million people worldwide, making them the primary cause of natural disaster fatalities. Asia, which experienced the highest number of flood-related deaths, accounted for approximately half of the fatalities during the last 25 years of the century. (Doocy et al., 2013; Jonkman, 2005). Addressing these challenges requires a multidisciplinary approach, involving engineers and

scientists who study the hydraulic behavior of rivers, sediment transport, flood management, and river restoration techniques.

Floodings are not solely triggered by heavy rainfall; it can occur when the flood discharge exceeds river capacity to convey water (Slater et al., 2015, 2019). The risk of flooding can be intensified by an increase in the occurrence of high flood discharge or a decrease in the river's capacity (Stover & Montgomery, 2001). Conversely, factors such as changes in the riverbed's elevation (Slater & Singer, 2013), alterations in the width of riverbanks (Singer, 2010), or variations in flow velocity due to changes in sediment texture or vegetation within the channel can influence the river's capacity (Garssen et al., 2017). Even if the frequency of flow remains constant, reductions in channel capacity can amplify the hazards associated with flooding.

1.1.1 Flow resistance

Flow resistance plays a pivotal role in shaping the dynamics of water in streams and rivers, exerting a substantial impact on flow hydraulics. It directly shapes a channel's capacity to transport water by influencing the flow velocity and, consequently, the water depth (Powell, 2014; Rhoads, 2020; Yen, 2002). Furthermore, the resistance to flow directly impacts the distribution of shear stress along the channel boundary, consequently shaping the scale and pattern of erosion on both the channel bed and banks.

Understanding flow resistance is essential for various applications, such as predicting the flow-stage relation and flood propagation in rivers (Uchida et al., 2014), evaluate flood risk (Khatua et al., 2012; Nezhad et al., 2022), and to design effective hydraulic structures (Ghaderi et al., 2021; Saghebian et al., 2020). Furthermore, flow resistance is vital in studying the dynamics of stream channels from a geomorphological, sedimentological, and engineering perspective. It

provides insights into the formation, stability, and adjustment of channel shape and helps assess the potential for erosion and sediment transport (Ferguson, 2010; Gladkov et al., 2021; Latosinski et al., 2022; Palucis et al., 2018; Rhoads, 2020).

Flow resistance in open channels exhibits similar characteristics to flow resistance in closed pipes (Henderson, 1966; Leopold et al., 1960), and it can be categorized into three primary types: distortion resistance, skin resistance, and spill resistance (Leopold et al., 1960; Powell, 2014; Yen, 2002). Distortion resistance arises when the flow encounters a boundary feature like a bend in the channel, causing the flow to deviate from its original direction. This results in the formation of secondary flow structures that increase the shear stress on the channel bottom. Skin resistance, on the other hand, occurs due to the interaction between the flowing water and the boundary surfaces such as the channel walls, riverbed, or riverbanks. Spill resistance is associated with sudden velocity reductions, such as at the point where a partially opened valve in a piping system expands or at the base of a waterfall in open-channel flow.

From a momentum perspective, flow resistance is defined as the force per unit area exerted on the boundaries of rivers. This resistance comprises surface drag caused by shear forces and form drag resulting from pressure forces in fluid mechanics (Rouse, 1978). However, the explanation of flow resistance components can become ambiguous due to the concept of energy dissipation, which adds complexity to the understanding of these components.

Flow resistance plays a crucial role in determining three important factors: flow velocity (V), flow depth (H), and friction or energy slope (S_f). To establish the relationship between flow resistance and these parameters, specific equations, known as flow resistance equations, are utilized. These equations are typically formulated assuming uniform, steady flow conditions. In the

field of Earth Sciences, three commonly employed flow resistance equations are the Manning equation (Equation 1.1), the Darcy-Weisbach equation (Equation 1.2), and the Chezy equation (Equation 1.3). These equations provide valuable tools for analyzing and quantifying flow resistance in various natural systems.

$$V = \frac{R^{2/3} S_f^{1/2}}{n} \tag{1.1}$$

$$V = \sqrt{\frac{8g}{f}} \sqrt{RS_f} \tag{1.2}$$

$$V = C\sqrt{RS} \tag{1.3}$$

in which n, f, and C are the Manning, Weisbach, and Chezy resistance coefficients, respectively; R: hydraulic radius, S_f: slope, g: gravitational acceleration.

1.1.2 Flow dynamics in curved and meandering rivers

The study of flow dynamics in curved and meandering rivers holds considerable significance in hydraulic and environmental engineering. A comprehensive understanding of the flow characteristics is essential for diverse applications, ranging from river management and flood control to ecological restoration (Lave et al., 2010; Palmer et al., 2005). These flow attributes exert a profound influence on the channel morphology, sediment transport, and overall hydraulic performance of the river system (Abad & Garcia, 2009a, 2009b; Engel & Rhoads, 2017).

Curved and meandering rivers display unique flow patterns and structures in contrast to straight channels. In straight channels, secondary flows mainly arise from the non-uniformity and anisotropy of turbulence (Nezu & Nakagawa, 1993; Yang et al., 2012). Consequently, these flows are present only in turbulent conditions, with their intensity typically being relatively weak.

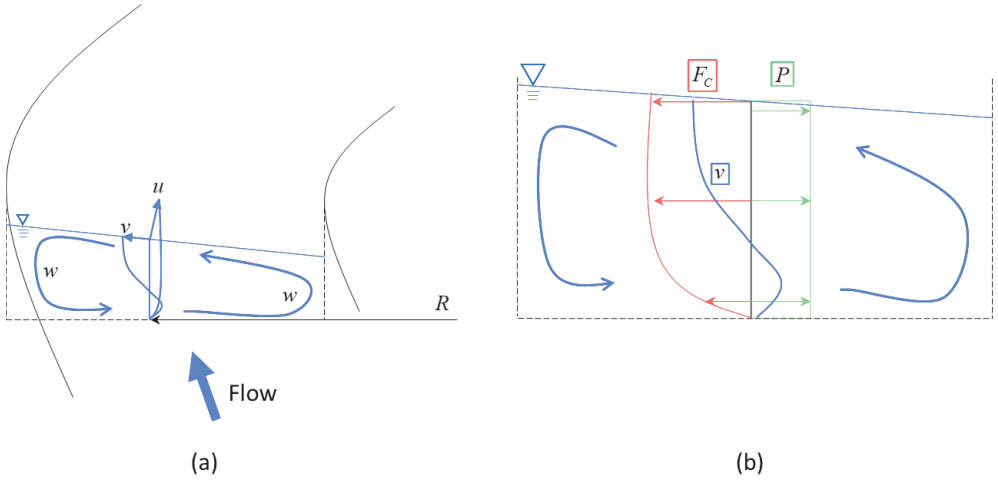

Figure 1.1 Flow structures in curved and meandering rivers: (a) Three-dimensional flow structures; (b) Schematic representation of secondary flow

Conversely, in channel bends, secondary flows primarily generated from a combination of pressure gradients and centrifugal forces. (Blanckaert & De Vriend, 2003, 2004, 2010; Da Silva & Ebrahimi, 2017; Pan et al., 2022; C. G. Song et al., 2012; Yan et al., 2020).

Figure 1.1 shows flow structures in curved and meandering rivers, (a) shows three-dimensional flow structures, in which u, v, w are streamwise, transverse, and vertical velocity while (b) shows a schematic representation of secondary flow, in which transverse velocity distribution. The secondary flow velocity component, v, is generated perpendicular to the primary flow direction due to the centrifugal acceleration, $F_C = \rho u^2 / R$, resulting from channel curvature, in which R is channel curvature. In contrast, the streamwise velocity component, u, varies from zero at the channel bed to a maximum near the water surface, leading to a radially outward centrifugal force that is greatest at the surface and diminishes towards the bed. This force, along with the hydrostatic pressure gradient, which is constant due to the assumed hydrostatic pressure

distribution, creates a net radial force that changes direction at a specific depth within the flow. This net force imbalance is the primary driver of the secondary flow.

The aspect ratio divides open-channel flows into two distinct categories: narrow and wide (Nezu & Nakagawa, 1993). Narrow channels $\left(B/H \leq 5\right)$, defined by pronounced recirculation zones at both the surface and bottom, exhibit a unique flow pattern that concentrates energy and momentum towards the center and redistributes it downward. This contrasts with wider channels $\left(B/H > 5\right)$, where recirculation effects are weaker and secondary flows less prominent (Kashyap et al., 2012).

The strength of secondary flow is also influenced by the radius of curvature $\left(R/B\right)$ (Kashyap et al., 2012). The curvature radius plays a crucial role in determining the nature of a bend, whether it is high $\left(R/B < 2.5\right)$ or moderate $\left(R/B > 2.5\right)$. In bends characterized by a high curvature radius, the area with increased streamwise velocities is located near the inner bank, close to the bend's entrance. On the other hand, in channels with milder curvature, the zone of high streamwise velocities does not reach the inner bank; instead, it persists along the outer bank for a considerable length of the channel.

1.1.3 Sediment transport and bed topography in curved and meandering rivers

The occurrence of transverse super-elevation at bends, induced by centrifugal acceleration, not only crucially contributes to the creation of secondary flow but also affects changes in bed shear stress and velocity distribution (Blanckaert & De Vriend, 2010; Engel & Rhoads, 2017; Rhoads, 2020). The outer bank of a meander bend typically experiences higher flow velocities, while the inner bank has lower velocities. The increased flow velocity along the outer bank results

in higher bed shear stress on the riverbed that triggers erosion to occur on the outer bank, and sediment is picked up and transported downstream. On the inner bank, the lower flow velocities lead to reduced bed shear stress. Consequently, sediment transport capacity decreases, and sediment may be deposited, leading to the formation of point bars.

The bed topography of meandering rivers is constantly changing due to the movement of sediment (Dietrich et al., 1979). Point bars and pools migrate downstream, and the channel itself migrates laterally (Nanson, 1980). This migration is caused by the erosion of sediment from the convex bank and the deposition of sediment on the concave bank. The migration of the channel can have a significant impact on the surrounding landscape. For example, it can cause the formation of oxbow lakes, which are abandoned meanders that have been filled with sediment (Schwenk & Foufoula-Georgiou, 2016).

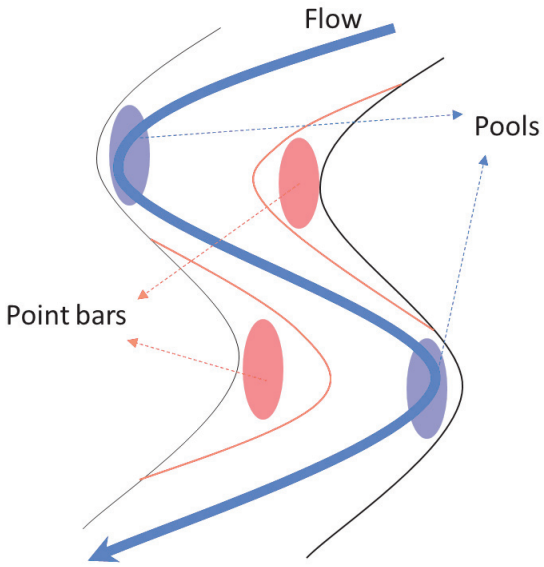

Figure 1.2 Meandering river's planform with the existence of pools and point bars

The sediment movement and bed topography in curved and meandering rivers play crucial roles in shaping the ecology and hydrology of these environments. The development of point bars and pools creates habitats for diverse aquatic organisms. Additionally, the shifting channel can modify the river's flow patterns and water quality, impacting factors such as cross-sectional area, water velocity, and sediment transport (Amoros, 2001; Kobayashi et al., 2022; Poff et al., 1997; Poole, 2002).

1.1.4 Numerical calculation method in fluvial dynamics

The study of river dynamics has seen a significant increase in focus due to advancements in measurement equipment (Abad & Garcia, 2009a, 2009b; Blanckaert, 2010; Termini, 2009a) and computer technology (Van Balen et al., 2010; Zeng, Constantinescu, Blanckaert, et al., 2008; Zeng, Constantinescu, & Weber, 2008). While direct measurements and experiments were the most accurate methods for understanding physical processes, numerical models have proven to be valuable tools for exploring flow characteristics with developments in computer technology and numerical models. These models have enabled researchers to solve complex equations that govern flow and connect advanced hydrodynamic models with sediment-transport and morphodynamic models, allowing for the analysis of meandering bed deformation and planimetric evolution in rivers (Motta et al., 2012; Rüther & Olsen, 2007; Vasquez et al., 2008, 2011).

The dynamics of natural river systems involve complex interactions between the three-dimensional (3D) flow field, sediment transport, and bathymetry. An essential element of this complexity is the existence of secondary flow structures, which wield considerable influence in redistributing velocity, affecting boundary shear stress and sediment transport, shaping bathymetry, and influencing the dispersion and mixing of suspended substances such as contaminants or

nutrients. A thorough comprehension and precise prediction of the 3D flow, sediment transport, and bathymetry hold immense importance in various applications of river engineering and management. This encompasses the design of river restoration projects, optimization of navigation routes, and enhancement of the ecological functions of rivers.

To achieve accurate predictions in curved sections of channels, it is preferable to use 3D numerical models that capture the intricate secondary flow patterns within the bends (Zeng, Constantinescu, Blanckaert, et al., 2008; Zeng, Constantinescu, & Weber, 2008). However, many 3D models are prone to numerical instability and require significant computational resources. As a result, hydraulic engineers often opt for two-dimensional (2D) depth-averaged (Duc et al., 2004; Wu, 2004) or one-dimensional (1D) cross-section-averaged (Nistoran et al., 2017) models, which are simpler to implement and widely applicable in practical applications.

One of the most advanced models for the simulation of flow and sediment transport in shallow water is DELFT3D and its 2D depth-average subsystem for river flow and morphological changes (Langendoen, 2001). A model that has similar features is the 2D curvilinear finite difference model MIKE21C which has been developed at the Danish Hydraulic Institute (DHI) for simulation of flow, sediment transport, and river morphology (Langendoen, 2001). In this model, the effects of secondary flow in curved channels are taken into account by introducing a so-called quasi-3D approach. A useful comparison of most of the models mentioned can be found in (2001) who gives a fairly detailed description of their features and evaluates them based on these features. A direct comparison of the model performance is, however, not included.

The crucial attributes of numerical models encompass accuracy, consistency, stability, and convergence, as outlined by Wu (2008). Accuracy refers to the ability to closely approximate the

exact solution, thereby minimizing errors arising from modeling, discretization, and iteration. Consistency entails ensuring that the system of discretized equations aligns with the original differential equation, such that the disparity between the exact and discretized equations approaches zero as the grid size and time step decrease. Stability is characterized by diminishing errors during the numerical solution process, where methods that avoid divergence are deemed stable. Convergence is attained when the solution of the discretized algebraic equations progressively approaches the exact solution of the original differential equation for each dependent variable.

The preservation of conservation properties, such as momentum transfer, is fundamental in numerical models, and it is crucial for the discretization scheme to uphold this characteristic. However, the discretization process often leads to numerical oscillations and a loss of stability properties compared to the continuous problem. To address these challenges, various numerical methods have been developed, including the finite difference method (FDM), finite element method (FEM), and finite volume method (FVM). Among these approaches, the finite volume method (FVM) has gained significant popularity as an efficient technique for discretizing partial differential equations (Hermeline, 2000; Manzini & Russo, 2008).

1.2 Research objectives

Figure 1.3 shows a conceptual model, (a) shows the interplay among variables accounted in this study. The general idea of this study is to gain a comprehensive understanding of flood management. From the literature review, we can notice that a flooding is not only triggered by a heavy rainfall event but also triggered due to the decreased river capacity. Sediment transport dynamics trigger rivers' shape to change, it can be riverbed's elevation and/or river narrowing, and it will promote the decreased river capacity. When river capacity decreases, its response to flow rate/discharge becomes more prone to flooding. Understanding the impact of flow resistance becomes crucial for predicting both flow-stage and the propagation of floods within a river. Hence,

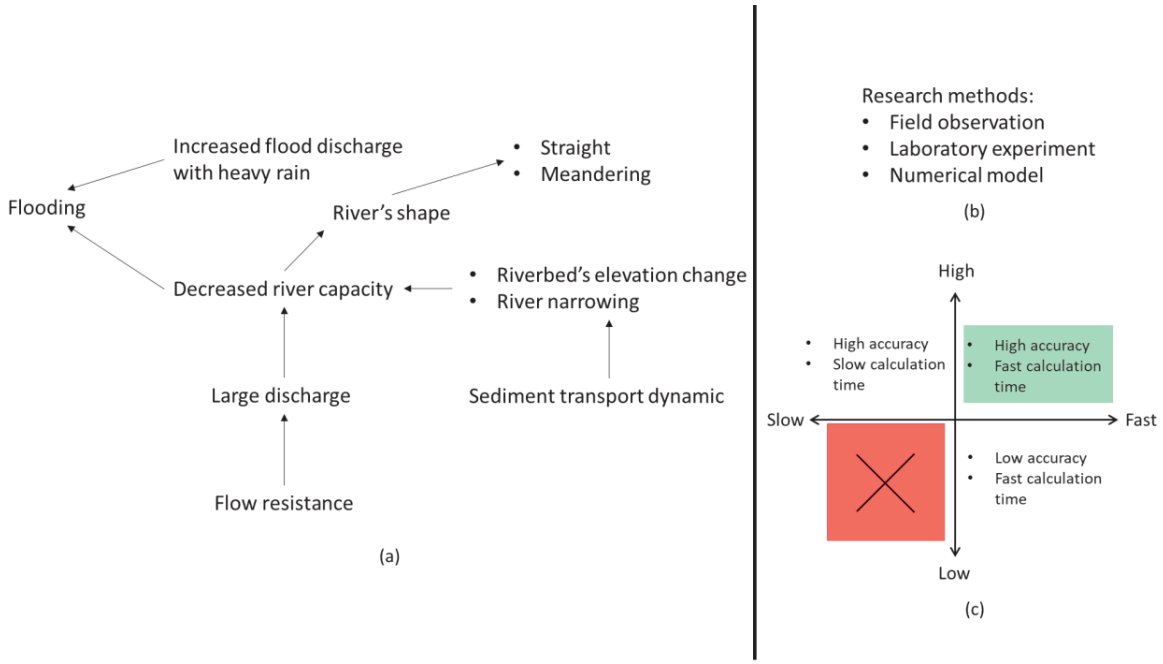

Figure 1.3 Conceptual model of this study: (a) the interplay among variables, (b) various research method approaches, (c) recent numerical model development.

the first research question arising from these considerations is: What is the influence of flow resistance and sediment transport dynamics on river capacity?

In nature, most of rivers are meander with complex flow structures compared to straight one. There are three approaches to study a phenomenon in rivers: field observation, laboratory experiment, and numerical model (Figure 1.3(b)). Numerical models, validated through experiments or observational datasets, prove to be cost-effective tools. While a 3D numerical model is preferable for capturing complex flow patterns in meandering rivers, many such models are susceptible to numerical instability and demand substantial computational resources. Consequently, hydraulic engineers often favor simpler two-dimensional (2D) depth-averaged or one-dimensional (1D) cross-section-averaged models for practical applications. However, these models lack the capability to depict the vertical flow distribution of streamwise and transverse velocity characteristic of meandering river flows. Thus, the second research question arising from these considerations is: Which numerical model is well-suited for accurately simulating complex flow structures while maintaining efficiency in cost? (Figure 1.3(c))

As a result of considering these research questions, the objectives of this study are:

- Investigating flow resistance and sediment transport dynamics in meandering rivers to get a comprehensive understanding of decreased river capacity mechanisms.
- Developing a numerical model with both efficient calculation time and high accuracy.

1.3 Research Outline

Chapter 1 presents the general introduction including literature review, research objectives, and research outline.

Chapter 2 describes the numerical models that are employed in this study.

Chapter 3 investigates flow dynamics in curved open channels and develops a numerical discretization method to overcome unphysical phenomena resulted from shallow water assumption.

Chapter 4 studies the effect of channel shape, bed characteristic, aspect ratio, and sinuosity on flow resistance.

Chapter 5 discusses sediment transport dynamics in curved and meandering channels and develops numerical model to consider sediment transport with supplied sediment condition.

Chapter 6 delivers the conclusion and future research.

Chapter 2 Numerical simulation methods

2.1 Advanced depth-integrated method

As computer hardware and software continue to rapidly evolve, numerical models have become increasingly popular for flow and sediment dynamics in rivers. Three-dimensional calculation (3DC) models are desirable to capture complicated flow structures with satisfactory accuracy (Van Balen et al., 2009, 2010; S. S. Y. Wang et al., 2009; Yan et al., 2020; Ye & McCorquodale, 1998). However, they take a great deal of computation time to be applied to practical engineering problems because of computational costs for preparing calculation grids in a vertical direction and the iterative calculation to the pressure equation as opposed to two-dimensional calculation (2DC) models (Lane, 1998; Qin et al., 2018). It is important to note that for the majority of geophysical open channel flows, where water depths are generally shallower than horizontal scales, three-dimensional analysis is often unnecessary. In fact, hydraulic engineers have used 2DC models frequently due to their simplicity in an application (Shaheed et al., 2021; Uchida et al., 2014; Uijttewaal, 2014), making them a suitable option. However, they are incapable of describing the vertical flow distribution of streamwise and transverse velocity that characterize the flow in curved and meandering rivers (Blanckaert & Graf, 2004).

In order to address the issue of long computation times with 3DC models and a lack of determining vertical flow structures with 2DC models, advanced depth-integrated models have been developed for practical problems. In this study, an advanced depth-integrated method so-called bottom velocity calculation (BVC) method was developed to study flow and sediment dynamics (Uchida et al., 2016; Uchida & Fukuoka, 2014).

2.1.1 Flow dynamics

Figure 2.1 presents the framework of the BVC method. The bottom-level z_b is defined over the thin vortex layer δz_b, and the flows between the bottom and the surface are calculated. The vertical distributions of the horizontal velocities are expressed by linear (Equation 2.1), quadratic (Equation 2.2), and cubic functions (Equation 2.3) based on the depth-averaged velocity U_i, velocity differences $\delta u_i \left(\delta u_i = u_{si} - u_{bi}\right)$, $\Delta u_i \left(\Delta u_i = U_{si} - U_i\right)$, and dimensionless depth η ($\eta = 0$ at the water surface to $\eta = 1$ at z_b).

$$u_i = \frac{\delta u_i}{2}\left(1 - 2\eta\right) + U_i \tag{2.1}$$

$$u_i = \frac{\delta u_i}{3}\left(1 - 3\eta^2\right) + U_i \tag{2.2}$$

$$u_i = \Delta u_i \left(12\eta^3 - 12\eta^2 + 1\right) + \delta u_i \left(-4\eta^3 + 3\eta^2\right) + U_i \tag{2.3}$$

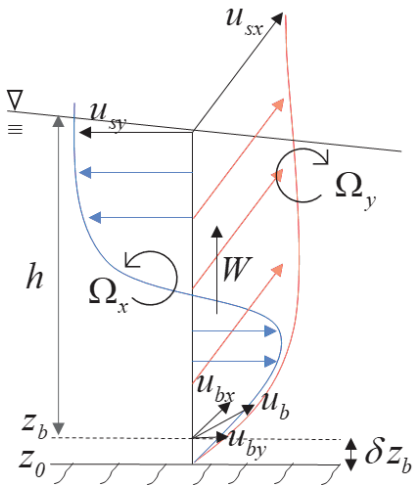

Figure 2.1 Variables of BVC in the Cartesian coordinate system

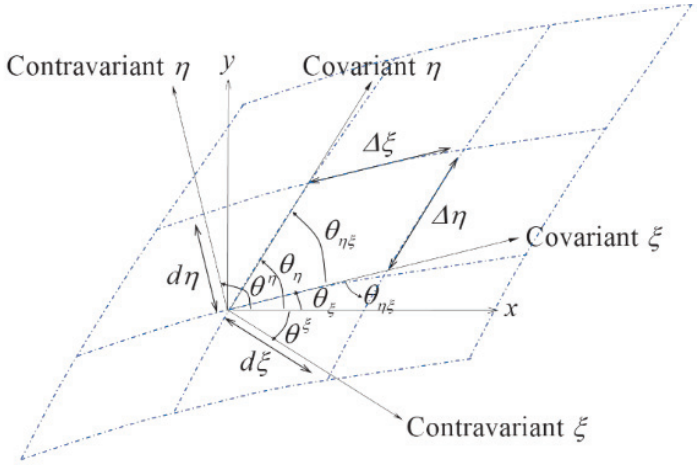

Figure 2.2 Geometry of the general coordinate system.

A general curvilinear coordinate system is effective for river flow simulations, considering the channel plan shape and conditions (Uchida et al., 2014). This study employs a general curvilinear coordinate system with physical components (Watanabe et al., 2002). Figure 2.2 illustrates the geometry.

The governing equations of the BVC method are based on the depth-integrated continuity equation (Equation 2.4) and depth-integrated horizontal momentum equations (Equation 2.5):

$$J\frac{\partial h}{\partial t}+\frac{\partial}{\partial \xi}\left(\Delta\eta\cdot Uh\right)+\frac{\partial}{\partial \eta}\left(\Delta\xi\cdot Vh\right)=0 \tag{2.4}$$

$$
\begin{aligned}
&h\frac{\partial U_\xi}{\partial t}+U_\xi h\frac{\partial U_\xi}{\partial \tilde{\xi}}+U_\eta h\frac{\partial U_\xi}{\partial \tilde{\eta}}-\tilde{J}\left(U_\eta-U_\xi\cos\theta^{\eta\xi}\right)\left(U_\xi h\frac{\partial \theta^\xi}{\partial \tilde{\xi}}+U_\eta h\frac{\partial \theta^\xi}{\partial \tilde{\eta}}\right)\\
&=-\frac{\tau_{b\xi}}{\rho}-\tau_{K\xi}-gh\left(\frac{\partial z_s}{\partial \tilde{\xi}}+\cos\theta^{\eta\xi}\frac{\partial z_s}{\partial \tilde{\eta}}\right)-\frac{1}{\rho}\left(\frac{\partial hdp_0}{\partial \tilde{\xi}}+\cos\theta^{\eta\xi}\frac{\partial hdp_0}{\partial \tilde{\eta}}\right)\\
&-\frac{dp_b}{\rho}\left(\frac{\partial z_b}{\partial \tilde{\xi}}+\cos\theta^{\eta\xi}\frac{\partial z_b}{\partial \tilde{\eta}}\right)+\frac{1}{J}\left\{\frac{\partial}{\partial \xi}\left(\Delta\eta\cdot hT_{\xi\xi}\right)+\frac{\partial}{\partial \eta}\left(\Delta\xi\cdot hT_{\xi\eta}\right)\right\}\\
&-\tilde{J}h\left\{\left(-T_{\xi\xi}\cos\theta^{\eta\xi}+T_{\xi\eta}\right)\frac{\partial \theta^\xi}{\partial \tilde{\xi}}+\left(-T_{\xi\eta}\cos\theta^{\eta\xi}+T_{\eta\eta}\right)\frac{\partial \theta^\xi}{\partial \tilde{\eta}}\right\}\\
&h\frac{\partial U_\eta}{\partial t}+U_\xi h\frac{\partial U_\eta}{\partial \tilde{\xi}}+U_\eta h\frac{\partial U_\eta}{\partial \tilde{\eta}}+\tilde{J}\left(U_\xi-U_\eta\cos\theta^{\eta\xi}\right)\left(U_\xi h\frac{\partial \theta^\eta}{\partial \tilde{\xi}}+U_\eta h\frac{\partial \theta^\eta}{\partial \tilde{\eta}}\right)\\
&=-\frac{\tau_{b\eta}}{\rho}-\tau_{K\eta}-gh\left(\frac{\partial z_s}{\partial \tilde{\eta}}+\cos\theta^{\eta\xi}\frac{\partial z_s}{\partial \tilde{\xi}}\right)-\frac{1}{\rho}\left(\frac{\partial hdp_0}{\partial \tilde{\eta}}+\cos\theta^{\eta\xi}\frac{\partial hdp_0}{\partial \tilde{\xi}}\right)\\
&-\frac{dp_b}{\rho}\left(\frac{\partial z_b}{\partial \tilde{\eta}}+\cos\theta^{\eta\xi}\frac{\partial z_b}{\partial \tilde{\xi}}\right)+\frac{1}{J}\left\{\frac{\partial}{\partial \xi}\left(\Delta\eta\cdot hT_{\xi\xi}\right)+\frac{\partial}{\partial \eta}\left(\Delta\xi\cdot hT_{\xi\eta}\right)\right\}\\
&-\tilde{J}h\left\{\left(T_{\xi\eta}\cos\theta^{\eta\xi}+T_{\xi\xi}\right)\frac{\partial \theta^\eta}{\partial \tilde{\xi}}+\left(T_{\eta\eta}\cos\theta^{\eta\xi}+T_{\xi\eta}\right)\frac{\partial \theta^\xi}{\partial \tilde{\eta}}\right\}
\end{aligned}
\tag{2.5}
$$

where ξ, η are the general curvilinear coordinates, J is the Jacobian (area of the computational grid, $J=x_\xi y_\eta-x_n y_\xi$), and $\Delta\xi$ and $\Delta\eta$ are the calculation grid spacings of the covariant in ξ and η directions, respectively; $\tilde{J}=J/d\xi d\eta$; $\theta^\xi=\theta_\eta-\pi/2$, $\theta^\eta=\theta_\xi+\pi/2$; $\partial/\partial\tilde{\xi}=\partial/d\xi\cdot\partial\xi$, $\partial/\partial\tilde{\eta}=\partial/d\eta\cdot\partial\eta$; g is the acceleration due to gravity; h is the water depth; U_ξ and U_η are the depth-averaged horizontal velocities in the ξ and η directions, respectively; $\tau_{b\xi}$ and $\tau_{b\eta}$ are the bed shear stresses in the ξ and η directions, respectively; τ_K is the vegetation resistance term; $T_{\xi\xi}$, $T_{\eta\eta}$, $T_{\xi\eta}$ is the horizontal momentum transfer comprising the shear stress terms of the turbulent motions and a dispersion term resulting from the vertical velocity distribution. Pressure p is expressed using the pressure deviation from the hydrostatic pressure distribution as

$p=\rho g\left(z_s-z\right)+dp$, $dp_0=dp_b/2$, dp_b is the bottom pressure deviation, and dp_0 is the depth-averaged pressure deviation.

$$
\begin{aligned}
T_{\xi\xi} &= -2\nu_t\left\{\left(\frac{\partial U_\xi}{\partial\tilde{\xi}}+\cos\theta^{\eta\xi}\frac{\partial U_\xi}{\partial\tilde{\eta}}\right)-\tilde{J}\left(U_\eta-U_\xi\cos\theta^{\eta\xi}\right)\left(\frac{\partial\theta^\xi}{\partial\tilde{\xi}}+\cos\theta^{\eta\xi}\frac{\partial\theta^\xi}{\partial\tilde{\eta}}\right)\right\}+\overline{u_\xi' u_\xi'} \\
T_{\eta\eta} &= -2\nu_t\left\{\left(\frac{\partial U_\eta}{\partial\tilde{\eta}}+\cos\theta^{\eta\xi}\frac{\partial U_\eta}{\partial\tilde{\xi}}\right)+\tilde{J}\left(U_\xi-U_\eta\cos\theta^{\eta\xi}\right)\left(\frac{\partial\theta^\eta}{\partial\tilde{\eta}}+\cos\theta^{\eta\xi}\frac{\partial\theta^\eta}{\partial\tilde{\xi}}\right)\right\}+\overline{u_\eta' u_\eta'} \\
T_{\xi\eta} &= -\nu_t\left\{\left(\frac{\partial U_\xi}{\partial\tilde{\eta}}+\cos\theta^{\eta\xi}\frac{\partial U_\xi}{\partial\tilde{\xi}}\right)-\tilde{J}\left(U_\eta-U_\xi\cos\theta^{\eta\xi}\right)\left(\frac{\partial\theta^\xi}{\partial\tilde{\eta}}+\cos\theta^{\eta\xi}\frac{\partial\theta^\xi}{\partial\tilde{\xi}}\right)\right\} \\
&\quad+\left\{\left(\frac{\partial U_\eta}{\partial\tilde{\xi}}+\cos\theta^{\eta\xi}\frac{\partial U_\eta}{\partial\tilde{\eta}}\right)+\tilde{J}\left(U_\xi-U_\eta\cos\theta^{\eta\xi}\right)\left(\frac{\partial\theta^\eta}{\partial\tilde{\xi}}+\cos\theta^{\eta\xi}\frac{\partial\theta^\eta}{\partial\tilde{\eta}}\right)\right\}+\overline{u_\xi' u_\eta'}
\end{aligned}
\tag{2.6}
$$

$$
\overline{u_i' u_j'}=\frac{13}{35}\Delta u_i\Delta u_j-\frac{2}{35}\left(\Delta u_i\delta u_j+\Delta u_j\delta u_i\right)+\frac{3}{35}\delta u_i\delta u_j \tag{2.7}
$$

where ν_t denotes the kinematic eddy viscosity. Instead of solving the transport equation of kinetic energy (Uchida et al., 2016; Uchida & Fukuoka, 2014), the present model employs the zero-equation model in which the production and dispersion terms are balanced as

$$
P_k=\varepsilon \tag{2.8}
$$

$$
\frac{P_k}{\nu_t}=2\left(S_{ij}^2+\overline{s_{ij}'^2}\right)+\overline{\left(\frac{\partial u_i}{\partial z}\right)^2} \tag{2.9}
$$

where k is the depth-averaged turbulent kinetic energy; $\nu_t=C_\mu k^2/\varepsilon$; $C_\mu=0.09$; $\varepsilon=C_\varepsilon k^{3/2}/\Delta=C_\varepsilon' k^{3/2}/h$; $C_\varepsilon'=1.7$ (Δ is the turbulence scale); $C_h=9\left(\alpha C_\varepsilon'\right)^4/C_\mu^3$; S_{ij} is the depth-averaged rate of the strain tensor; s_{ij}' is the strain velocity of the deviation velocity u_i'.

The SBVC3 and GBVC3 models employ the cubic velocity distribution as the vertical distribution of the horizontal velocity, while the SBVC2 model assumes a quadratic velocity distribution. The velocity difference between the water surface and the bottom is given by depth-integrated horizontal vorticity as

$$\delta u_i = u_{si} - u_{bi} = \varepsilon_{ij}\Omega_j h + \left(\frac{\partial Wh}{\partial x_i} - w_s \frac{\partial z_s}{\partial x_i} + w_b \frac{\partial z_b}{\partial x_i} \right) \tag{2.10}$$

where *i, j* is 1(x), 2(y), $x_3 = z$ is the vertical axis, ε_{ij} is the Levi-Civita symbol, u_{bi} is the bottom velocity, u_{si} is the water surface velocity, Ω_j is the depth-averaged vorticity in the *j* direction, *h* is the water depth, *W* is the depth-averaged vertical velocity w, and w_s and w_b are the vertical velocities at the water surface and bottom, respectively.

Bottom velocity in Equation 2.10 was evaluated using the water surface velocity and depth-integrated horizontal vorticity equations (Equation 2.11):

$$\frac{J\partial\Omega_i h}{\partial t} = J\left(ER_{\sigma i} + P_{\omega i}\right) + \frac{\partial h\Delta\eta D_{\omega i\xi}}{\partial\xi} + \frac{\partial h\Delta\xi D_{\omega i\eta}}{\partial\eta} \tag{2.11}$$

where $ER_{\sigma i}$ is the rotation term of the vertical vorticity $\left(ER_{\sigma i} = u_{si}\omega_{\sigma s} - u_{bi}\omega_{\sigma b}\right)$; $\omega_{\sigma s}$ and $\omega_{\sigma b}$ indicate the rotation of u_{si} and u_{bi}, respectively; $P_{\omega i}$ is the vorticity production term corresponding to the bottom vortex layer; $D_{\omega i\xi}$ and $D_{\omega i\eta}$ are the horizontal vorticity fluxes due to advection, rotation, dispersion, and turbulence diffusion expressed by

$$D_{\omega i\xi} = -U_\xi \Omega_i + U_i \Omega_\xi + \overline{\omega_\xi' u_i'} - \overline{\omega_i' u_\xi'} + \frac{\nu_t}{\sigma_\omega}\left(\frac{\partial \Omega_i}{\partial \tilde{\xi}} + \cos\theta^{\eta\xi}\frac{\partial \Omega_i}{\partial \tilde{\eta}}\right)$$
$$D_{\omega i\eta} = -U_\eta \Omega_i + U_i \Omega_\eta + \overline{\omega_\eta' u_i'} - \overline{\omega_i' u_\eta'} + \frac{\nu_t}{\sigma_\omega}\left(\frac{\partial \Omega_i}{\partial \tilde{\eta}} + \cos\theta^{\eta\xi}\frac{\partial \Omega_i}{\partial \tilde{\xi}}\right) \quad (2.12)$$

where $\omega_i' = \omega_i - \Omega_j$ and $\sigma_\omega = 1$. The production terms $P_{\omega i}$ are given by Equation 2.13.

$$P_{\omega i} = C_{p\omega} \nu_{tb} (\omega_{bei} - \omega_{bi}) / h \quad (2.13)$$

where $C_{p\omega} = \kappa / \alpha$, $\alpha = \kappa / 6$, $\kappa = 0.41$, $\nu_{tb} : \nu_t$ at the bottom transformed to a depth-averaged scale assuming $\nu_{tb} = \max\left(\alpha^2 h^2 \omega_b,\ \alpha^2 h^2 \omega_{be}\left(=\alpha c_b u_b h\right),\ \nu_t\right)$; ω_{bi} is the horizontal vorticity at the bottom, ω_{bei} is the equilibrium ω_{bi} for u_b, given by Equation 2.14.

$$\omega_{bej} = 2\frac{\varepsilon_{ij3} c_b u_{bi}}{\kappa h} \ln(1 + h / \delta z_b) \quad (2.14)$$

where $\frac{1}{c_b} = \frac{1}{\kappa} \ln \frac{z_b}{k_s} + 8.5$; κ is the von Karman constant; k_s is the equivalent sand grain roughness.

The water surface velocity u_s that is necessary to solve the bottom velocity with Equation 2.10 can be solved using Equation 2.15.

$$
\begin{aligned}
&\frac{\partial u_{s\xi}}{\partial t}+u_{s\xi}\frac{\partial u_{s\xi}}{\partial \tilde{\xi}}+u_{s\eta}\frac{\partial u_{s\xi}}{\partial \tilde{\eta}}-\tilde{J}\left(u_{s\eta}-u_{s\xi}\cos\theta^{\eta\xi}\right)\left(u_{s\xi}\frac{\partial \theta^{\xi}}{\partial \tilde{\xi}}+u_{s\eta}\frac{\partial \theta^{\xi}}{\partial \tilde{\eta}}\right)\\
&=-g\left(\frac{\partial z_s}{\partial \tilde{\xi}}+\cos\theta^{\eta\xi}\frac{\partial z_s}{\partial \tilde{\eta}}\right)-\left(\frac{\partial z_s}{\partial \tilde{\xi}}+\cos\theta^{\eta\xi}\frac{\partial z_s}{\partial \tilde{\eta}}\right)\left(\frac{\partial dp}{\partial z}\right)_{z=z_s}+P_{s\xi}\\
&\frac{\partial u_{s\eta}}{\partial t}+u_{s\xi}\frac{\partial u_{s\eta}}{\partial \tilde{\xi}}+u_{s\eta}\frac{\partial u_{s\eta}}{\partial \tilde{\eta}}+\tilde{J}\left(u_{s\zeta}-u_{s\eta}\cos\theta^{\eta\xi}\right)\left(u_{s\xi}\frac{\partial \theta^{\eta}}{\partial \tilde{\xi}}+u_{s\eta}\frac{\partial \theta^{\eta}}{\partial \tilde{\eta}}\right)\\
&=-g\left(\frac{\partial z_s}{\partial \tilde{\xi}}+\cos\theta^{\eta\xi}\frac{\partial z_s}{\partial \tilde{\eta}}\right)-\left(\frac{\partial z_s}{\partial \tilde{\xi}}+\cos\theta^{\eta\xi}\frac{\partial z_s}{\partial \tilde{\eta}}\right)\left(\frac{\partial dp}{\partial z}\right)_{z=z_s}+P_{s\eta}
\end{aligned}
\tag{2.15}
$$

where $u_{s\xi}$ and $u_{s\eta}$ are the water surface velocities in the streamwise and lateral axes, respectively; P_{si} is the production term due to the shear stress acting on the thin water surface layer δz_s represented by Equation 2.16.

$$
P_{si}=\frac{2\nu_t}{h^2}\left\{36\left(u_{sei}-u_{si}\right)-\left(3\delta u_i-6\Delta u_i\right)\right\} \tag{2.16}
$$

The GBVC3 model was expanded for application to more general cases without the shallow water assumption for the 2DC and SBVC models. The bottom pressure deviation from the hydrostatic pressure distribution was obtained by depth-integrating the vertical momentum equation:

$$
\frac{dp_b}{\rho}=U_{\xi}h\frac{\partial W}{\partial \tilde{\xi}}+U_{\eta}h\frac{\partial W}{\partial \tilde{\eta}}+\frac{\tau_{b\xi}}{\rho}\frac{\partial z_b}{\partial \tilde{\xi}}+\frac{\tau_{b\eta}}{\rho}\frac{\partial z_b}{\partial \tilde{\eta}} \tag{2.17}
$$

To evaluate Equation 2.17 and the third term on the right side of Equation 2.10, the vertical velocity equation double-integrated with the continuity equation over water depth is given by Equation 2.18:

$$Wh = h\left(\frac{\partial z_m}{\partial t} + U_\xi \frac{\partial z_m}{\partial \tilde{\xi}} + U_\eta \frac{\partial z_m}{\partial \tilde{\eta}} \right) + \frac{\partial}{J\partial \xi}\left(\Delta\eta \cdot h^2 \left(k_2 \Delta u_\xi + k_1 \delta u_\xi \right) \right) + \frac{\partial}{J\partial \eta}\left(\Delta\xi \cdot h^2 \left(k_2 \Delta u_\eta + k_1 \delta u_\eta \right) \right) \tag{2.18}$$

where $z_m = \left(z_s + z_b\right)/2,\ k_1 = 1/10,\ k_2 = 1/20$. k_1 and k_2 depend on the velocity distribution function that is derived by considering the double integral of the continuity equation along the vertical direction (Uchida et al., 2016; Uchida & Fukuoka, 2014).

2.1.2 Sediment transport

The variation in bed level over time is determined by applying Exner's 2D continuity equation for sediment transport (Equation 2.19), with the exclusion of temporal changes in bedload sediment.

$$\left(1 - \lambda_B\right)\frac{\partial z_b}{\partial t} + \frac{\partial q_{Bi}}{\partial x_i} = 0 \tag{2.19}$$

where λ_B : sediment porosity (λ_B = 0.4) and q_{Bi} : bedload sediment transport rate. The sediment transport rate is assumed in the equilibrium condition. The equilibrium bedload is given by Ashida and Michiue (1972) with a modification of the coefficient (Equation 2.20).

$$q_{Be*} = C_{qB}\tau_*^{3/2}\left(1 - \tau_{*c}/\tau_*\right)\left(1 - \sqrt{\tau_{*c}/\tau_*}\right) \tag{2.20}$$

where τ_* and τ_{*c} are non-dimensional bed tractive and critical bed tractive forces, respectively. C_{qB} is a constant to reproduce the experimental sediment discharge. The bed tractive and critical bed tractive forces are calculated by Equations 2.21 and 2.22 with the gravitational effect on the bed slope.

$$\tau_*^2 = \tau_{*i}\tau_{*i}, \quad \tau_{*i} = \frac{\tau_{bsi}}{sgd} - \frac{\tau_{*c}}{\mu_s}\frac{\partial z_b}{\partial x_i} \tag{2.21}$$

$$\tau_{*c} = \tau_{*c0}\cos\theta, \quad 1\Big/\cos^2\theta = 1 + \frac{\partial z_b}{\partial x_i}\frac{\partial z_b}{\partial x_i} \tag{2.22}$$

where τ_{bsi}, i: direction component of τ_{bs}; μ_s: static friction coefficient; τ_{*c0}: non-dimensional critical shear stress on a horizontal bed (τ_{*c0} = 0.034 for d = 0.8 mm of the experiment); and θ: maximum bed gradient. Where the bed slope exceeds the angle of repose φ (tan φ = 0.6), the instantaneous sand slide in the maximum grade direction can be found in the calculation.

2.2 Types of BVC models

There are several types of BVC models employed in this study: (1) The SBVC (simplified bottom velocity calculation) method with shallow water assumption that employs hydrostatic pressure distribution and neglects the variation in vertical velocity. The SBVC2 model assumes the equilibrium condition of water surface flow, while SBVC3 calculates the momentum equations for water surface flows. (2) The GBVC3 (general bottom velocity calculation) model is not restricted to the shallow water assumption and calculates the non-hydrostatic pressure distribution and variation in vertical velocity (Uchida et al., 2016; Uchida & Fukuoka, 2014). Table 2.1 shows an unknown variables and equations for BVC models and a conventional 2D model.

Table 2.1 Unknown variables and equations for calculation method.

BVC models				Unknown variable	Governing equation	Equation number
GBVC3	SBVC3	SBVC2	2D			
○	○	○	○	h	Depth-integrated continuity equation	(2.4)
○	○	○	○	U_i	Depth-integrated horizontal momentum equations	(2.5)
○	○	○		u_{bi}	Depth-integrated equation of horizontal vorticity	(2.10)
○	○	○		Ω_i	Depth-integrated vorticity equations	(2.11)
○	○			u_{si}	Horizontal momentum equation for water surface	(2.15)
○				dp_b	Depth-integrated vertical momentum equation	(2.17)
○				W	Double integrated continuity equations	(2.18)

2.3 Three-dimensional calculation method

In this study, a three-dimensional computation served as a reference for evaluating the depth-integrated method. The NaysCUBE model was chosen which is based on the RANS equation (Kimura et al., 2009). The governing equations encompass the continuity equation (Equation 2.23), the momentum equation (Equation 2.24), the k-equation (Equation 2.25), and the ε-equation (Equation 2.26). These governing equations undergo a transformation via a generalized curvilinear

coordinate formulation, enabling the conversion of any given domain into a computational cube for solution (Kimura, 2020; Nelson et al., 2016).

$$\frac{\partial U_i}{\partial x_i} = 0 \tag{2.23}$$

$$\frac{\partial U_i}{\partial x_i} + \frac{\partial U_i U_j}{\partial x_j} = G_i - \frac{1}{\rho}\frac{\partial p}{\partial x_i} + \frac{\partial\left(\overline{-u_i u_j}\right)}{\partial x_j} + \nu\frac{\partial^2 U_i}{\partial x_i \partial x_j} \tag{2.24}$$

$$\frac{\partial k}{\partial t} + \frac{\partial k U_j}{\partial x_j} = \overline{-u_i u_j}\frac{\partial U_i}{\partial x_j} - \varepsilon + \frac{\partial}{\partial x_j}\left\{\left(\frac{\nu_t}{\sigma_k} + \nu\right)\frac{\partial k}{\partial x_j}\right\} \tag{2.25}$$

$$\frac{\partial \varepsilon}{\partial t} + \frac{\partial \varepsilon U_j}{\partial x_j} = -C_{\varepsilon 1}\frac{\varepsilon}{k}\overline{u_i u_j}\frac{\partial U_i}{\partial x_j} - C_{\varepsilon 2}\frac{\varepsilon^2}{k} + \frac{\partial}{\partial x_j}\left\{\left(\frac{\nu_t}{\sigma_\varepsilon} + \nu\right)\frac{\partial \varepsilon}{\partial x_j}\right\} \tag{2.26}$$

where x_i : spatial coordinates; t : time; U_i : flow velocity; p : pressure; u_i : turbulent velocity; ν : kinematic viscosity coefficient; ρ : fluid density; k : turbulent kinetic energy; ε : dissipation rate of turbulent kinetic energy; ν_t : turbulent kinetic viscosity coefficient; G_i : gravity acceleration; $\overline{u_i u_j}$: Reynolds stress tensor.

2.4 Evaluation of dispersion term in momentum equations for advanced depth-integrated models

The accuracy of the advection term is generally important in flow analysis (Wu, 2008). However, within channel bends, the evaluation of the dispersion term becomes increasingly crucial for calculating momentum transfer attributed to the vertical velocity distribution, surpassing the importance of the advection term. In simpler terms, an incorrect discretization of the dispersion

term can lead to unphysical solutions similar to those arising from the advection term, considering that the dispersion term originates from the advection term. The vertical velocity distribution is frequently disregarded by 2DC models, leading to inaccuracies in the main velocity distribution. Consequently, when applied to channel bends, several 2DC models that neglect dispersion terms have exhibited unsatisfactory performance (Jia & Wang, 1999; Ye & McCorquodale, 1997).

Figure 2.3 illustrates the momentum transfer in a channel bend with the distribution of the transverse and vertical velocities in the cross-sectional vertical view. The vertical velocity profile is expressed as a linear velocity distribution to simplify the mathematical derivation of the dispersion term. In the middle of the channel, the surface velocity moves outward and the bottom velocity moves inward with the streamwise vorticity of the secondary flow. The shallow water assumption for Equation (2.10), in which the second term for the distribution in vertical velocity in the right side of the equation is neglected, provides a high momentum transfer near the wall, as indicated by the red dashed-line velocity profile.

This paper develops a numerical discretization scheme for the dispersion terms in the momentum equation for depth-averaged horizontal velocity distribution in the Cartesian coordinate

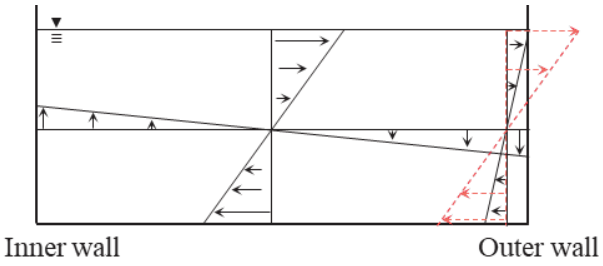

Figure 2.3 Illustration of momentum transfer in a channel bend. Red dash line shows the unphysical property of velocity distribution resulted by shallow water assumption.

system (Equation (2.27), the equation for the general curvilinear coordinate system can be found in Chapter 2.1.1).

$$\frac{\partial U_i h}{\partial t}+\frac{\partial U_i U_j h}{\partial x_j}=-gh\frac{\partial z_s}{\partial x_i}-\frac{\tau_{bi}}{\rho}+\frac{\partial hT_{ij}}{\rho\partial x_j}-\left(\frac{\partial hdp_0}{\rho\partial x_i}+\frac{dp_b}{\rho}\frac{\partial z_b}{\partial x_i}\right) \tag{2.27}$$

$$T_{ij}=\left(\nu+\overline{\nu_t}\right)\left(\frac{\partial U_i}{\partial x_j}+\frac{\partial U_j}{\partial x_i}\right)-\overline{u_i^{'}u_j^{'}} \tag{2.28}$$

where, i, j=1, 2; x_3 is vertical direction; $h=z_s-z_b$; h: water depth; z_s: water surface; z_b: bottom; U_i: depth-averaged horizontal velocity u_i; τ_{bi}: bottom shear stress. The pressure p is expressed using the pressure deviation from the hydrostatic pressure distribution as $p=g\left(z_s-z\right)+dp$; $dp_0=dp_b/2$. The horizontal shear stresses T_{ij} consist of shear stresses due to molecular and turbulent motions (the first term on the right-hand side of Equation (2.28)) and dispersion term due to vertical velocity distribution (the second term on the right-hand side of Equation (2.28)), which is included in the third term in the right-hand side of Equation (2.27). The bar in the dispersion term $\overline{u_i^{'}u_j^{'}}$ represents the integrated value over water depth and $u_i^{'}$ is deviation from the depth-averaged velocity defined as $u_i^{'}=u_i-U_i$.

Since the central differential scheme in the discretization for the advection terms often causes numerical oscillations, several schemes have been developed, such as upwind scheme (Wu, 2008). It is crucial to calculate the momentum transfer due to the dispersion term in a channel bend because the momentum transfer due to the secondary flow in the transverse direction is more dominant than the convection terms. However, to the best of our knowledge, an appropriate discretization scheme for the dispersion term has not been discussed enough for advanced depth-

integrated models. Especially in the case of shallow-water assumption, the abrupt changes in horizontal momentum transport due to secondary flow, such as the flow near side walls as indicated in Figure 2.3, cannot be handled appropriately. An appropriate discretization method is considered necessary as stabilization schemes for the advection term is particularly important in the explicit scheme. While the central differential scheme has been applied in previous studies without the shallow water assumption (Uchida et al., 2016; Uchida & Fukuoka, 2014), this study develop a first-order upwind scheme for the dispersion term for the general use in the advanced depth integrated model.

The dispersion and advection terms in the depth-integrated momentum equations [Equation (2.27)] were derived using the depth integration procedure from the advection term in the Reynolds-averaged Navier–Stokes equation. The depth-integrated momentum transfer is defined by Equation (2.29).

$$\int_h \left(u_i u_j\right)_J dz = h\left(U_i U_j\right)_J + \int_h \left(u'_i u'_j\right)_J dz \tag{2.29}$$

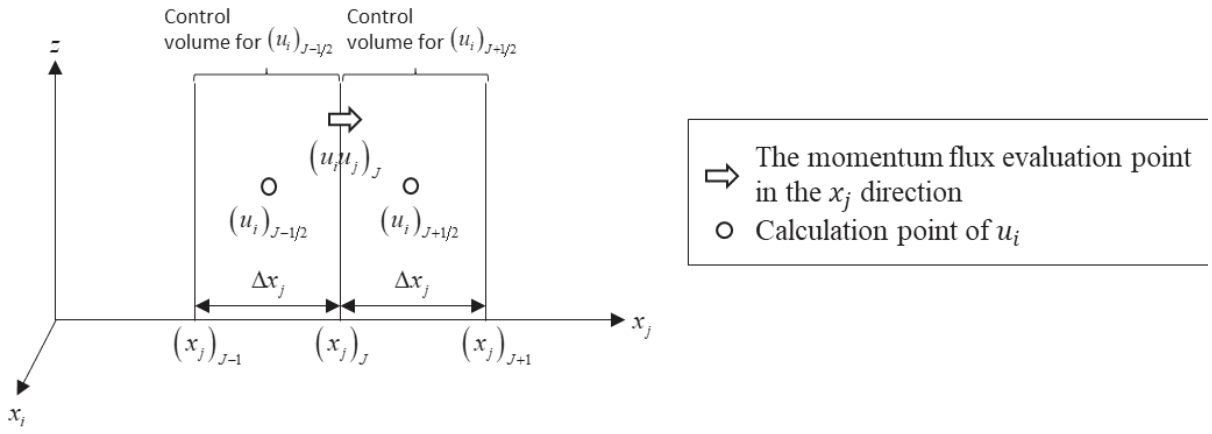

Figure 2.4 Evaluated variable in the numerical discretization method.

where, J is the evaluation point for x_j direction, as shown in Figure 2.4. The first and second terms in Equation (2.29) were evaluated using advection and dispersion terms that can be found in the second term on the left-hand side of Equation (2.27) and the second term on the right-hand side of Equation (2.28), respectively. Let us consider the *i*-direction momentum flux in the *j*-direction (*j*-direction advection term in the *i*-direction momentum equation) at $J\left(x_j=\left(x_j\right)_J\right)$, as shown in Figure 2.4 for a 3DC grid system. The variable u_i, of which a temporal variation is calculated with the momentum equation, is evaluated at the half grid upstream or downstream from *J*.

The first-order upwind scheme for the momentum flux of u_i by u_j is introduced by combining the centered scheme and its diffusion as

$$(u_i'u_j')_J \approx \left(u_i'\right)_J\left(u_j'\right)_J - d_{ij} \quad , \quad d_{ij}=\left|\left(u_j\right)_J\right|\left\{\left(u_i\right)_{J+1/2}-\left(u_i\right)_{J-1/2}\right\} \tag{2.30}$$

To integrate the numerical diffusion term d_{ij} over water depth for the upwind dispersion terms, a linear vertical velocity distribution [Equation (2.31)] is assumed for simplicity.

$$u_i=\frac{\delta u_i}{2}(1-2\eta)+U_i \tag{2.31}$$

where $\delta u_i\left(\delta u_i=u_{si}-u_{bi}\right)$ is velocity differences and η is dimensionless depth ($\eta=$ 0 at the water surface to $\eta=1$ at z_b). By substituting Equation (2.31) into Equation (2.30), and assuming $U_j=0$ for the dispersion term, d_{ij} is obtained as

$$d_{ij} = \left|\frac{1-2\eta}{2}\delta u_j\right| \cdot \left\{(U_i)_{J+1/2} - (U_i)_{J-1/2} + \frac{1-2\eta}{2}\left((\delta u_i)_{J+1/2} - (\delta u_i)_{J-1/2}\right)\right\} \tag{2.32}$$

The depth-averaged diffusion flux D_{ij} for the depth integrated momentum equation is derived as

$$D_{ij} = \int_0^1 d_{ij} d\eta = \frac{|\delta u_j|}{8} \cdot \Delta x_j \cdot \frac{(U_i)_{J+1/2} - (U_i)_{J-1/2}}{\Delta x_j} = \varepsilon_j \frac{\partial U_i}{\partial x_j} \tag{2.33}$$

Notably, Equation (2.33) in this study does not follow the Einstein summation. As indicated above, Equation (2.33) is derived for the condition $U_j = 0$, assuming no advection term due to the depth-averaged velocity. When the velocity sign u_j does not change over the water depth, the upwind effect is considered in the advection term, and no numerical diffusion term is required for the dispersion term. Considering the linear velocity distribution of u_j, the diffusion term [Equation (2.33)] is expanded for flows with depth-averaged velocity U_j, as follows:

$$\varepsilon_j = \begin{cases} \dfrac{|\delta u_j| - 2|U_j|}{8} \cdot \Delta x_j & (|\delta u_j| > 2|U_j|) \\ 0 & (|\delta u_j| \le 2|U_j|) \end{cases} \tag{2.34}$$

The numerical diffusion term D_{ij} was added to the dispersion term [Equation (2.27)] for the horizontal shear stress term in the *i*-direction momentum equations.

Chapter 3 Numerical calculations for curved open channel flows with advanced depth-integrated models

3.1 Introduction

Numerical calculation models have become one of the most effective ways of studying the open channel flows coupled with field observations and laboratory experiments. Three-dimensional calculation (3DC) models are desirable to capture complicated flow structures with satisfactory accuracy (Van Balen et al., 2009, 2010; S. S. Y. Wang et al., 2009; Yan et al., 2020; Ye & McCorquodale, 1998). However, they take a great deal of computation time to be applied to practical engineering problems because of computational costs for preparing calculation grids in a vertical direction and the iterative calculation to the pressure equation as opposed to two-dimensional calculation (2DC) models (Lane, 1998; Qin et al., 2018).

It is important to note that for the majority of geophysical open channel flows, where water depths are generally shallower than horizontal scales, three-dimensional analysis is often unnecessary. In fact, hydraulic engineers have used 2DC models frequently due to their simplicity in an application (Shaheed et al., 2021; Uchida et al., 2014; Uijttewaal, 2014), making them a suitable option. However, they are incapable of describing the vertical flow distribution of streamwise and transverse velocity that characterize the flow in curved and meandering rivers (Blanckaert & Graf, 2004).

In order to address the issue of long computation times with 3DC models and a lack of determining vertical flow structures with 2DC models, advanced 2DC models have been developed for practical problems. An advanced 2DC model with the assumption of hydrostatic pressure

distribution was proposed by Jin and Steffler (1993) to simulate velocity distribution in curved open channels using a boundary-fitted coordinate system. Finnie et al. (1999) developed a secondary flow model by solving the transport equation of streamwise vorticity with an acceleration term to predict depth-averaged velocity better. The results were in good agreement with the experimental datasets compared with those of the conventional 2DC model without the dispersion term.

Uchida and Fukuoka (2014) introduced an advanced depth-integrated method, known as the Bottom Velocity Calculation (BVC) method, designed to compute sediment transport and bed topography resulting from three-dimensional flows in both simple and compound meandering channels. This method incorporates additional equations, such as depth-integrated horizontal vorticity equations, momentum equations for the water surface, double-integrated continuity equations over depth, and depth-integrated vertical momentum equations accounting for non-hydrostatic pressure distribution. These equations are coupled with depth-integrated continuity and horizontal momentum equations to calculate the bottom velocity.

Uchida et al. enhanced the method by integrating it with the dynamic wall law, employing a fourth-degree polynomial equation for the vertical distribution of velocity. This sophisticated approach demonstrated significant improvements in modeling complex flow over a rough bed with isolated submerged boulders, even in close proximity to the bed (Uchida et al., 2016) and rapid sediment transport with dam-break flows (Uchida & Fukuoka, 2019). Although the BVC method has been extensively used in complex conditions, performance of the method for simple channel bends has not been sufficiently discussed (Lugina et al., 2020, 2022).

Because 2DC models are still actively used to calculate long-term, wide-area flows, such as riverbed morphology with sediment transport (Begnudelli et al., 2010; Bora & Kalita, 2020; Shaheed et al., 2021; Shimizu et al., 2020; C. G. Song et al., 2012), it is important to clarify the accuracy and applicability range of the 2DC model and the method to enhance the 2DC models. This paper examines the effect of coupling several equations for vertical velocity and pressure profiles in a depth-integrated model to clarify the roles of three-dimensional flow structures in curved channels on reducing errors inherent in the 2DC model. For these objectives, this paper compared various models including conventional 2DC to advanced 2DCs and 3DC models, to better understand roles of the equation and terms for calculating the flow.

This study has developed a numerical technique to discretize the dispersion terms found in the depth-averaged horizontal momentum equations. The other objective is to develop an effective scheme for the horizontal momentum transfer caused by velocity profiles such as the secondary flows in channel bends (Blanckaert & Graf, 2001; Da Silva & Ebrahimi, 2017; De Vriend, 1979; Falcon, 1984; Pan et al., 2022; Rozovskii, 1957). This secondary flow induces the transverse convection of primary flow momentum from the inner bank to the outer bank, resulting in significant alterations to the velocity distribution. Numerous researchers have incorporated the dispersion term into two-dimensional depth-averaged models to capture the impact of momentum transfer associated with secondary flow structures (Begnudelli et al., 2010; Duc et al., 2004; Lazzarin & Viero, 2023; C. G. Song et al., 2012). Log-law distribution (Duan, 2004) and linear models (Ghamry & Steffler, 2005; Jin & Steffler, 1993) have been used extensively for evaluating the horizontal momentum transfer due to secondary flow. The advection term in the momentum equation has been treated by several discretization schemes (Duc et al., 2004; Lazzarin & Viero,

2023; C. G. Song et al., 2012). However, as far as our knowledge extends, there has been insufficient discussion regarding an appropriate discretization scheme for the dispersion term arising from the vertical velocity distribution in advanced depth-integrated models. Furthermore, after confirming the applicability of the proposed method, the models were then extended to be applied to the bed topographic steering case.

3.2 Methods

3.2.1 Numerical calculation models

The effectiveness of the numerical discretization method for the dispersion terms of the horizontal momentum equations was applied to the BVC method. The models of the BVC method (see Table 2.1) later then compared with a non-hydrostatic 3DC model, NaysCUBE (Kimura et al., 2009; Shimizu et al., 2020); the solver is available in the public domain in the iRIC river software package (Kimura, 2020).

3.2.2 Calculation conditions for flat bed cases

To validate the capability of the proposed method, it was compared with two sets of experimental data for curved channels obtained by Rozovskii (1957) and de Vriend (1979). A sharply curved channel is shown in Figure 3.1(a), and a mildly curved channel is shown in Figure 3.1(b). Table 3.1 summarizes the channel geometries and hydraulic conditions for each case.

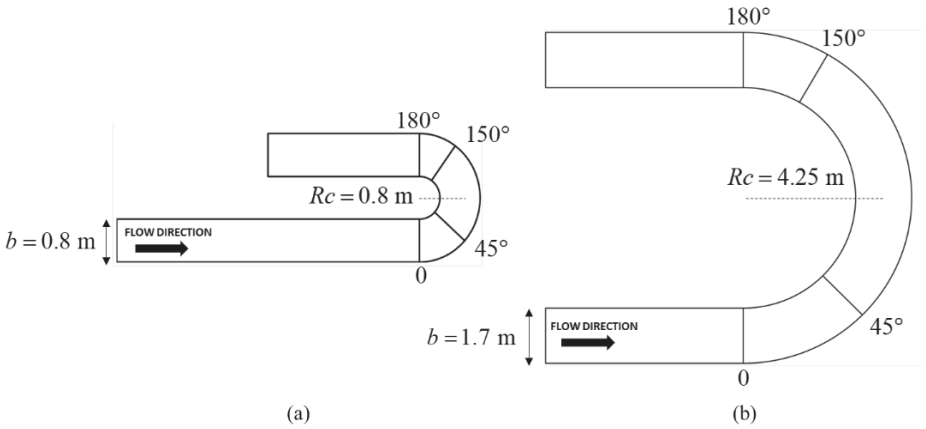

Figure 3.1 Configuration of channels: (a) sharply curved channel, (b) mildly curved channel.

A sharply curved channel has a 180° bend with a rectangular cross-section connected with a straight inlet and outlet. The lengths of the upstream and downstream channels were 6 m and 3 m, respectively. The ratio of the mean radius of curvature to channel width was 1.0. The channel width was 0.8 m, and the internal radius was 0.4 m. The upstream discharge was 0.0123 m^3/s, and the downstream water depth was 0.051 m. The mildly curved channel consisted of a 6 m-long straight section upstream, followed by a 180° bend with a radius of curvature of 4.25 m, and a 6 m-long straight section downstream. The channel cross-section was rectangular with a width of 1.7 m. The ratio of the radius of curvature to the channel width was 2.5. The upstream discharge was 0.18 m^3/s, and the downstream water depth was 0.189 m.

Table 3.1 Experimental conditions for flow measurement.

Variable	Symbol	Sharply curved channel	Mildly curved channel
Upstream discharge (m^3/s)	Q	1.2×10^{-2}	1.8×10^{-1}
Downstream water depth (m)	h_0	5.0×10^{-2}	1.9×10^{-1}

Channel width (m)	b	8.0×10^{-1}	1.7
Bend angle	θ	180°	180°
Curvature radius (m)	R_c	8.0×10^{-1}	4.2
Radius-to-width ratio	R_c/b	1.0	2.5
Channel slope	S	0.0	0.0
Froude number	Fr	4.4×10^{-1}	4.1×10^{-1}
Reynolds number	Re	1.5×10^{4}	1.1×10^{5}

The calculation domain included the entire experimental channel with a computational mesh $dx = 0.1$ m, $dy = 0.05$ m, and 10 grid cells in the vertical direction (approximated $dz = 0.006$ m for 3DC) for the sharply curved channel, and $dx = 0.1$ m, $dy = 0.1$ m, and 10 grid cells in the vertical direction (approximated $dz = 0.02$ m for 3DC) for the mildly curved channel. The numbers of grid cells in the transverse direction 17 for both channels since the grid dependency shown by the root-mean-square error (RMSE) of the water surface profiles between numerical calculation models and experimental datasets does not show a significant improvement from 17 to 35 grid cells (Figure 3.3). The experimental discharge provides the upstream boundary condition, and the experimental water depth provides the downstream water depth. $k_s = 0.0073$ m for the sharply curved channel was obtained from the water surface profile in the upstream part of the channel, equivalent to the Manning coefficient n = 0.024. $k_s = 0.0005$ m was obtained for the mildly curved channel from a linear regression of the vertical velocity distribution at the upstream end using the logarithmic law of the wall (Nezu and Nakagawa, 1993), the equivalent to the Manning coefficient n = 0.011. The 3DC model utilized a linear turbulence model to evaluate the effectiveness of the BVC models, which, in contrast, utilized a zero-equation model for turbulence.

3.2.3 Calculation conditions for topographic steering case

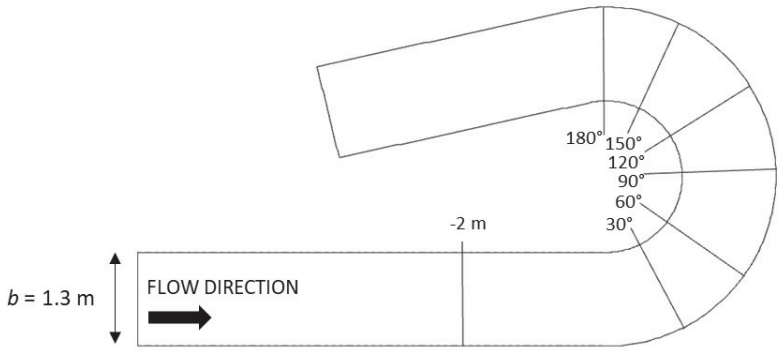

Figure 3.2 Configuration of channel by Blanckaert (2010).

Experimental dataset by Blanckaert (2010) was used to validate the models capability in reproducing flow characteristics in topographic steering case (Figure 3.2). The experimental setup comprised a flume with three sections: a 9-meter straight inflow section, a 193° curved section, and a 5-meter straight outflow section. Acoustic limnimeters were used to measure both the bed and water surface topography. The flume's vertical sidewalls were designed to be hydraulically smooth. The sand particles utilized ranged in diameter from 1.6 to 2.2 mm, with an average size of approximately 2.0 mm. The mean water depth was 0.141 m, and the discharge rate was 89 liters per second. With a flume width of b=1.3 m, the bulk velocity was 0.49 m/s, resulting in a Reynolds number of 68,000 based on this velocity and the mean water depth.

3.3 Results and discussion

3.3.1 Study on flat bed conditions and evaluation of new dispersion term

3.3.1.1 Grid dependency

Before discussion on the model validation with fine mesh, the differences in grid convergence for several models are investigated in this session. The meshes in a computational grid should be sufficiently fine to capture the flow details, but not exceedingly fine that the overall number of meshes in the domain is excessively high beyond the model ability (S. S. Y. Wang et al., 2009). To investigate the variation in the performance of the method with the grid resolution for the calculation models shown in Figure 3.3, we compared the calculation results with several grid cells with the flow widths of 35, 17, 8, 4, and 1 grid cells for the BVC method and the 2DC model. In the case of the 3DC model, the coarsest grid cell size in the transverse direction was 2. The grid size in streamwise direction was maintained to be $dx = 0.1$ because the outcomes obtained with dx = 0.05 and dx = 0.1 showed no discernible differences, but the computation time doubled.

Figure 3.3 shows the RMSE of the water surface profiles of 2DC, SBVC2, SBVC3, GBVC3, and 3DC models compared with the experimental datasets. The error value increased with grid coarsening. The 3DC model exhibited the lowest error, followed by GBVC3, SBVC3, SBVC2, and 2DC models. When the grid was the coarsest, the error value was the same for the 2DC model and the models of the BVC method because the vertical velocity distributions were not calculated with a single mesh in the transverse direction.

Figure 3.3 shows that the variation in the RMSE for each grid size is insignificant for the 2DC model because it does not account for the effect of secondary flow. According to the

investigation of the meandering channel (Lugina et al., 2021; Zhang et al., 2022), the secondary flow increases the flow resistance due to vertical momentum transfer. The vertical velocity distribution in the 2DC model is constant; therefore, the shear stress does not significantly change, nor does the water surface profile change, regardless of the grid size. Thus, the result was not significantly improved even with the smallest grid size applied to the 2DC model. Because the models of the BVC method consider the effect of the secondary flow, they show a considerable improvement upon refining the grid sizes; this result is in good agreement with the 3DC model. The GBVC3 and SBVC3 models show better results than the SBVC2 model because they employ a cubic velocity distribution with a non-equilibrium water surface velocity, whereas the SBVC2 model utilizes a quadratic velocity distribution assuming $u_{si} = U_{0i} + \delta u_{si}/3$.

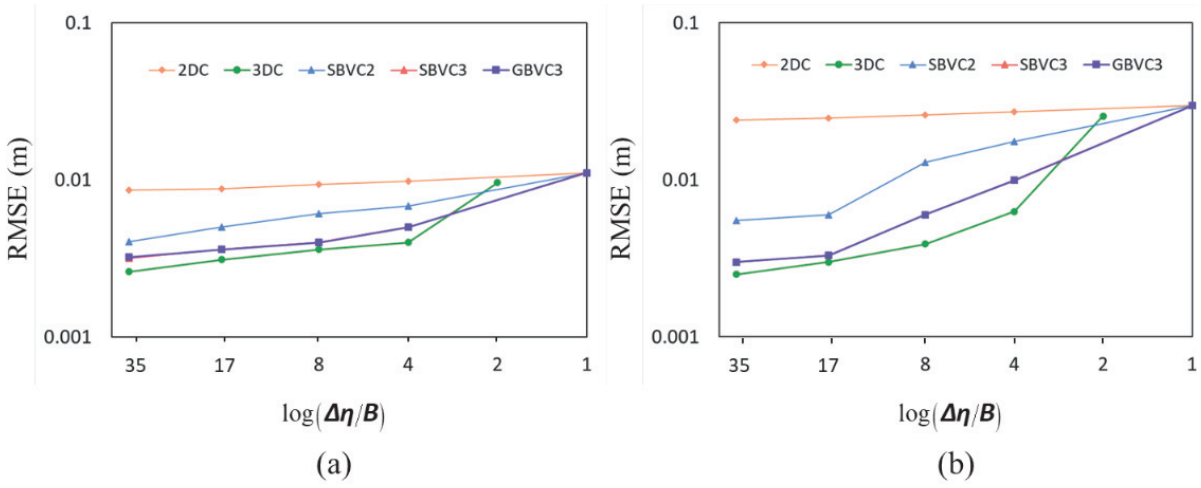

Figure 3.3 Effect of grid resolution on the water surface profile error: (a) sharply curved channel, (b) mildly curved channel.

In the numerical calculation method, the partial differential equation cannot be evaluated ideally and induces a numerical error that can be minimized by decreasing the grid size. Grid convergence is performed in the numerical verification step (Roache, 1998; S. S. Y. Wang et al.,

2009); however, as shown in the results of this study, the grid convergence effect also depends on the validity of the calculation method to the target flow. The inability of 2DC to define the water surface profile is attributed to the absence of three-dimensional considerations. In contrast, the models of the BVC method employ a polynomial velocity equation to define the vertical velocity distribution.

3.3.1.2 Water surface profile

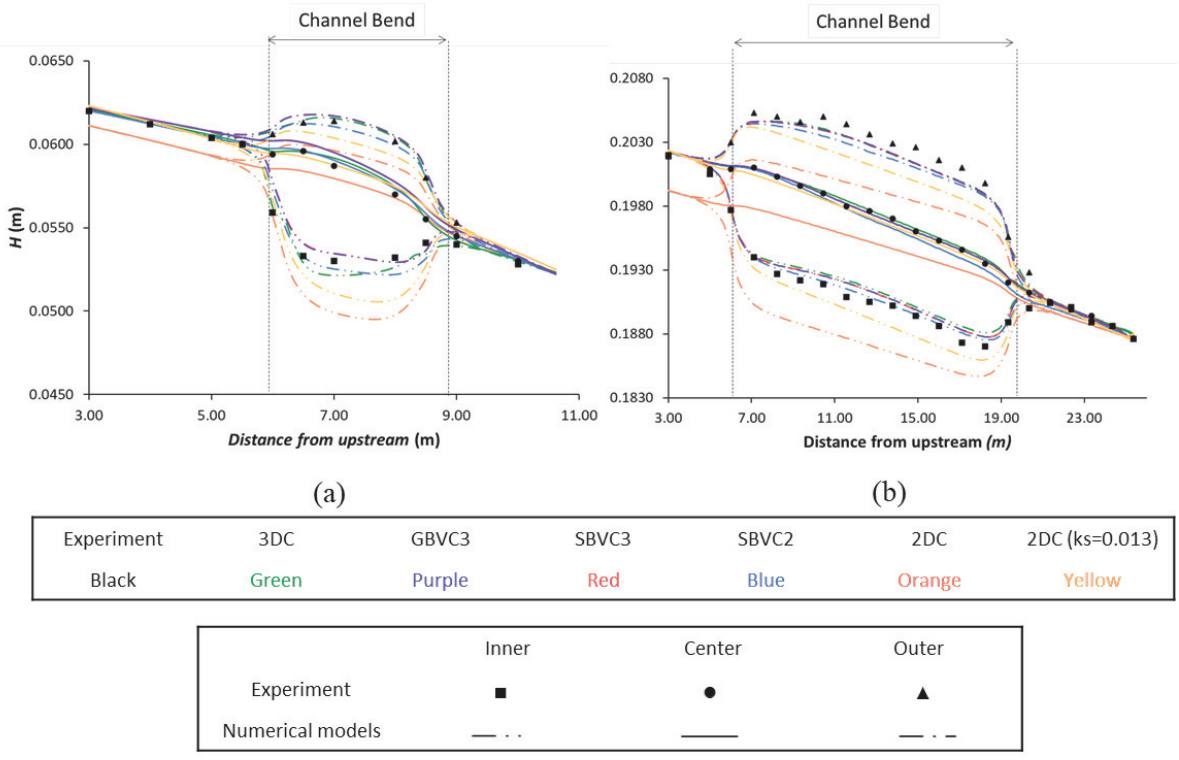

Figure 3.4 Water surface profile comparison: (a) sharply curved channel, (b) mildly curved channel.

Figure 3.4(a) and (b) show comparisons of the water surface profile along the outer and inner banks for the sharply and mildly curved channels, respectively. The water surface profile is uniform in the upstream section of the curved part. Once the flow enters the curved part, the water

surface profile increases at the outer wall and decreases at the inner wall owing to the centrifugal force effect. After leaving the bend, the water surface profile becomes uniform again.

Leopold et al. (1960), Powell (2014), and Yen (2002) mentioned that any deflection in the channel (channel bend in this study) produces an additional resistance and induces a secondary flow. The 3DC model, a fully three-dimensional model, considers the effect of secondary flow on increasing flow resistance. Therefore, it reproduces the water surface profiles of experimental datasets well. However, it still underestimates the water surface gradient in the transverse direction inside the bend. The models of the BVC method calculate the vertical velocity variation using polynomial equations [Equations (2.1, 2.2, 2.3)] by taking velocity differences between the water surface and the bottom velocity [Equation (2.10)]. In terms of shape, GBVC3 and SBVC3 exhibit a striking similarity and closely resemble the patterns observed in experimental datasets (GBVC3 result (purple line) is on SBVC3 result (red line)). Both models utilize a cubic function [Equation (2.3)] to represent the vertical velocity distribution, although GBVC3 incorporates non-hydrostatic velocity distribution while SBVC3 assumes the shallow water flows. Additionally, it was clarified that accounting for variations in vertical velocity in a depth-integrated model did not yield substantial improvements in the results, particularly in this specific condition. Although the SBVC2 model solves the vorticity equation, its assumption regarding the velocity distribution of uniform flow for the water surface velocity still leads to an underestimation of water surface profile. This underestimation is primarily caused by the presence of secondary flow, which results in an underestimated flow resistance. The longitudinal surface gradient is underestimated by the 2DC model. To fit the experimental datasets, the 2DC model requires a coarser value for k_s compared to the physical value obtained from the experimental water surface and velocity profiles. This

discrepancy arises because the 2DC model does not account for the increase in vertical momentum transfer caused by secondary flow. To address this, the 2DC model were modified by adjusting the k_s values. Specifically, the k_s values were increased from 0.0073 m to 0.013 m for sharply curved channels and from 0.0005 m to 0.0018 m for mildly curved channels, as indicated by the orange dashed line in the plot. However, even with the increased roughness coefficient, the 2DC model failed to reproduce the water surface profile accurately in the curved section. It is noteworthy that the 2DC model underestimates the water surface superelevation along the outer bank. This discrepancy can be attributed to the neglect of momentum transport in the outer-bank direction by the secondary flow in the 2DC model.

3.3.1.3 Depth-averaged velocity

Figure 3.5 and Figure 3.6 show comparisons of the depth-averaged velocity along the streamwise direction at several cross-sections of the sharply and mildly curved channels. The vertical axis represents the depth-averaged velocity U normalized by the cross-sectional averaged velocity U_0. The horizontal axis represents the distance from the left bank, proportionate to the channel width (0 is the inner bank and 1 is the outer bank).

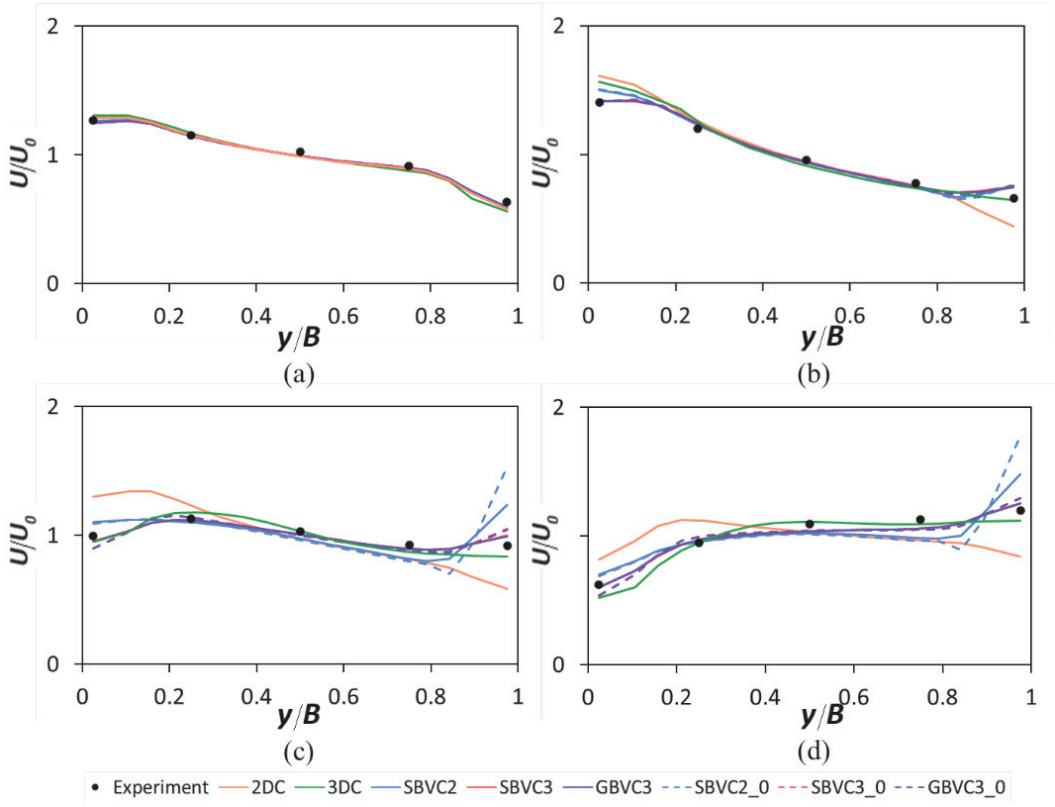

Figure 3.5 Lateral distribution of depth-averaged streamwise velocity at the sharply curved channel: (a) 0, (b) 45°, (c) 150°, and (d) 180°. The dashed lines (SBVC2_0, SBVC3_0, and GBVC3_0) show the calculation results without incorporating the numerical diffusion term in Equation (2.33)

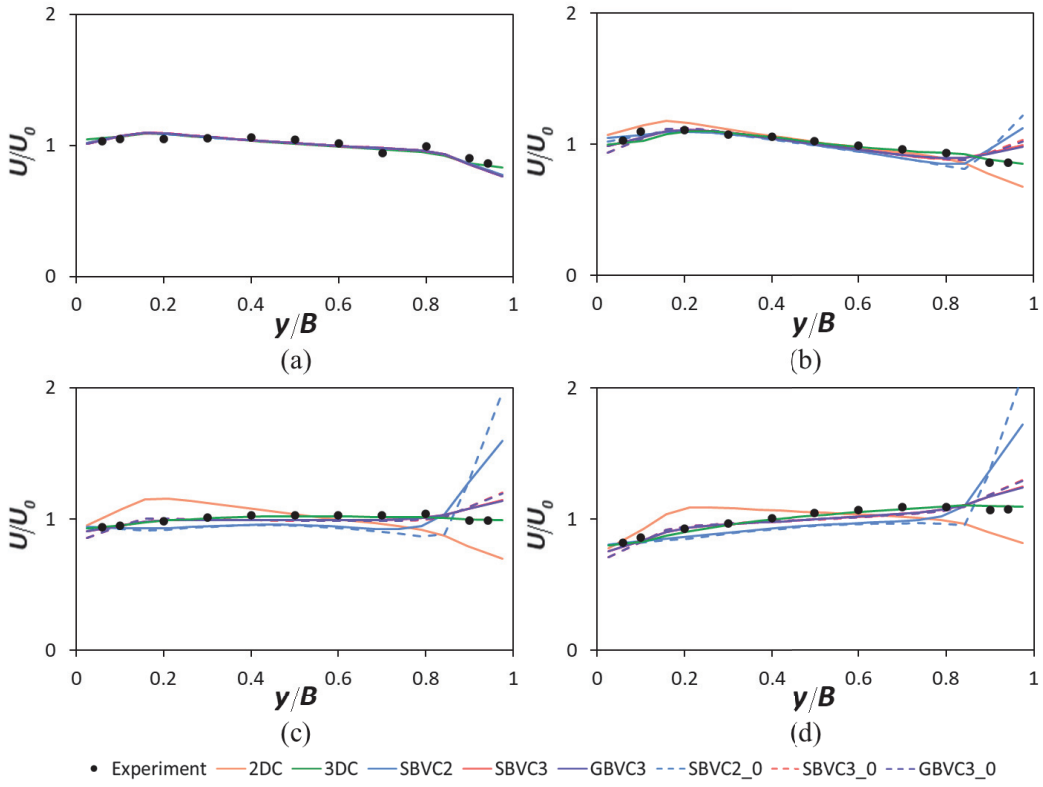

Figure 3.6 Lateral distribution of depth-averaged streamwise velocity at the mildly curved channel: (a) 0, (b) 45°, (c) 150°, and (d) 180°. The dashed lines (SBVC2_0, SBVC3_0, and GBVC3_0) show the calculation results without employing the numerical diffusion term in Equation (2.33)

A comparison was made at the entrance section of the channel bend (0), early bend (45°), late bend (150°), and bend exit (180°) for both channels. In both channels, the velocity near the inner bank experiences an increase at the entrance. As the bend section begins, the maximum velocity is observed near the inner bank, primarily due to the presence of a significant longitudinal water surface gradient, as depicted in Figure 3.4. Within the bend section, there is a gradual decrease in velocity near the inner bank, resulting from the transfer of momentum induced by the circulation of secondary flow within the channel bend. As the flow progresses towards the exit of

the bend, the maximum velocities are found near the outer bank. This phenomenon is attributed to the transverse convection of momentum transfer facilitated by the secondary flow. Although sharply and mildly curved channels both exhibit similar depth-averaged velocity distribution patterns, the strength of the depth-averaged velocity distribution over the calculated averaged velocity for each cross-section is greater in sharply curved channels. As has been found in previous studies, the potential-vortex effect triggered by the large transverse water surface gradient (Figure 3.4) in the sharply curved channel is higher than the mildly one (Blanckaert & de Vriend, 2005; Kashyap et al., 2012; Zeng, Constantinescu, Blanckaert, et al., 2008).

The 3DC model and the models of the BVC method can reproduce the acceleration of the depth-averaged velocity near the inner bank before entering the bend and the shifting of the maximum velocity toward the outer bank after leaving the bend since they consider the vertical velocity variation. Similar to water surface profiles, the SBVC3 and GBVC3 models produce similar patterns. The absence of the horizontal momentum equation on the water surface [Eq. (2.15)] in the SBVC2 model leads to the high non-physical velocity along the outer wall. The results of the 2DC model do not show the shift of the maximum velocity in the channel bend from the inner to the outer walls affected by the transverse convection of the secondary flow of the momentum transfer since the 2DC model does not consider the vertical velocity variation, as previously noted by Finnie et al. (1999). This drawback in 2DC caused the underestimation in velocity along the outer bank, and a uniform-like velocity pattern can be observed after leaving the bend in the 2DC model that underestimates the water surface profile along the outer bank.

The effectiveness of the proposed numerical discretization method for the dispersion terms of the horizontal momentum equations applied to the models of the BVC method was examined as

follows. The dashed lines show the calculation results without incorporating the numerical diffusion term D_{ij} in Equation (2.33). It can be noticed that the absence of the numerical diffusion term D_{ij} leads to high velocities along the outer bank that occurred in the two channels induced by the unphysically high momentum transfer that could not be dumped at the outer bank. As a result, the proposed numerical discretization method successfully improved the calculation of velocity along the outer bank, preventing from unphysical large momentum transfer. The dispersion viscosity, as defined in Equation (2.34), plays a crucial role in altering the depth-averaged velocity profile in contrast to the eddy viscosity, as described in Equation (2.9). This is primarily due to the prevalence of secondary flow along the curved channel, which amplifies the influence of dispersion viscosity.

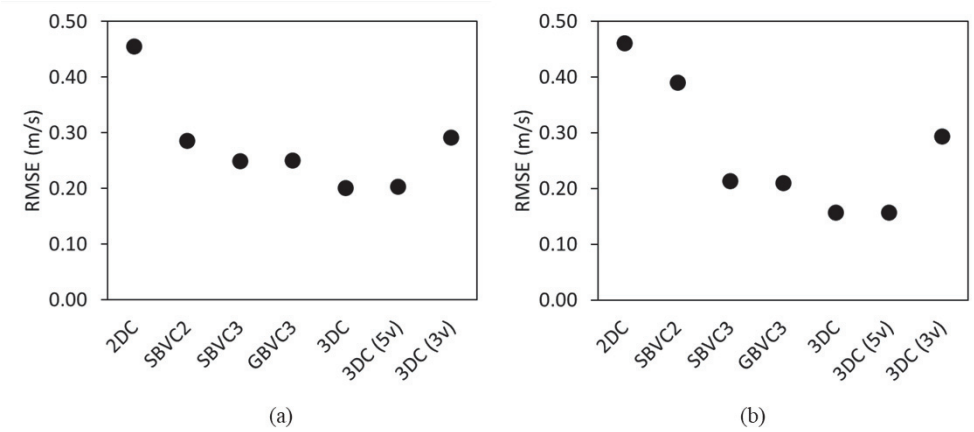

Figure 3.7 RMSE of depth-averaged velocity between numerical calculation and experiment datasets varying with several number of vertical grid on 3DC model: (a) sharply curved channel, (b) mildly curved channel.

Figure 3.7 shows RMSE between experimental dataset and numerical calculation results with some additional results obtained by 3DC model for three and five vertical grid numbers in

sharply and mildly curved channels. 2DC model without incorporating vertical velocity consideration resulted the biggest error in depth-averaged velocity distribution. While the models of the BVC method can reduce the error since they consider the vertical velocity distribution. The SBVC3 and GBVC3 have a smaller error compared with the 3DC model with three vertical grid numbers.

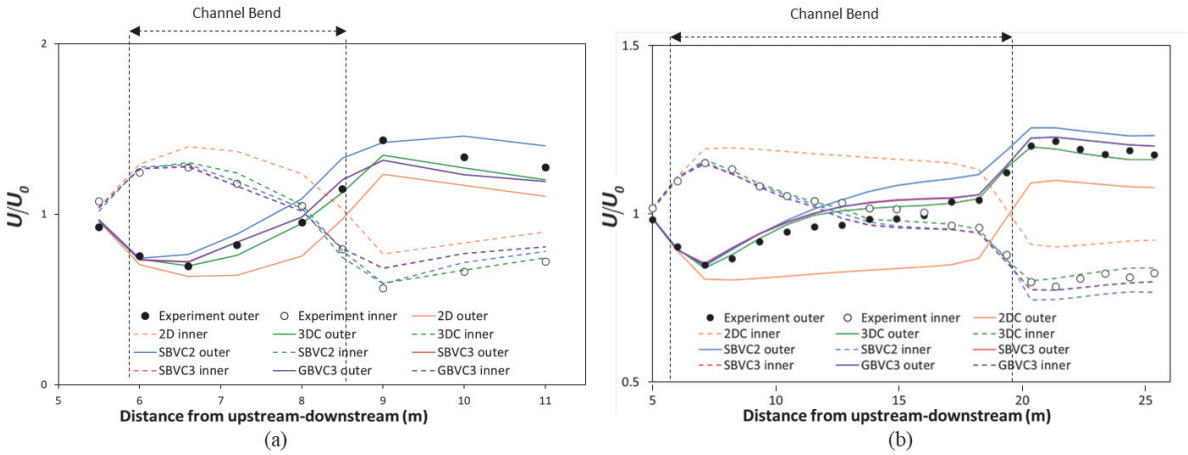

Figure 3.8 Distribution of depth-averaged streamwise velocity along the inner and outer bank for the (a) sharply curved channel (b) mildly curved channel.

Figure 3.8 shows the depth-averaged velocity distribution along the inner and outer banks of the sharply and mildly curved channels. The vertical axis represents the depth-averaged velocity U along inner and outer banks normalized by U_0 the calculated averaged velocity for each cross-section. The horizontal axis represents the distance from upstream to downstream of the channels. The distribution and shifting of the depth-averaged velocity along the channels are more pronounced in Figure 3.8 than what is shown in Figure 3.5 and Figure 3.6. The depth-averaged velocity distribution shows a uniform pattern in the upstream part of the channel, that is, a straight

channel. At the bend entrance, the velocity close to the inner bank is dominant until it decreases and gradually shifts to the outer bank when it reaches the bend exit.

The 3DC model and the models of the BVC method can reproduce the distribution of the depth-averaged velocity along the inner and outer banks, they are in the same manner as water surface profiles and depth-averaged velocity distribution. It is more prominent that the models of the BVC method still overestimate the results of the experimental datasets and the 3DC model. However, some discrepancies remain resulting from the 3DC model as well. While the overestimated result of the BVC method may be triggered by the zero-equation model in the turbulence model, the inability of 2DC to describe the effect of secondary flow on the distribution of depth-averaged velocity is notable.

3.3.1.4 Vertical velocity distribution

Figure 3.9 and Figure 3.10 show vertical velocity distribution of the sharply and mildly curved channels, respectively. The vertical axis represents the distance from the bed to the water surface ($\eta = 0$ at the water surface to $\eta = 1$ at the bed). The horizontal axis represents the vertical velocity profiles at the left, the center, and the right of the banks. A comparison was made at the entrance section of the channel bend (0), early bend (45°), late bend (150°), and bend exit (180°) for the sharply and mildly curved channels.

The streamwise vertical velocity distribution for both channels take maximum values around the water surface at the beginning of the bend. Once flow enters the bend, the secondary flow is formed and deforms the distribution of streamwise vertical velocity distribution, especially close to the banks. It was pointed out the deformation of streamwise velocity distribution along the bend, a secondary flow that transports advective momentum flattens the streamwise velocity

by increasing or decreasing velocities in the lower or upper part of the water column (Blanckaert and De Vriend, 2003; Blanckaert and Graf, 2004). As for the transverse vertical velocity distribution of both channels show uniform profiles at the beginning of the bend. Once flow enters the bend, the flow at the surface moves outward while the flow at the bottom moves inward. When the flows leaving the bend apexes, outer bank cells formed (at cross-section 150^{o} and 180^{o}) indicated by the decreasing velocity at the water surface. The outer bank cells in the mildly curved channel looks more pronounced than in the sharply curved channel, it is caused by the traveled distance is longer in the mildly curved channel. A shorter travel distance in the sharply curved channel can be seen from an acceleration appearing near the water surface on the right bank (Fig. 10(b), at 45^{o}) compared to the situation observed in the mildly curved channel (Figure 3.10(b), at 45^{o}). This acceleration might be attributed to the combination of short travel distance in the sharply curved channel and significant momentum transfer toward the outer bank (right bank) due to the secondary flow generated by the imbalance of centrifugal forces, which continued developing up to 90^{o}.

(a) Stream wise velocity profiles

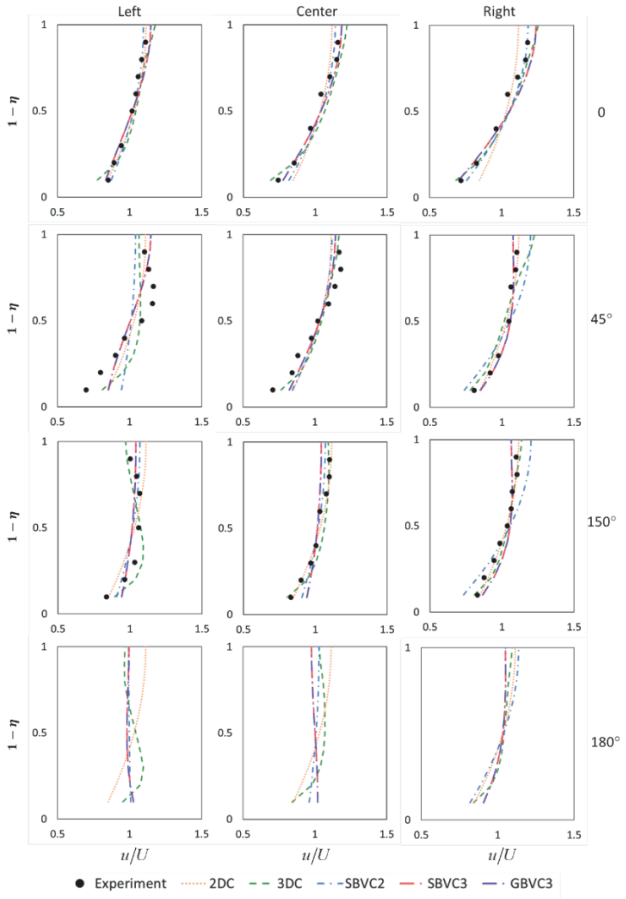

(b) Transverse velocity profiles

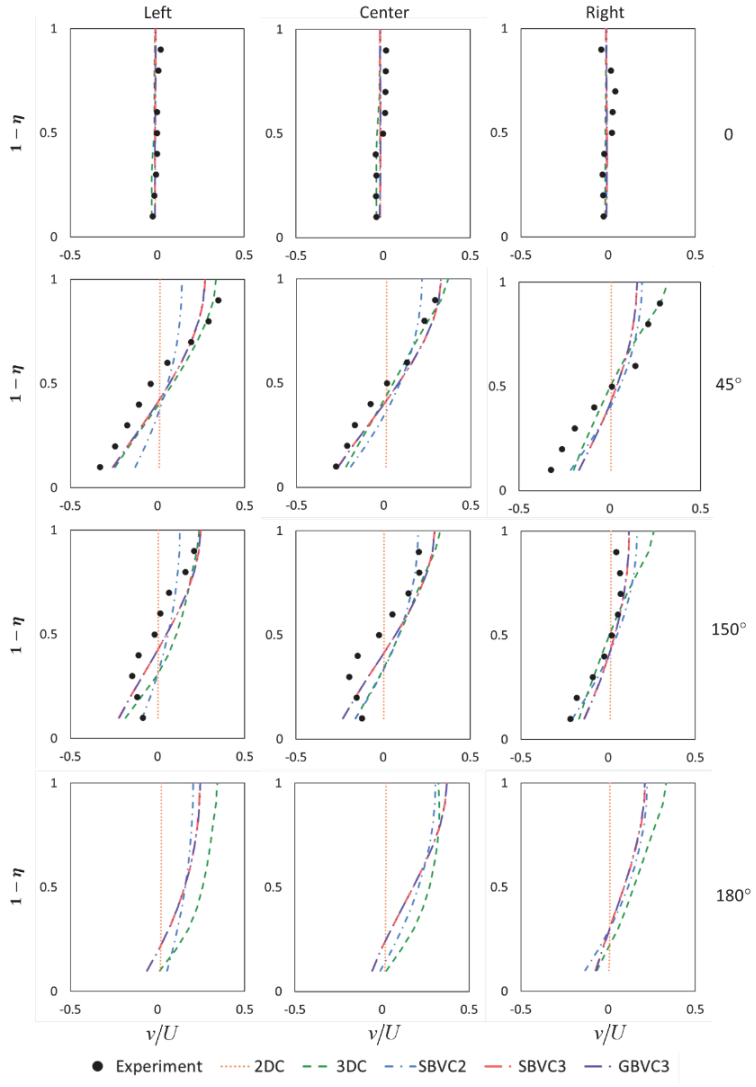

Figure 3.9 Vertical distribution of the sharply curved channel.

(a) Stream wise velocity profiles

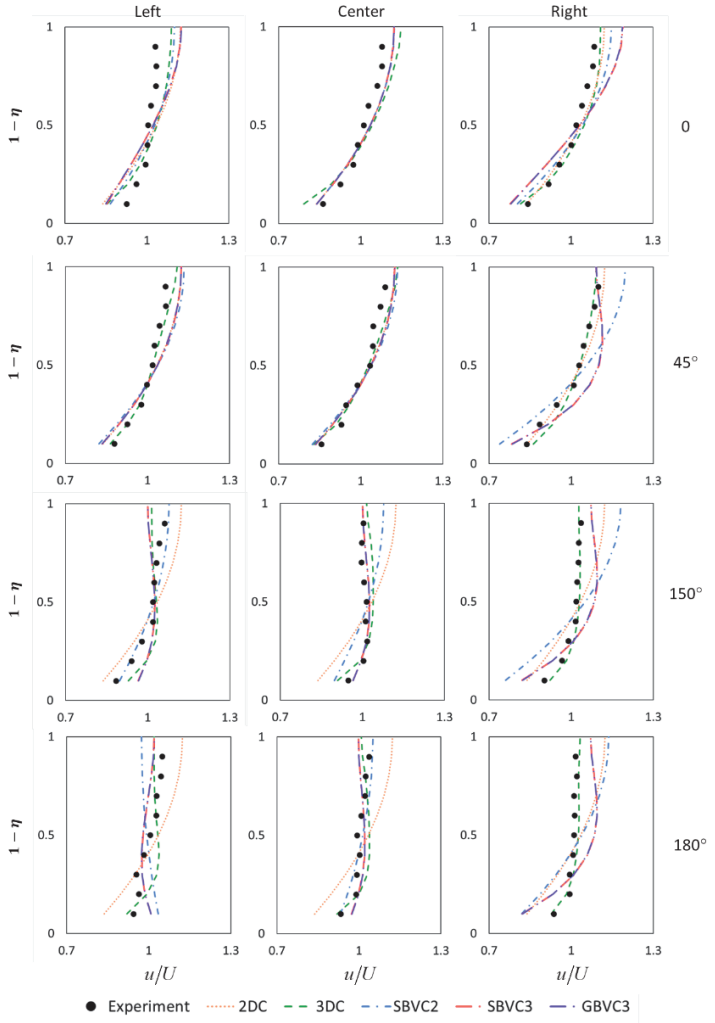

(b) Transverse velocity profiles

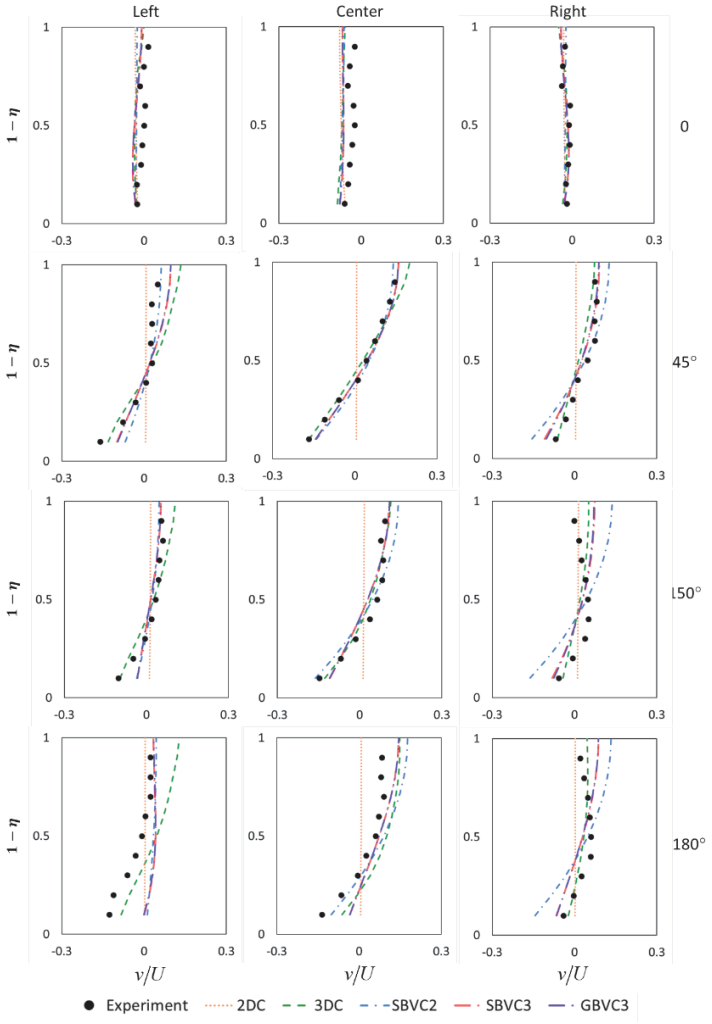

Figure 3.10 Vertical distribution of the mildly curved channel.

The 3DC model produced the vertical velocity distribution measured by the experiments well, especially close to the banks. It can dump high velocity at the outer banks compared with other numerical models. However, there are some discrepancies in reproducing the outer bank cell for the mildly curved channel. The models of the BVC method can consider the vertical velocity

variation. The structure of transverse velocity, which moves outward at the water surface and inward at the bottom, can be produced as well as the effect of secondary flow on deforming the vertical streamwise velocity distribution. The SBVC3 and GBVC3 models are similar in reproducing the streamwise and transverse vertical velocity distributions. Therefore, the non-hydrostatic pressure distribution and variations in vertical velocity are not more significant than the degree of resolution in the vertical velocity function. Although GBVC3 takes into account the distribution effect of the vertical velocity component, the difference is not significant since the effect of secondary flow in this channel is not sufficiently strong. The SBVC2 model produces higher velocity distribution especially in the water surface than SBVC3 and GBVC3.

3.3.2 Study on bed topographic steering case

3.3.2.1 Water level elevation

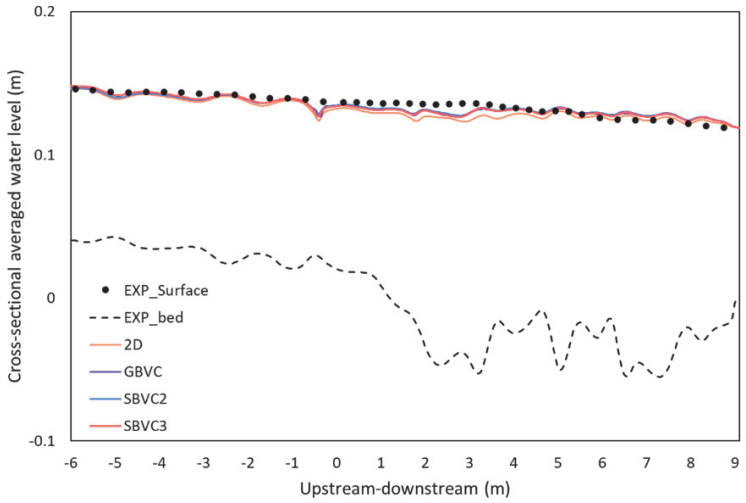

Figure 3.11 Cross-sectional average of water level comparison in longitudinal direction between experimental dataset and numerical model results.

Figure 3.11 shows a comparison of cross-sectional average of water level elevation in longitudinal direction. Despite the complexity of bed topography profile, the BVC models are able to reproduce the slope of water level in cross-sectional average form, while 2D model underestimates the result. A closer look at the profile in a channel cross-section can be found in Figure 3.12. The superelevation of water surface can be reproduced by the model characterized by higher water surface at the outer bank. At the beginning of curvature, all the models underestimate the results from experimental dataset that can be attributed to the complex structure of bed topography where maximum scouring and deposition are located.

Bed topography can promote very complex flow structures (Blanckaert, 2010) that will be difficult to be captured by the models indicated by underestimation of the model results. However,

when the flow reaches bend exit (180), the BVC models can reproduce superelevation of water surface that can be attributed to the weakening of three-dimensional flow structures. The advantage of considering non-hydrostatic assumptions is confirmed by GBVC3 over SBVC3 results that resemble closer profile with the experiment dataset. The absence of horizontal momentum at the water surface consideration leads to an overestimate result shown by SBVC2. The transverse water surface gradient is underestimated by the 2DC model because the 2DC model does not account for the increase in vertical momentum transfer caused by secondary flow.

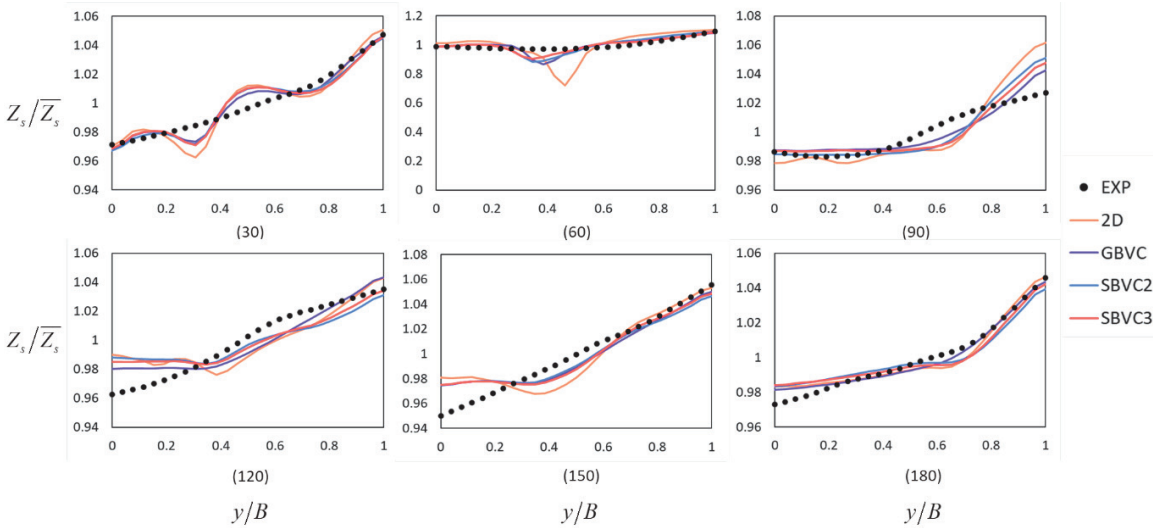

Figure 3.12 Cross-sectional comparison of water level between experimental dataset and numerical model results. $\overline{Z_s}$ is cross-sectional average of water level.

3.3.2.2 Vertical velocity structures

Figure 3.13 and Figure 3.14 show vertical velocity distribution in streamwise and transverse direction, respectively. The vertical axis represents the distance from the bed to the water surface ($\eta = 0$ at the water surface to $\eta = 1$ at the bed). The horizontal axis represents the vertical velocity

profiles at the left, the center, and the right of the banks. A comparison was made at the 30°, 60°, 120°, and 180°. There is no available data for cross-section 60° and 120° along the left bank because the huge deposition exists. A large-eddy simulation (LES) (Van Balen et al., 2009) was accounted for vertical velocity comparison with BVC models result.

The LES model still show small discrepancies compared to experimental dataset, that may be triggered by the existence of the small-scale dunes, the spatial resolution of the model was not sufficient to resolve the details of the dunes (Van Balen et al., 2009). The BVC models results show a variation, at some cross-section there is a good agreement between BVC models, experimental dataset, and LES model, but at some cross-section not. For overall qualitative results, BVC models are rather good compared to experimental dataset and LES model.

Generally, bottom velocity of GBVC3 becomes accelerated compared to SBVC3 and SBVC2 due to the effect of non-hydrostatic pressure assumptions that consider the vertical velocity distribution. SBVC2 tends to follow linear profile of velocity distribution like 2DC model due to the absence of consideration on horizontal momentum equations at water surface and consideration of quadratic polynomial equation for the vertical distribution of velocity.

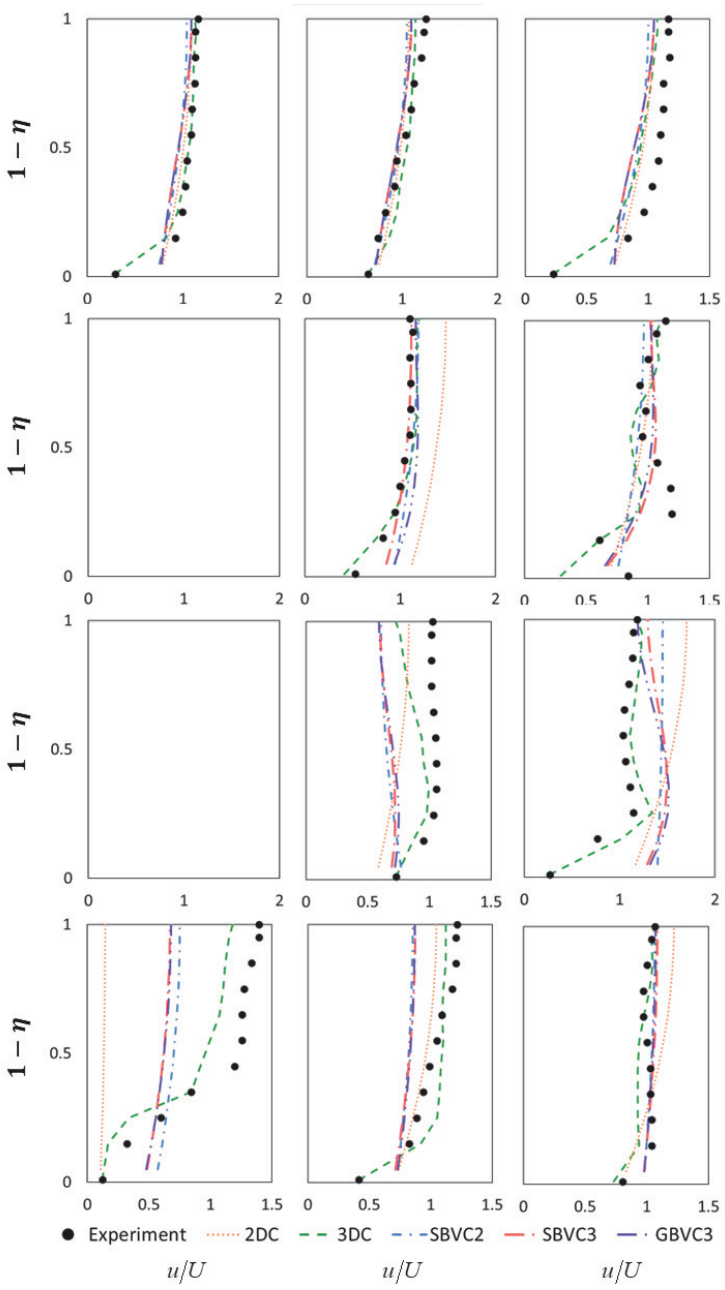

Figure 3.13 Vertical velocity distribution in streamwise direction comparison between experimental dataset and numerical model results.

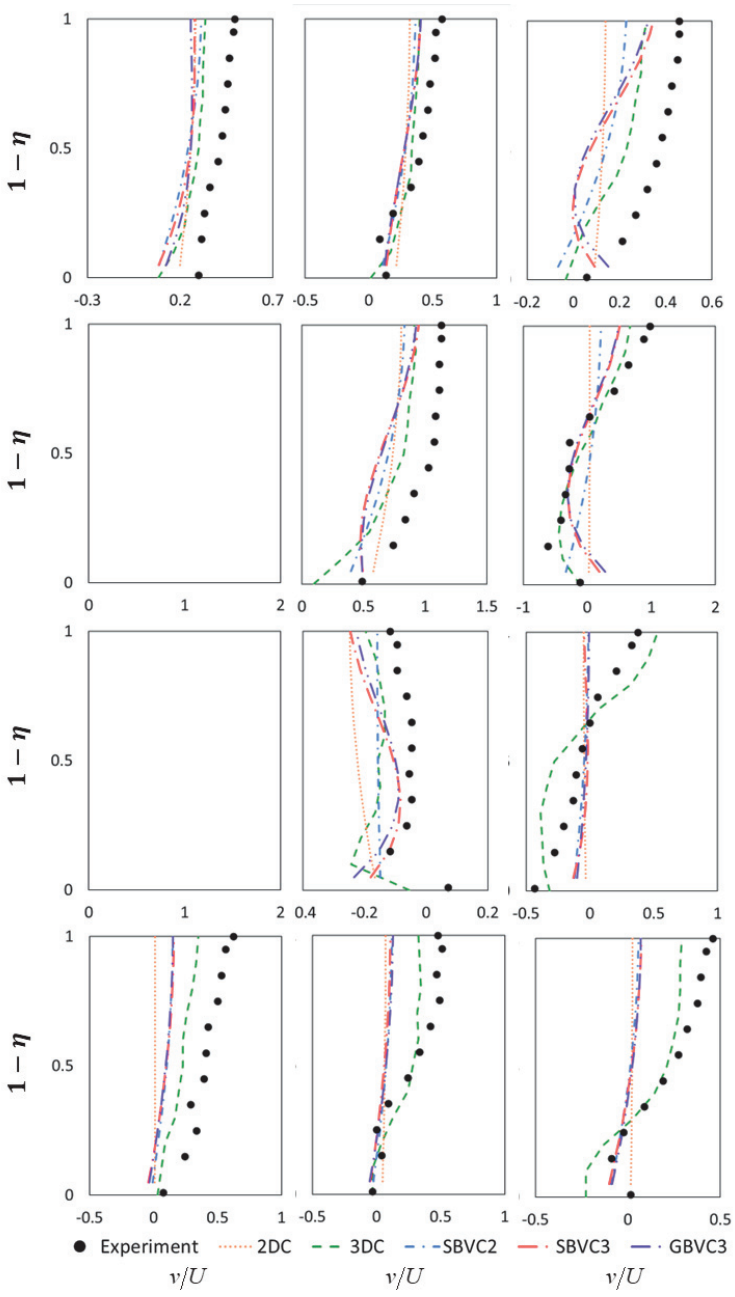

Figure 3.14 Vertical velocity distribution in transverse direction comparison between experimental dataset and numerical model results.

3.4 Conclusion

In this study, several types of numerical calculation models were compared in order to investigate the performance of coupling several equations in a depth-integrated model. Furthermore, a numerical discretization method for the dispersion terms of the horizontal momentum equations was proposed to prevent an unphysical phenomenon along the banks of the channels. The numerical calculation models were validated in sharply and mildly curved channels, then applied to a bed topographic steering case. The significant findings of this study on flat bed are as follows:

a. The models of the BVC method were in good agreement with the 3DC model in terms of the sensitivity of grid dependency and reproducing the water surface profile from the measurement data.
b. The 2DC model cannot predict well the water surface profile in curved channel because of the inability to consider the increase in flow resistance due to secondary flow. In addition, even with modified roughness coefficients to reproduce the increased channel resistance, 2DC underestimated the water surface elevation along the outer bank.
c. The proposed dispersion method can avoid excessively high velocities along the wall that is a drawback that has been overlooked in advanced depth-integrated models. By incorporating the dispersion term, it is demonstrated that the BVC method can reproduce the experimental water levels and velocity profiles in the channel bend, including those along the outer bank, with the same accuracy as that of the full three-dimensional model.
d. It was investigated that incorporating a vertical velocity component into an advanced 2DC model will not have much impact for flow in curved channels in this study.

After confirming the applicability of the models of the BVC method with the discretization scheme in dispersion terms, the models were then extended to be applied to the bed topographic steering case. Although the models cannot reproduce the experimental dataset well, but overall qualitative results, the models are rather good compared to experimental dataset.

Chapter 4 Flow resistance of meandering channels with different aspect ratio, bed roughness, and sinuosity

4.1 Introduction

Flow resistance in a river influences local flow depth and velocity distribution and determines its morphology. (Chanson, 2004; Chaudhry, 2007; Ferguson, 2010; Henderson, 1966; Rhoads, 2020). It is described by well-known equations, e.g., Manning, Chezy, and Darcy-Weisbach equations, which take into account river properties and flow characteristics that induce resisting forces or an energy loss. Accurate estimation of flow resistance not only defines river's conveyance capacity and sediment transport (Ferguson, 2010; Gladkov et al., 2021; Latosinski et al., 2022; Palucis et al., 2018; Rhoads, 2020), but also helps to predict flow-stage relation and flood propagation in rivers (Uchida et al., 2014), evaluate flood risk (Khatua et al., 2012; Nezhad et al., 2022; Yagi et al., 2022), design effective hydraulic structures (Ghaderi et al., 2021; Saghebian et al., 2020).

Flow resistance in open channels shares fundamental similarities with that in closed pipes (Henderson, 1966; Leopold et al., 1960) and can be classified into three main types: skin resistance, spill resistance, and distortion resistance (Leopold et al., 1960; Powell, 2014; Yen, 2002). Skin resistance is exerted by boundary surface, such as riverbed or riverbanks. Spill resistance is related to a sudden reduction in velocity, such as a partly opened valve in a piping system or at the base of a waterfall in open-channel flow. Distortion resistance is induced by a boundary feature such as a channel bend, which deflects the flow from its original direction, it promotes secondary flow structures that increase bottom shear stress. From the momentum point of view, flow resistance

should be separated from the internal force, which is the momentum exchange between the fluids, and should be an integral force per unit area at the river boundary. This force is categorized into surface drag caused by shear forces and form drag due to boundary layer separation with pressure reduction within fluid mechanics (Rouse, 1978). Nonetheless, the introduction of the energy dissipation concept for elucidating flow resistance adds an additional layer of complexity to the concept. For example, secondary flows cause energy loss in a river bend due to the energy transition from mean flow to turbulence by an energy cascade process (Nezu & Nakagawa, 1993; Yagi et al., 2022). This energy loss process is known to increase the risk of water level rise, scouring and erosion damage (Yagi et al., 2022), which must be explained by the increase in forces acting on the boundary of the rivers, i.e., flow resistance.

Lugina et al. (2021) conducted a study delving into the impact of channel shape on flow resistance within both straight and meandering channels. They found that flow resistance in the meandering channel is higher than in the straight one due to the momentum transfer caused by secondary flows generated by channel bends. In straight channels, secondary flows are induced by turbulence anisotropy (Nezu & Nakagawa, 1993; Z.-Q. Wang & Cheng, 2006), typically weaker to those in curved or meandering channels induced by the vertical unbalanced force distributions between centrifugal acceleration and radial pressure gradient (Blanckaert & De Vriend, 2003, 2004, 2010; Blanckaert & Graf, 2001; Falcon, 1984; Nikora & Roy, 2012). According to Nezu and Nakagawa (1993), when a channel's aspect ratio $\left(B/h\right)$ falls below the critical value of 5 - indicating a narrow channel - the intensity of the secondary flow will be significant. Numerous studies investigating the correlation between aspect ratio and secondary flow strength have been conducted in straight channel (Jing et al., 2019; Shinneeb et al., 2021; Takakua & Fukuoka, 2020;

Vinuesa et al., 2018), in curved channel (Kashyap et al., 2012), and in meandering channel (Zhang et al., 2022).

As computer hardware and software continue to rapidly evolve, numerical models have become increasingly popular for evaluating flow resistance in open channels. Zhang et al. (2022) applied a three-dimensional (3D) model to investigate the effect of sinuosity and aspect ratio on flow resistance considering that their numerical model have enabled to approximate the solution. However, the application of 3D models for flow resistance assessment remains expensive (D'Ippolito et al., 2021). In fact, horizontal two-dimensional analyses have been used to predict flood flows in a river network with tributaries and variation in river morphology with sediment transport (Uchida et al., 2014; Shimizu et al., 2020). For this reason, several advanced depth-integrated models with the ability to evaluate vertical velocity and pressure distribution have been developed to account for internal momentum transport and forces on the channel boundary (Ghamry & Steffler, 2005; Jin & Steffler, 1993; Uchida et al., 2016; Uchida & Fukuoka, 2014, 2019; Yeh & Kennedy, 1993). The above advanced depth-integrated models can take into account the energy cascade due to three-dimensional eddy motion, which is excluded in two-dimensional analysis, and are expected to dramatically improve the applicability to the flow resistance prediction. For example, numerical investigations with the bottom velocity calculation (BVC) models revealed that the horseshoe vortex around submerged boulders in gravel bed rivers generates vertical momentum exchange and increases shear stress on bed in addition to the drag force on them (Uchida et al., 2016). In other words, the merit in utilizing an advanced depth-integrated model not only results in better outcomes compared to conventional two-dimensional

(2D) models, but it also can provide the direct extraction of 3D flow influences on flow resistance attributed to channel shape.

This study investigates the flow resistance resulting from shear forces in meandering channels, by integrating laboratory experiments with numerical models featuring uniform width and rectangular cross-sections. The study specifically concentrates on distortion resistance and skin resistance, while excluding the consideration of spill resistance and form drag effects. The study has two primary objectives. Firstly, to examine the impact of channel shape, aspect ratios, and bed roughness on flow resistance through laboratory experiments. In this study, a combination of factors was explored to gain a more comprehensive understanding of flow resistance. Secondly, the study aims to validate the effectiveness of BVC models in simulating the impact of different factors on flow resistance and to investigate flow resistance in channels with different sinuosity.

4.2 Experimental setup

4.2.1 Laboratory experiment

The laboratory experiments were conducted at the Hydraulic Experimental Facility of Hiroshima University that aimed to explore three parameters affecting flow resistance: channel meander, aspect ratio (B/h, B: width, h: depth), and bed roughness. To assess the effect of channel meander on the flow resistance, the experiments were conducted on both straight and meandering channels, as depicted in Figure 4.1. The length of these channels was 16 m in the straight direction, with a width B of 0.39 m. The meandering channel featured a maximum deflection angle of 52.99°, a meandering length of 8.06 m in a wavelength of 6.43 m, and a sinuosity of 1.25. To evaluate the influence of aspect ratio B/h on flow resistance, four cases with various B/h ranging from 2.6 to

7.0, including the critical value of the narrow channel $B/h = 5.0$ classified by Nezu and Nakagawa (1993), were prepared. The Froude number was set at 0.47 to ensure consistent flow properties. We also minimize the effect of the Reynolds numbers by setting the minimum value in the cases was 19,231. The physical experiment condition is shown in Figure 4.1. The effect of bed roughness on flow resistance was examined by applying two bed conditions, a smooth concrete bed and a rough gravel bed with a particle size of 5-10 mm. The gravel was securely affixed to the channel bed using glue to prevent displacement.

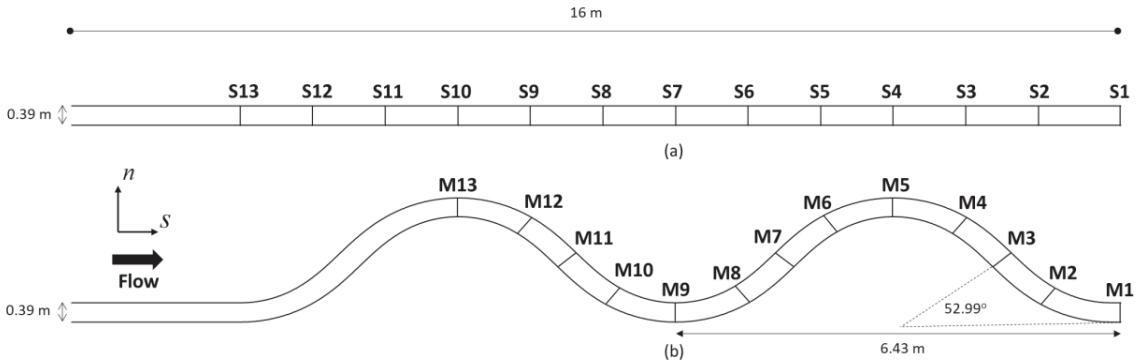

Figure 4.1 Physical experiment channels: (a) straight channel; (b) meandering channel.

Water surface elevation was measured at the center of 13 cross-sections for both straight and meandering channels using a point gauge with the level survey. The longitudinal section intervals are 1 m along the channel, in which same section between straight and meandering channels indicating the same distance from the downstream end of the channel. This yielded 16 datasets of water surface profiles for all test conditions composed of four aspect ratios, two bed conditions (rough/smooth), and two channel types (straight/meandering). Velocity distribution was measured using an Acoustic Doppler Velocimeter (ADV) (SonTek 16-MHz MicroADV) at cross-

section 9 under $B/h = 3.6$ condition for both the smooth and rough bed conditions. The resulting velocity distribution data was utilized to validate BVC models in reproducing flow structures.

Table 4.1 Physical experiment condition

Aspect ratio	*B/H*	2.6	3.6	5.0	7.0
Discharge (m^3/s)	*Q*	0.0331	0.0202	0.0124	0.0075
Downstream water depth (m)	*H*	0.150	0.108	0.078	0.056
Channel width (m)	*B*	0.39	0.39	0.39	0.39
Froude number	*Fr*	0.47	0.47	0.47	0.47

4.2.2 Numerical models

Previous research conducted by Lugina et al. (2021, 2022) demonstrated that the advanced depth-integrated models based on the BVC method (composed several BVC models: SBVC2, SBVC3, and GBVC3 (Uchida et al., 2016)) show good agreement with the experimental datasets for flows with secondary flow in curved and meandering channel. However, their study was limited to a single case (B/h = 3.6 on smooth bed). This paper aims to investigate the effectiveness of BVC models in simulating the influence of various factors on flow resistance. The BVC models calculate velocity acting on the bed using depth-integrated continuity and horizontal momentum equations along with additional equations for depth-integrated horizontal vorticity, velocity at the water

surface, the depth-integrated vertical velocity, and depth-integrated vertical velocity (Uchida & Fukuoka, 2014). Combining additional equations of motion with the depth-averaged momentum equations to account for the non-equilibrium conditions of velocity vertical profile and non-hydrostatic pressure distribution, which is excluded in the conventional 2D model, improves applicability to flow resistance evaluation. In this study, several types of depth integrated calculation models based on the BVC method indicated in Table 2.1 were compared to clarify the role of non-equilibrium flow effects in the vertical velocity distribution on flow resistance.

To fulfill ADV's requirement of submersion beneath the water surface, velocity measurements were obtained near the riverbed, specifically at a depth of 5 cm below the probe. In order to compensate for the lack of velocity distribution data from these measurements and compare the advanced depth integrated models with 2D and 3D models, the NaysCUBE model was employed as a fully three-dimensional model capable of simulating river flow and bed deformation, incorporating non-hydrostatic effects (Nelson et al., 2016). The model's accuracy has been confirmed through validation against various cases, demonstrating good agreement with experimental datasets (Suzuki et al., 2014; Sisinggih et al., 2021; Lugina et al., 2022)

After model validation, the application of BVC models was extended to investigate the impact of sinuosity on flow resistance. For the rough bed scenario, an impermeable bed condition (Nicholas, 2001) was assumed, meaning there is no water flow between the gravel. The upstream and downstream boundary conditions were given by the experimental discharge and downstream water depth, respectively. In the case of a straight channel, the computational mesh size was set to $dx = 0.1$ m and $dy = 0.039$ m, while for a meandering channel, it was set to $dx = 0.1$ m and $dy = 0.018$ m (x defined along the channel and y defined normal right angle to the channel). The

k_s value for smooth bed condition was fine-tuned to match the observed water depth in the straight channel as k_s = 0.5 mm. For rough bed condition, the k_s value was adjusted to 8.0 mm with the bed level of 0.005 m height above the smooth bed to account for the average thickness of the gravel particles layer. The equivalent roughness k_s and log-low origin height δz_b were used to evaluate the skin resistance of the bottom shear stress acting on the bed τ_{bi} :

$$\tau_{bi} = \tau_b \frac{u_i}{u_b} = c_b{}^2 u_{bi} u_b, \quad \tau_b = \sqrt{\tau_{bi}\tau_{bi}}, \quad u_b = \sqrt{u_{bi}u_{bi}} \tag{4.1}$$

where $1/c_b = (1/\kappa)\ln\left((\delta z_b + ak_s)/k_s\right) + Ar$, $i, j = 1(x),\ 2(y)$, u_{bi} : bottom velocity in i direction, $\delta z_b = 0.05h$, h : water depth, $\kappa = 0.4$, a : coefficient for the origin height of the log law ($a = 0.1$), $Ar = 8.5$.

4.3 Experimental results

Figure 4.2 shows a comparison between water surface elevations along center of the straight and meandering channels under smooth and rough bed conditions for various aspect ratios. The horizontal axis represents the distance along the channel center. In meandering channels, the water surface elevation is generally higher than that in straight channels both for smooth and rough conditions. This finding is consistent with a preliminary study by Lugina et al. (2021), which presented that the higher water surface elevation in meandering channels is caused by vertical momentum transfer with secondary flow induced by channel bends. However, this claim can hardly be confirmed for aspect ratios 7.0 under rough bed conditions (Figure 4.2(d)), where the profiles

for these conditions indicate that the water surface elevation in the straight channel has almost the same characteristics as in the meandering channel.

Figure 4.3 illustrates the assessment of flow resistance through the use of friction factor with the variation in the aspect ratio under different bed conditions and channel shapes. The friction factor for wide rectangular channel is defined by

$$f = \frac{2g}{q^2 L}\int_L h^3 i_e dx \tag{4.4}$$

where, f : Darcy-Weisbach friction factor, g : gravitational acceleration, q : flow rate per unit width, i_e : total head gradient, L : inspection channel length. For Equation (4.4) to evaluate *f*, this paper uses h in place of R (hydraulic radius) to ensure that the comparison is based on the same hydraulic characteristic for smooth and rough bed conditions, regardless of the variation in aspect ratio, which varies the effect of the side wall for the smooth bed condition. Therefore, it should be noted that, the friction factor *f* for smooth bed conditions (SS and MS) decreases gradually with increasing the aspect ratio *B*/*H* due to the decreasing in the side wall shear stress. On the other hand, in the case of rough bed conditions, the friction factor tends to rise as *B*/*H* increases. This is attributed to the increase in relative roughness height $\left(k_s/h\right)$ as the aspect ratio *B*/*h* increases with decreasing water depth *h*. The larger relative roughness height, the more dominant role of bed roughness plays in determining flow resistance compared to distortion resistance. This is due to the fact that bed roughness intensifies bed shear stress and turbulence intensities (Takakua & Fukuoka, 2020; Tominaga et al., 1989), particularly in shallow water depths with rough surfaces.

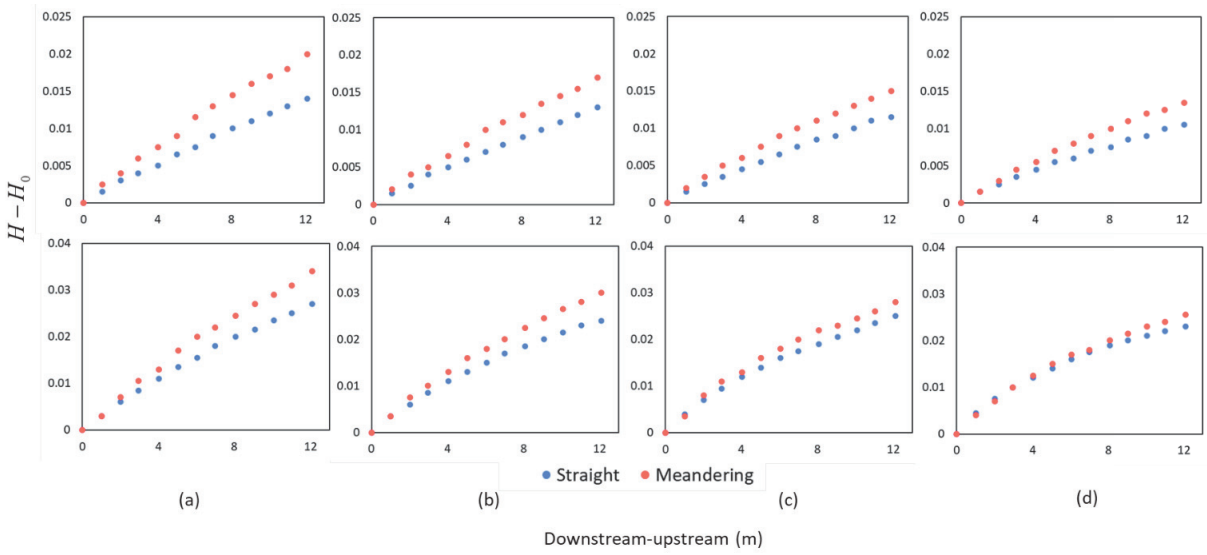

Figure 4.2 Water surface elevations of experimental results (H_0: downstream water depth) in smooth (top) and rough (bottom) bed conditions with aspect ratios: (a) 2.6; (b) 3.6; (c) 5.0; (d) 7.0.

In Figure 4.3, the meandering channels (MS and MR) exhibit higher friction factors compared to straight channels (SS and SR, respectively), indicating a greater resistance in meandering channels. This increase in friction factor can be attributed to the additional transverse bed shear stress component and the advective momentum transport in the vertical direction caused by secondary flow, these factors increase the velocity near the bed and increase bed shear stress (Blanckaert, 2009; Blanckaert & De Vriend, 2003). This mechanism generates the additional energy loss in a gently bend pipe without flow separation (Chanson, 2004; Chaudhry, 2007; Henderson, 1966), in which the strain velocity by the deformation of the velocity vertical profile generates turbulent energy and energy loss (Yagi et al., 2022).

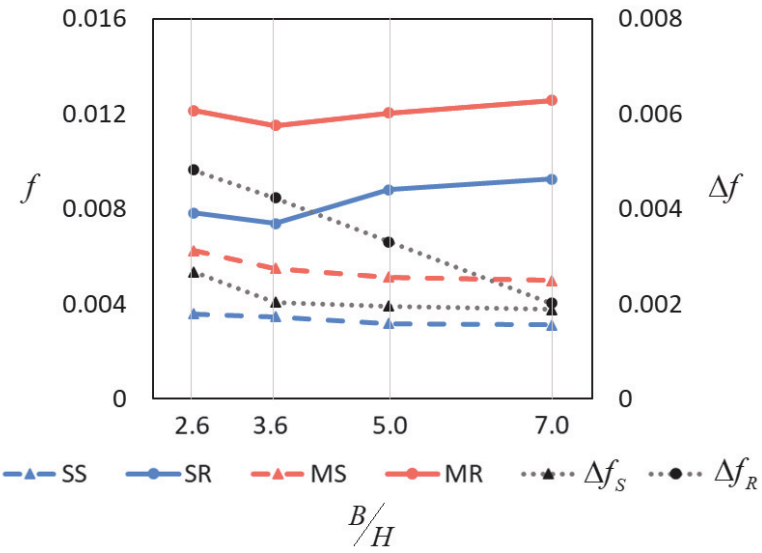

Figure 4.3 Flow resistance comparison in smooth and rough bed conditions for various aspect ratios. SS: straight-smooth; SR: straight-rough; MS: meandering-smooth; MR: meandering-rough; $\Delta f_S, \Delta f_R$: difference of friction factor between straight and meandering channels for smooth and rough bed, respectively.

The effects of channel bend on the flow resistance, such as the intensity of secondary flow that increases vertical momentum exchange and bottom velocity, are investigated with the difference in friction factor between straight and meandering channels under smooth $\left(\Delta f_S\right)$ and rough $\left(\Delta f_R\right)$ bed conditions. Both of Δf_S and Δf_R for smooth and rough bed conditions tend to increase as the aspect ratio decreases, indicating that the strength of secondary flow increases with decreasing in the aspect ratio, but this tendency is more pronounced in rough channels than in smooth channels. As previously discussed, the influence of the bed becomes more prominent with

increasing aspect ratio. The value of Δf_R exhibits an inverse relationship with k_s/h, where Δf_R decreases as the aspect ratio increases, while k_s/h increases with increasing aspect ratio.

4.4 Numerical models validation to predict flow resistance

To assess the ability of BVC models to simulate the impact of various factors on flow resistance, experimental datasets of water surface elevation were compared for smooth and rough bed in straight (Figure 4.4) and meandering (Figure 4.5) channels. In the case of a straight channel with a smooth bed, although the 2D and SBVC2 models tend to slightly underestimate the water surface elevation as B/h decreases, it can be inferred that all models accurately reproduced the experimental water surface profiles with sufficient accuracy. This suggests that the non-equilibrium velocity profile in the vertical direction has minimal impact on predicting flow resistance, which is primarily determined by the roughness of the channel bed and the depth-averaged velocity using Equation (4.3), indicating the validity of the water depth equation for gradually varied flow (Chow, 2009). However, when dealing with a rough surface, both the 2D and SBVC2 models consistently underestimate the water surface elevation for all conditions compared to the experimental results. This underestimation becomes more pronounced as B/h decreases, resulting in larger water surface elevation. Comparing this with the smooth bed case, it becomes evident that water surface elevation is larger on rough beds, indicating a higher rate of flow acceleration in the longitudinal direction. In such accelerating flows, the boundary layer near the bed remains underdeveloped, resulting in a relatively uniform velocity distribution with higher velocities near the bottom (T. Song & Graf, 1994; Uchida & Fukuoka, 2015). Consequently, the

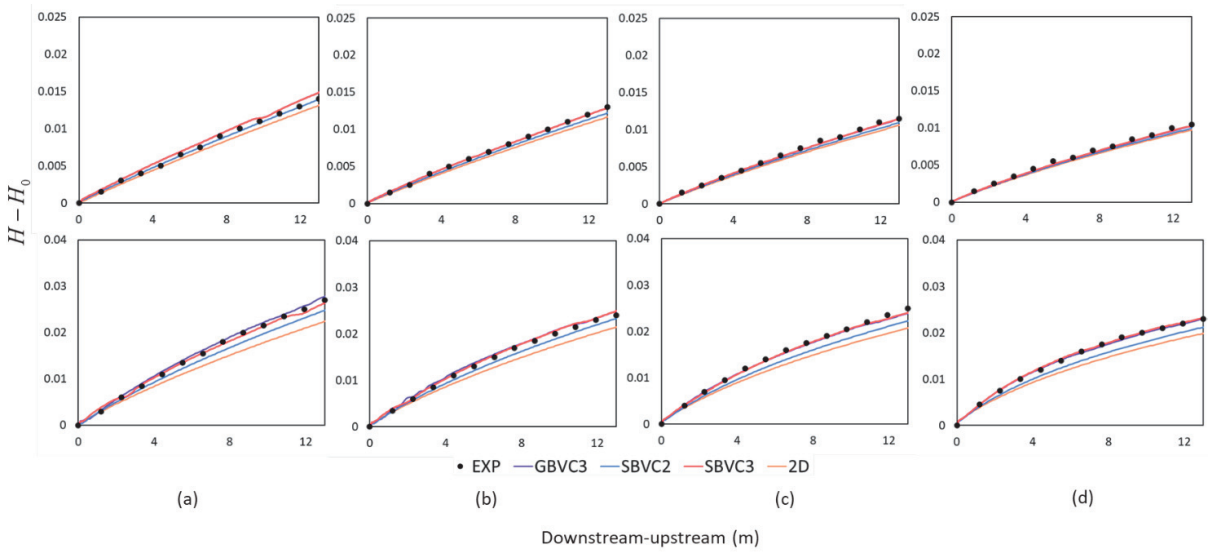

Figure 4.4 Numerical models validation of water surface elevations (H_0: downstream water depth) in straight channel for smooth (top) and rough (bottom) bed condition with aspect ratios: (a) 2.6; (b) 3.6; (c) 5.0; (d) 7.0.

2D model with the assumption of the equilibrium velocity profile is more likely to underestimate flow resistance. Although the vorticity equation is solved in the SBVC2 model, the assumption regarding water surface velocity is still based on the velocity distribution of uniform flow (i.e., $u_{si}=\left(3U_i-u_{bi}\right)/2$). It is believed that this assumption contributes to the underestimation of flow resistance and bottom velocity in accelerating flows. On the other hand, the SBVC3 and GBVC3 models successfully reproduced the experimental water surface profiles for various water depth conditions with the constant roughness coefficients for smooth and rough surfaces, indicating their validity in evaluating flow resistance under accelerating flow conditions. Furthermore, it can be observed that the influence of the assumption of shallow water flow is minimal for accelerating

flows in gradually varied flow conditions, where the flow state remains unchanged (Uchida & Fukuoka, 2015). This is in contrast to accelerating flows around critical flow conditions for rapidly

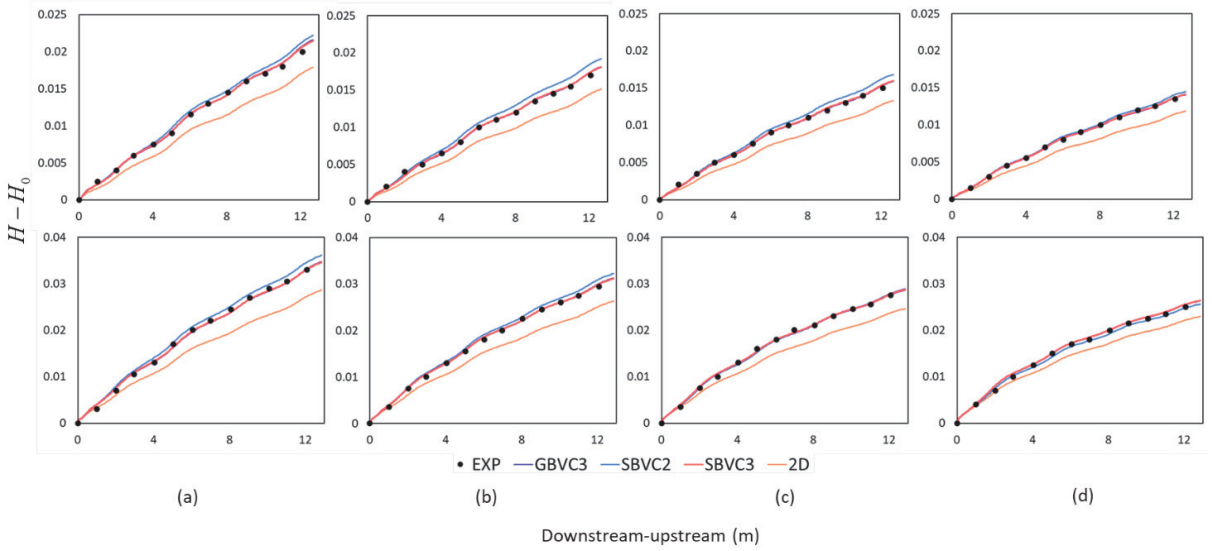

Figure 4.5 Numerical models validation of water surface elevations (H_0: downstream water depth) in meandering channel for smooth (top) and rough (bottom) bed condition with aspect ratios: (a) 2.6; (b) 3.6; (c) 5.0; (d) 7.0.

varied flows, in which the non-hydrostatic pressure component affects considerably on the water surface profile (Uchida, 2018; Uchida & Fukuoka, 2019).

While the various calculation models and experimental observations showed similar water surface profiles in a smooth-straight channel, there were notable differences when applied to a meandering channel with a smooth bed in Figure 4.5. Specifically, the 2D model considerably underestimates the elevation of the water surface. This underestimation was attributed to the model's inability to account for the increase in bottom velocity caused by vertical momentum transport with secondary flow (Lugina et al., 2021). Moreover, this underestimation became more pronounced as B/h decreased. In contrast to the trend in straight channel, the SBVC2 exhibited

a slightly higher water surface elevation in the meandering channel, indicating that the assumption of $u_{si} = \left(3U_i - u_{bi}\right)/2$ for SBVC2 puts more emphasis on the effect of secondary flow and less on the effect of acceleration on flow resistance. This characteristic was more apparent in meandering channels with rough beds. For smaller B/h values, in which $B/h = 2.6$ and $B/h = 3.6$, SBVC2 estimated the water surface elevation to be higher than the experimental results. However, as $B/h = 5.0$, SBVC2 aligned more closely with the experimental observations, and for $B/h = 7.0$, it underestimated the water surface elevation. These discrepancies were due to the diminishing effect of secondary flow as B/h decreased, while the influence of accelerated flow became more pronounced. Although SBVC2 has the advantage in terms of computational cost of omitting to calculate the equation for the water surface velocity, the disadvantages of the SBVC2 include dependency of the function of the vertical velocity to evaluate bottom velocity based on the vertical velocity profile in Equation (4.2), in which water surface velocity is evaluated with $u_{si} = \left(3U_i - u_{bi}\right)/2$. On the other hand, SBVC3 and GBVC3 reproduced the experimental water surface elevation for meandering channels with both smooth and rough beds. These models are capable of capturing momentum transport by secondary flow in meandering channels accurately. This demonstrated the high validity of SBVC3 and GBVC3 in predicting bottom velocity and bottom shear stress, as they were not directly affected by the vertical velocity distribution used to evaluate bottom flow velocity in Equation (4.2). It should be noted that SBVC3 omitted the third term in Equation (4.2) by assuming shallow-water flow. Although it is known that the effect of the shallow water flow assumption appears near the wall (Uchida & Fukuoka, 2014, 2015), there is little difference between SBVC3 and GBVC3 under the present conditions where $B/h \geq 2.6$,

indicating that the shallow water flow assumption is not a problem in the resistance evaluation for present conditions.

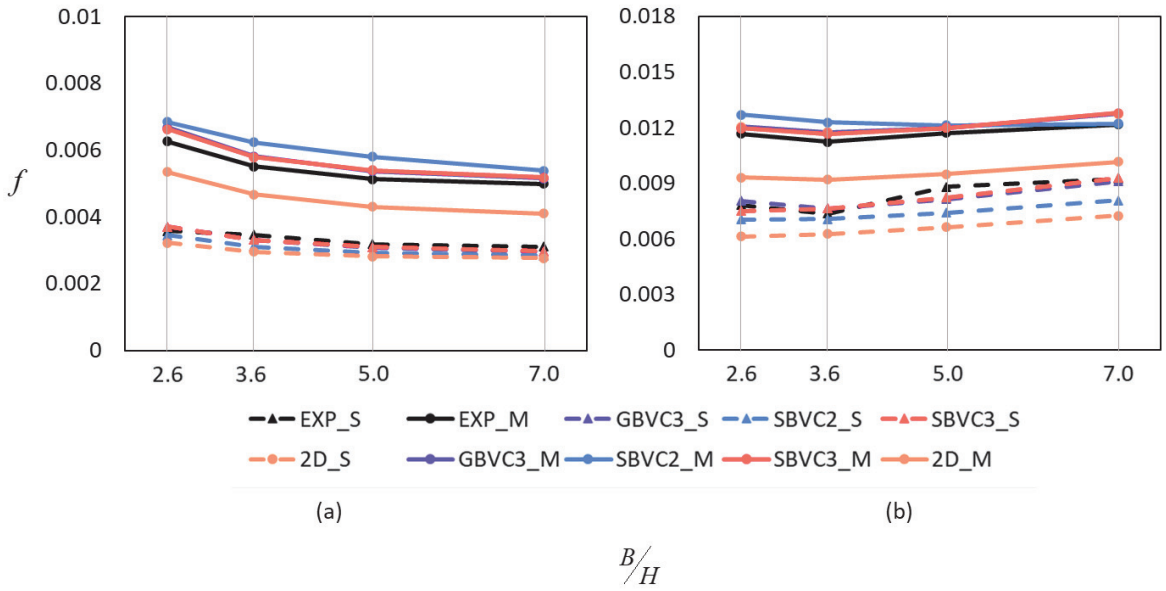

Figure 4.6 Calculated friction coefficients with various models and experiment in: (a) smooth bed; (b) rough bed. _S and _M indicate straight and meandering channels, respectively.

Figure 4.6 provides a comparison of friction factors with various models and experimental results between straight and meandering channels, for both smooth (a) and rough bed conditions (b). As expected from Figure 4.4 and Figure 4.5, the friction factor predicted with the 2D model in meandering channels underestimates the measurement result. However, it is worth noting that the 2D model is capable of considering additional flow resistance tendency due to channel meander under several aspect ratios, as demonstrated by the difference in friction factor of the 2D model between straight and meandering channels. It can be assumed that the flow resistance in the meandering channel consists of both the secondary flow structures and 2D components, with the

difference resulting from the 2D model indicating the main-flow distribution due to the meander resulting in an increase in flow resistance. The results of the comparison indicate that BVC models are able to reproduce flow resistance, showing GBVC3 and SBVC3 are the closest match to the experimental results, while SBVC2 produces a higher profile for both comparisons. The GBVC3 and SBVC3 models exhibit comparable behavior in replicating flow resistance, suggesting that the vertical velocity component does not exert a substantial influence under the current conditions. The difference between SBVC3 and SBVC2 is attributed to the horizontal momentum equation on the water surface as discussed with Figure 4.4 and Figure 4.5, where calculation of the momentum equations for water surface flows improve to predict flow resistance by flow acceleration and secondary flow.

As for velocity distribution validation, laboratory experiment and numerical model experiment were combined. Velocity distribution close to the channel bed was measured using an ADV, while a 3D model, i.e., NaysCUBE (Kimura et al., 2009; Shimizu et al., 2020), was applied to describe velocity close to the water surface. The vertical distributions of the stream-wise and transverse velocity at the center of cross-section 9 under $B/h = 3.6$ conditions by experiments and several calculations are compared in Figure 4.7 for both smooth and rough bed conditions. In the case of a straight channel, it is observed that BVC models have a tendency to overestimate the bottom velocity when compared to both the experimental datasets and the 3D results. This error may arise from the velocity distribution utilized in BVC models, which assumes a quadratic curve for the velocity distribution. While 2D models generate uniform velocity profiles, it becomes apparent that there exists a non-equilibrium velocity profile in the streamwise velocity and secondary flow by comparing the velocity profiles between BVC models and 2D models. As

indicated in Figure 4.4, while the velocity profiles are nearly identical for all calculation results in the case of a straight channel with a smooth bed condition, slight differences can be observed among the calculation models for a straight channel with a rough bed condition.

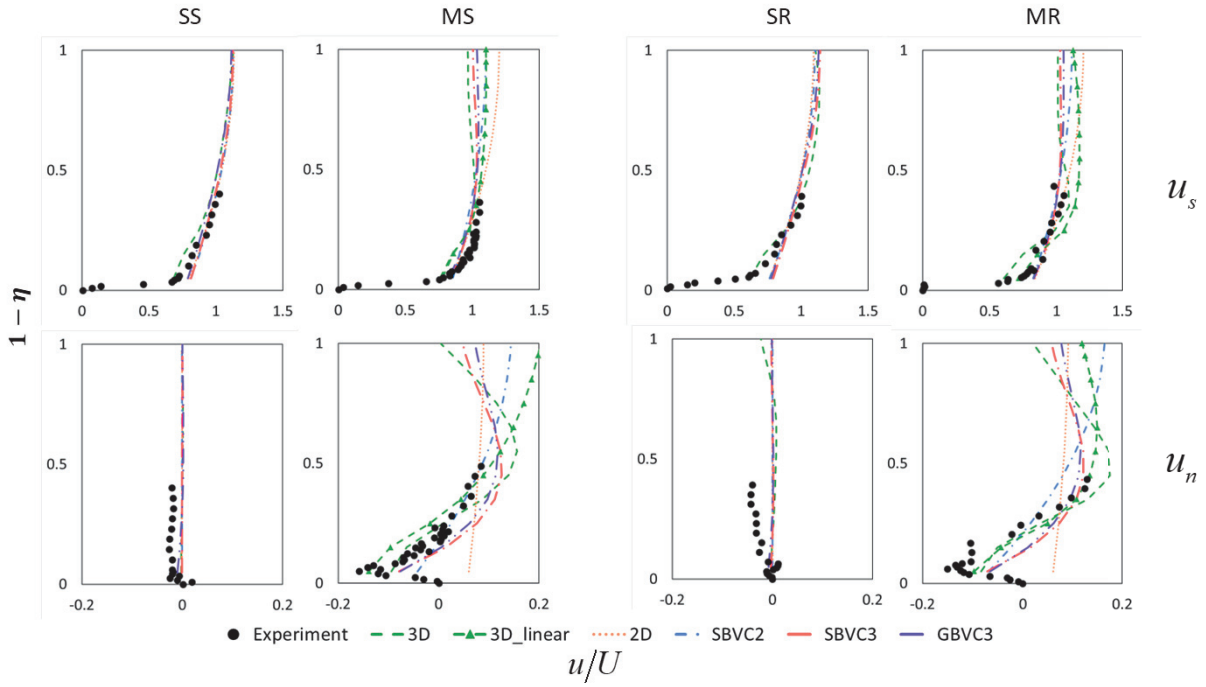

Figure 4.7 Numerical model validation of velocity distribution in streamwise (top) and transverse (bottom). SS: straight-smooth, MS: meandering-smooth, SR: straight-rough, MR: meandering-rough. The horizontal axis represents velocity magnitude, in which for transvers velocity distribution represents location for right and left banks (i.e., 0.5 is the right bank; -0.5 is the left bank). The vertical axis represents the distance from the bed proportionate to the water depth (i.e., 0 is the bed; 1 is the water surface).

On the other hand, a comparison of the experimental results for meandering and straight channels shows that in both of the smooth and rough bed conditions, the vertical distribution of the main flow velocity is more uniform than in the straight channel. The same phenomena observed in

straight channel cases also occur in meandering channels, where BVC models overestimate the bottom velocity when compared to experimental datasets and 3D model results. This could be attributed to the estimation of velocity distribution employed in the BVC models, i.e., log-law velocity and polynomial velocity distribution lead to the overestimation of velocity on the bed. However, a notable advantage is that these models accurately capture the presence of two vortices near the water surface and the bed, as evidenced by the analysis of transverse velocity distribution. The non-equilibrium characteristics of both the main flow velocity distribution and the secondary flow velocity distribution, as observed in the experiment and 3D model results utilizing the non-linear k-ε model, are effectively explained by SBVC3 and GBVC3. In contrast, SBVC2 exhibits a distinct velocity distribution from SBVC3 and GBVC3, supporting the findings presented in Figure 4.4 - Figure 4.6.

The 3D model demonstrates a good agreement with the experimental datasets in both straight and meandering channels, considering different bed conditions for smooth and rough bed. This further supports the utilization of the 3D model as a benchmark for BVC models to validate velocity distribution for meandering channel flows. To discern the effect of the turbulence model, linear and non-linear k-ε models were compared in Figure 4.8 for the streamwise vorticity distribution to investigate the secondary flow structures at the channel bend apex of M9 and M5. Specifically, two vortices can be observed: a clockwise vorticity near the bed and an anticlockwise vorticity near the water surface at M9 and vice versa at M5. The clockwise vorticity indicates the transfer of momentum from the outer to the inner bank, while the anticlockwise vorticity represents the first type of secondary flow that can be induced by turbulence anisotropy or transported from

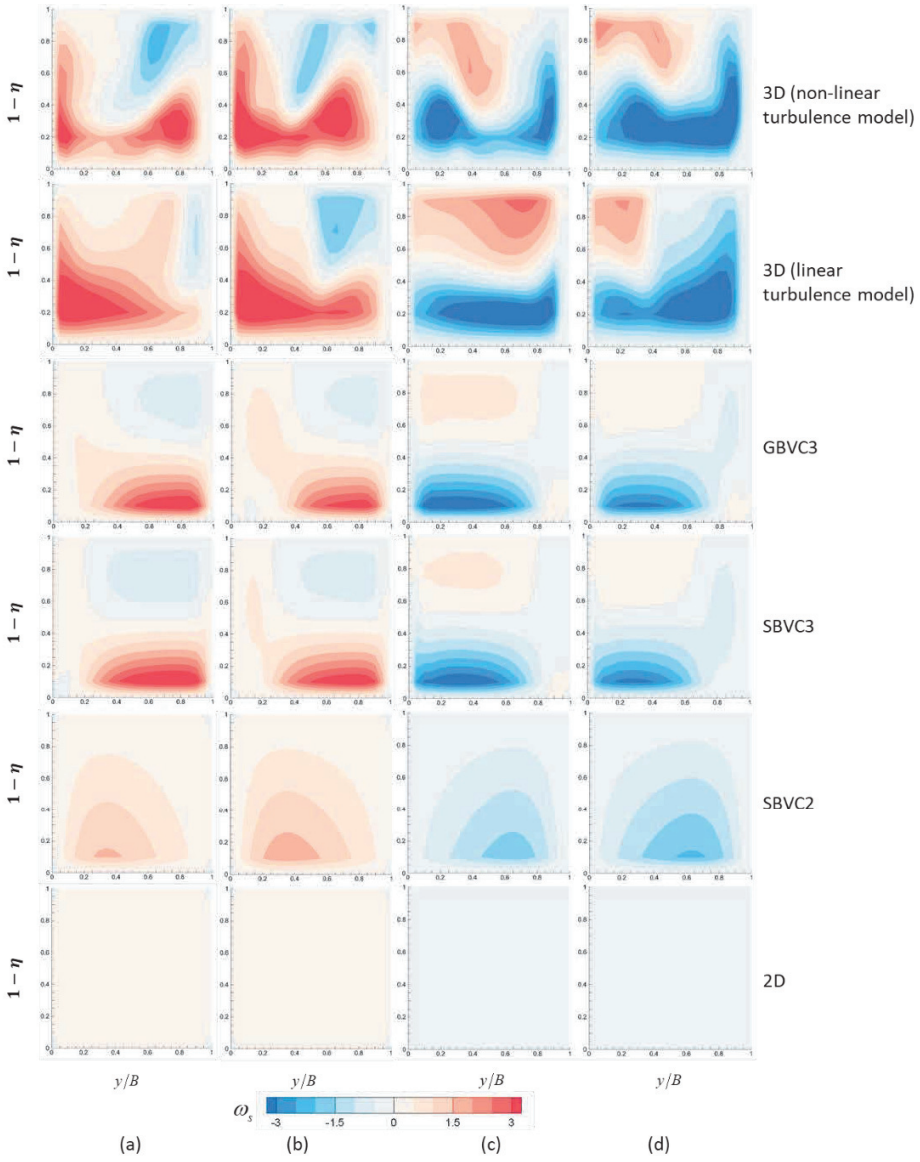

Figure 4.8 Streamwise vorticity distribution at; (a) smooth bed M9, (b) rough bed M9, (c) smooth bed M5, (d) rough bed M5. The horizontal axis and vertical axis represent the distance from the left bank proportionate to the channel width and from the bed proportionate to the water depth, respectively (i.e., 0 is the left bank and bed; 1 is the right bank and water surface).

the preceding channel bend (Abad & Garcia, 2009a; Kang & Sotiropoulos, 2011). In successive meander bends, the vorticity pattern from a prior bend persists and influences the pattern in the subsequent bend, indicating a mutual interaction of vorticity patterns between the preceding and following bends.

GBVC3 and SBVC3 have the capability to replicate two vortex components, although the strength is less than the 3D results. While SBVC2 does illustrate the transfer of momentum on the lower section of the channel through a clockwise vorticity, it falls short in capturing the anticlockwise vorticity near the surface, as it assumes an equilibrium condition for momentum transfer at the water surface. As anticipated, the 2D approach is unsuccessful in emulating vortex components, given its disregard for vertical velocity distribution.

4.5 Numerical investigation of channel meander effects on flow resistance

Once the model validation was confirmed to be in good agreement with the experimental results, the next step involved using the models to estimate the impact of channel sinuosity on flow resistance. To carry out the numerical experiment, the condition of $B/h = 3.6$ was used for the smooth and rough bed conditions. The sinuosity was then interpolated between these two conditions and extrapolated beyond sinuosity 1.25, with the total 13 sinuosity values were prepared for the interpolation and extrapolation, including 1.00, 1.05, 1.10, 1.15, 1.20, 1.25, 1.50, 1.75, 2.00, 2.25, 2.50, 2.75, and 3.00 (Figure 4.9).

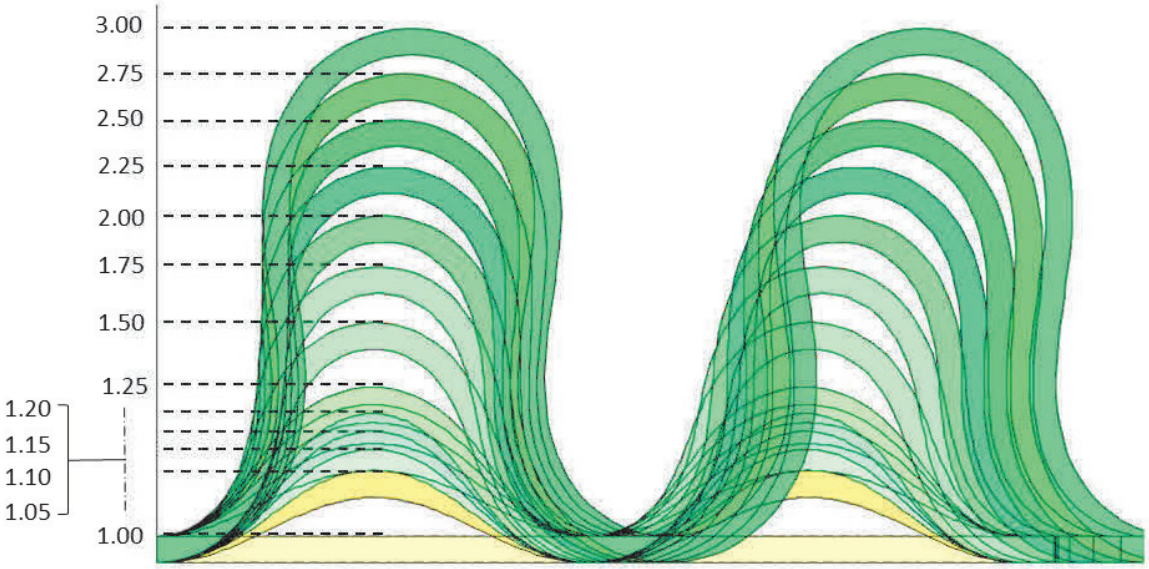

Figure 4.9 Channel shapes for investigation of sinuosity effect on flow resistance.

The models were equipped with a periodic boundary condition, which was designed to mitigate the impact of channel length on the aspect ratio while accounting for sinuosity changes. This implementation required the specification of the channel slope S = 0.0014 and initial water depth h = 0.108m as the initial conditions for the periodic boundary condition framework. Flow resistance was evaluated using the same method as the previous approach and presented as a ratio to the straight channel, i.e., $\Delta f = \left(f - f_0\right)/f_0$; f_0 : friction factor in straight channel. The results demonstrated that increased sinuosity led to greater flow resistance until a sinuosity value of 1.75, beyond which flow resistance decreased. This phenomenon can be explained by examining the curvature radius $\left(H/R\right)$ depicted in Figure 4.10(d). The $\left(H/R\right)$ can be associated with the strengthening of secondary flow (Blanckaert, 2009; Kashyap et al., 2012). The peak of flow resistance closely corresponded to the peak of $\left(H/R\right)$, with the flow resistance peak occurring at a

sinuosity of 1.75 $\left(\theta_{\max} = 78.76^{\circ}\right)$, and the $\left(H/R\right)$ peak occurring at a sinuosity of 1.5 $\left(\theta_{\max} = 69.5^{\circ}\right)$. The peak shift resulted by the models can be regarded to the maximum secondary flow intensity which is established downstream of the channel bend apex. There is a lag of secondary flow location resulted by the models. These findings align with the research conducted by Zhang et al. (2022), which observed that the flow resistance peak coincided with a maximum deflection angle $\left(\theta_{\max}\right)$ of 70° due to the intense secondary flow (Da Silva & Ebrahimi, 2017; Kashyap et al., 2012). Furthermore, a rough bed condition led to higher additional flow resistance compared to a smooth bed condition (Figure 4.10(a)).

Figure 4.10(b) and Figure 4.10(c) present the components in determining flow resistance for various sinuosities under smooth and rough bed conditions, respectively. It is evident that even the 2D model can capture the increase in flow resistance caused by the distortion effect arising from the distribution of depth-averaged velocity.

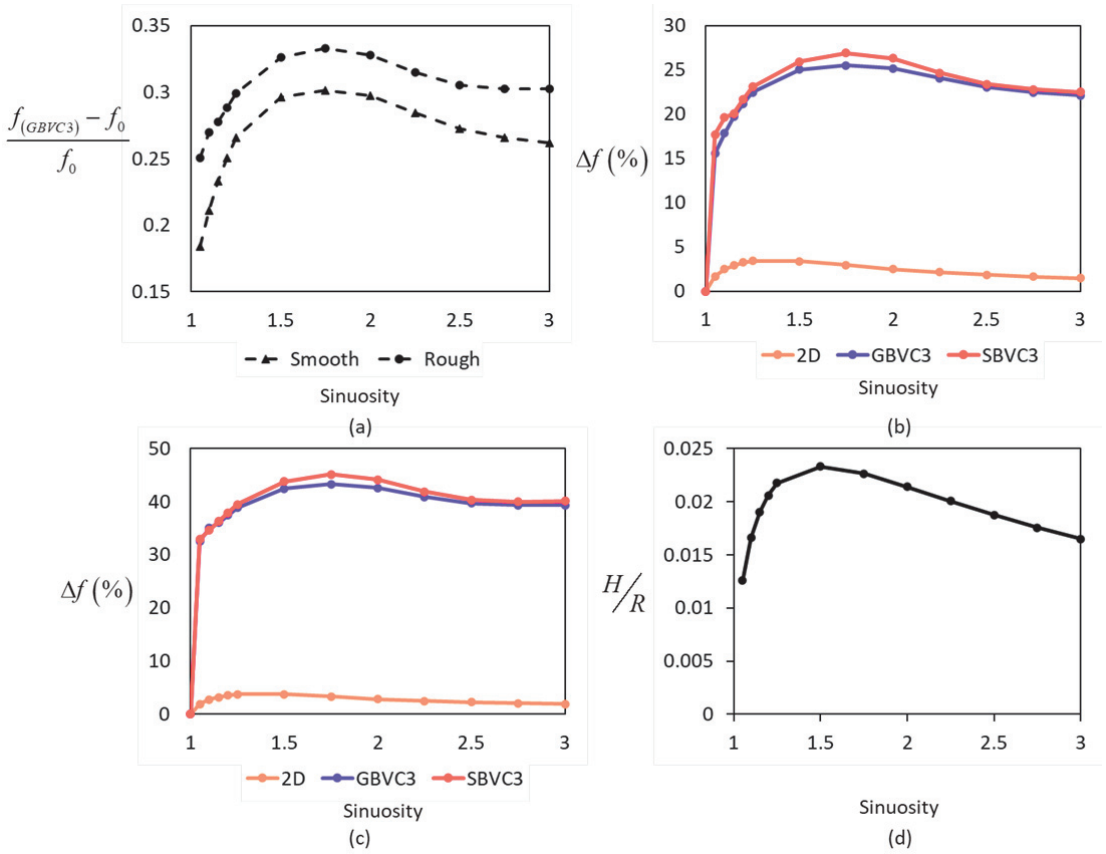

Figure 4.10 Numerical investigation of sinuosity effect on flow resistance; (a) Friction factor for various sinuosity in smooth and rough bed conditions; (b) and (c); Percentage friction factor comparison in smooth and rough bed conditions, respectively; (d) Curvature radius per width ratio variation along various sinuosity.

The results obtained from the GBVC3, SBVC3, and SBVC2 models indicate the influence of secondary flow strength on the increase in flow resistance. The disparity between GBVC3 and SBVC3 primarily arises in situations where the secondary flow intensity is high, attributed to the peak of (H/R). Beyond this point, both GBVC3 and SBVC3 exhibit a similar pattern of flow resistance due to the weakened secondary flow strength. In regions characterized by intense secondary flow, SBVC3 tends to overestimate the results obtained from GBVC3 due to the

assumption of the shallow water equation. While for SBVC2, it overestimated GBVC3 and SBVC3 due to lack of momentum equation at water surface consideration.

4.6 Conclusion

Previous research (Lugina et al., 2021) found that the shape of a channel can impact flow resistance, specifically by generating secondary flow due to bends in the channel. This paper confirms the importance of other factors, including aspect ratios, bed roughness, and sinuosity, on flow resistance. Flow resistance was evaluated by the friction factor of Darcy-Weisbach. The main results of the study are as follows:

Meandering channels display higher friction factors in comparison to straight channels, indicating a greater level of resistance in meandering channels. This rise in friction factor can be attributed to two factors: the presence of an additional transverse bed shear stress component and the advective momentum transport in the vertical direction resulting from secondary flow. These factors contribute to an increase in velocity near the bed and subsequently elevate bed shear stress.

There is an observed trend of decreasing friction factor as aspect ratios increase in smooth bed conditions. This can be attributed to the fact that smaller aspect ratios result in higher shear stress acting on the sidewall.

In the case of a rough bed condition, there is a tendency for the friction factor to increase as the aspect ratio increases. This can be explained by the rise in relative roughness height associated with the increasing aspect ratio. The intensification of bed roughness leads to higher levels of bed shear stress and turbulence, especially in shallow water depths with rough surfaces.

Generally, the BVC models were in good agreement to replicate both water surface elevation and flow resistance caused by secondary flow. Meanwhile, the 2D model cannot predict well the water surface elevation and flow resistance because of the inability to consider the increase in flow resistance due to secondary flow.

The numerical investigation demonstrated that as sinuosity increased, flow resistance also increased until reaching a sinuosity value of 1.75. However, beyond this point, flow resistance started to decrease. This phenomenon can be attributed to the strengthening of secondary flow, whereby a smaller $\left(H/R\right)$ value resulted in a more pronounced secondary flow.

Chapter 5 Numerical investigations of bed deformation in meandering channels

5.1 Introduction

The dynamic of meandering rivers has been attracted researchers to study its mechanisms. Classical works done by Schumm and Khan (1971) revealed that meandering rivers evolution progresses lateral (downstream) and transversal direction characterized by the formation of pools and point bars (Da Silva & Ebrahimi, 2017; da Silva & El-Tahawy, 2008; He et al., 2021; Termini, 2009b; Whiting & Dietrich, 1993b, 1993a). There have been various research attempts to understand the mechanism by which pools and point bars are located (da Silva & El-Tahawy, 2008; Whiting & Dietrich, 1993a) and its time development (Binns & da Silva, 2009, 2015). An understanding of pools and point bars mechanism will be beneficial for river engineering works.

There is a strong correlation between the formation of pools and point bars caused by secondary flow due to transverse convection of primary flow momentum, resulting in considerable deformation of the velocity distribution (Blanckaert & De Vriend, 2003, 2004, 2010; Blanckaert & Graf, 2001; Da Silva & Ebrahimi, 2017; De Vriend, 1979; Rozovskii, 1957). Secondary flows promote inward bed stress, resulting in transversal inward sediment transport, which triggers the riverbed on the outer bank deeper and induces point bar formation at the opposite side (Abad & Garcia, 2009a, 2009b; Blanckaert, 2010; Blanckaert & De Vriend, 2003, 2004, 2010; Ottevanger et al., 2012). Riverbed deformation redistributes flow structures, so called “topographic steering” (Blanckaert, 2010; Dietrich & Smith, 1983). As mentioned by Hodge (2017), sediment processes in rivers are linked through a series of feedbacks to both river morphology and flow dynamics.

The rapid development of computer hardware and software has led to an increase in the use of fully three-dimensional (3D) model for calculating flow and sediment transport interactions. The use of 3D models has proven to be a useful tool for better understanding the mechanisms involved in flow and sediment interactions (Constantinescu et al., 2011, 2013; Khosronejad et al., 2007; Lin & Falconer, 1996; Olsen, 2003; Rodriguez et al., 2004; Van Balen et al., 2010; Wu et al., 2000; Zeng, Constantinescu, Blanckaert, et al., 2008; Zeng, Constantinescu, & Weber, 2008). In spite of this, 3D models are still limited to small-scale and short-term configurations due to the high cost of computations (Lane, 1998; Qin et al., 2018).

Two-dimensional (2D) models have been used widely in hydraulic engineering practice for their ease of use, making them an appropriate option (Uchida et al., 2014). Duc et al. (2004) and Wu (2004) proposed a 2D depth-averaged model to predict bed deformations, but it had some limitations due to the absence of consideration of vertical structures in flow fields. The 2D depth-averaged model can be enhanced to consider vertical flow structures by adding equations of moment-of-momentum (Ghamry & Steffler, 2005; Jin & Steffler, 1993; Vasquez et al., 2006; Yeh & Kennedy, 1993), the so-called quasi-3D models.

In order to gain a better understanding of sediment transport mechanisms, Uchida & Fukuoka (2014) developed other quasi-3D models, known as bottom velocity calculation (BVC) method. The BVC method evaluates velocity on the bed coupled with depth-integrated continuity and horizontal momentum equations with additional equations of depth-integrated horizontal vorticity equations, momentum equations of the water surface, double integrated continuity equation over depth, and depth-integrated vertical momentum equation for non-hydrostatic pressure distribution. The models based on the BVC method were validated to calculate bed

deformation in simple compound meandering channel without sediment supply. Using a fourth-degree polynomial equation for the vertical distribution of velocity, Uchida et al. (2016) improved the models with the dynamic wall law and applied them to sediment transport with dam-break flows (Uchida & Fukuoka, 2019).

Application of quasi-3D models for sediment transport analysis is still limited into simple cases, in which curved open channel (Ghamry & Steffler, 2005; Jin & Steffler, 1993; Vasquez et al., 2006; Yeh & Kennedy, 1993) and without sediment supply condition (Uchida & Fukuoka, 2014). In spite of this, the consideration of more complex channel shapes and conditions is critical, e.g., sediment-flood disasters in Japan as a result of heavy precipitation in 2018 (Hashimoto et al., 2020; Uchida et al., 2021). Therefore, this research aims to investigate the applicability of quasi-3D models to predict bed deformation in meandering channel with excessive sediment supply.

5.2 Experimental setup

5.2.1 Curved channel

The experiment for curved channel case conducted by (Blanckaert, 2010) has a 193^o curved section with constant centerline radius of curvature R = 1.7 m, 9 m long straight inflow, and 5 m long straight outflow reaches. The width of the channel is 22.7 m along the centerline. The vertical sidewalls of the flume are hydraulically smooth. The mean water depth H is 0.141 m, the discharge Q is 0.089 m^3/s, and the width B = 1.3 m. The sand particles that are used have a diameter ranging from 1.6 – 2.2 mm with an average value of about 2.0 mm. Beginning from an initial flat bed, sediment was continuously supplied at the upstream at a rate of Q_s = 29.9 g/s. The experimental figure and setup for curved channel is shown in Figure 5.1 (a) and Table 5.1, respectively.

Table 5.1 Experiment conditions for curved and meandering channels

	Curved channel	Meandering-steep slope	Meandering-mild slope
Discharge (m^3/s)	0.089	0.0195	0.0124
Channel width (m)	1.3	0.39	0.39
Sediment diameter (mm)	2.00	1.55	1.55
Slope	0.003	0.203	0.007
θ_{max}	193°	52°	52°
Q_s (g/s)	29.9	141	20.2

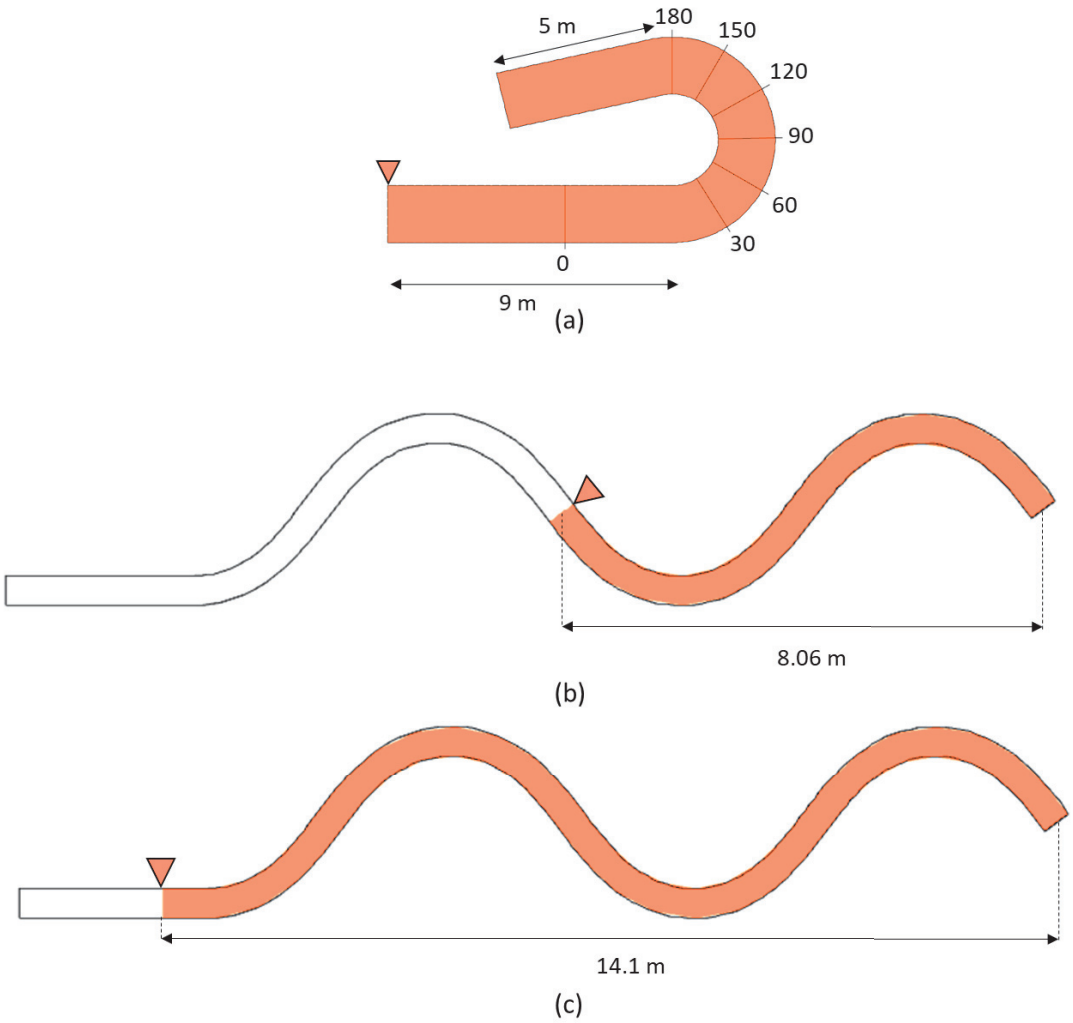

Figure 5.1 Experimental channel; (a) Curved channel; (b) Meandering-steep slope; (c) Meandering-mild slope.

5.2.2 Meandering channel

The laboratory experiments for meandering channel as shown in Figure 5.1(b) and Figure 5.1(c) were conducted at the Hydraulic Experimental Facility of Hiroshima University with two slope conditions: steep and mild slope. The total length of these channels is 16 m in the straight

direction, with a width B of 0.39 m. The meandering channel featured a maximum deflection angle of 52.99°, a meandering length of 8.06 m in a wavelength of 6.43 m, and a sinuosity of 1.25. Weirs were installed at the downstream of the channel with 0.1 m and 0.15 m height for steep and mild slope, respectively. The sand particles used have an average diameter of 1.55 mm. For the case of steep slope, an initial flat bed was set, and sediment supply rate was Q_s = 141 g/s. For the case of mild slope, an initial slope was set to be 1/500, and sediment supply rate was Q_s = 20.2 g/s. The experimental figure and setup for curved channel is shown in Figure 5.1(b) and Figure 5.1(c) and Table 5.1, respectively.

5.3 Numerical Model

In this study, several types of depth integrated calculation models based on the BVC method indicated in Table 2.1 were compared to clarify its applicability on predicting bed morphology profile by incorporating sediment supply effect. The calculation domain included the entire experimental channel with a computational mesh $dx = 0.125$ m, $dy = 0.05$ m for the curved channel, and $dx = 0.1$ m, $dy = 0.02$ m for the meandering channel. The experimental discharge provides the upstream boundary condition, the sediment supply rates were converted to be a bed load rate at the location of supplied sediment, and the weir heights were used as the downstream condition. Additionally, a Nays2DH model was employed to be a benchmark for BVC models.

5.4 Prediction of bed morphology in meandering channels

Figure 5.2 shows a comparison of bed and water levels in cross-sectional average for curved and meandering channels. It can be noticed that the trend of bed and water levels from experimental

dataset can be reproduced by BVC models and Nasy2DH model, although the scouring magnitude cannot be represented by the model, their location show a good agreement with experimental dataset.

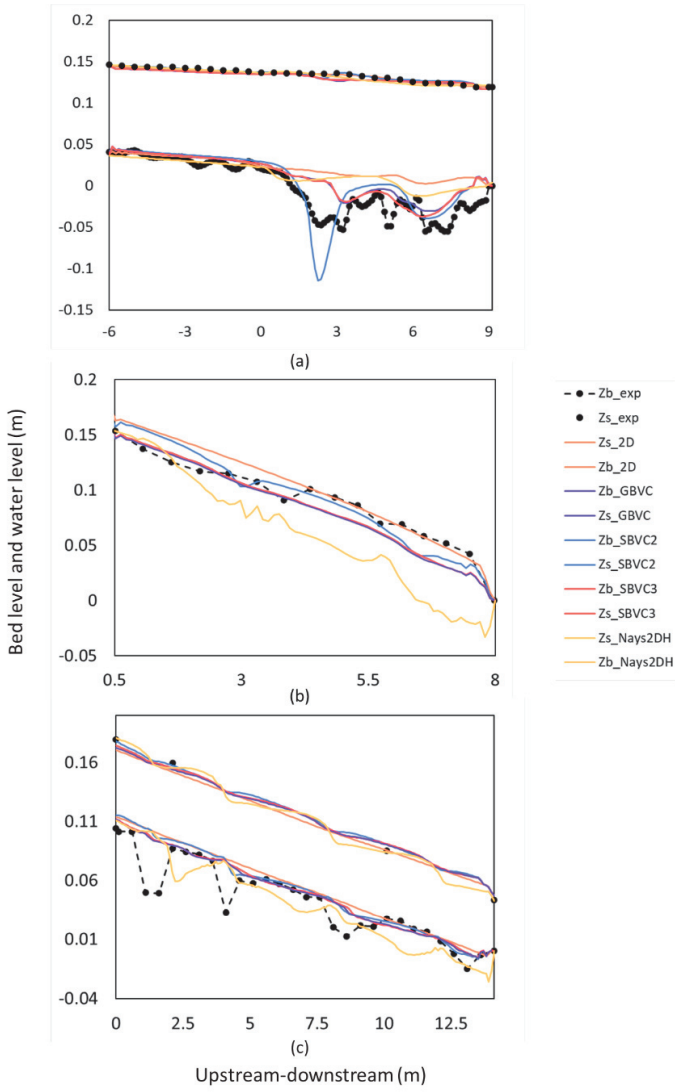

Figure 5.2 Bed and water levels comparison between experimental dataset and numerical mode results in forms of cross-sectional averaged in: (a) curved channel; (b) steep-meandering channel; (c) mild-meandering channel.

Figure 5.3, Figure 5.4, and Figure 5.5 show a comparison of bed level between experimental dataset and numerical model results in curved channel, steep-meandering channel, and mild-meandering channel, respectively. In curved channel (Figure 5.3), there is a noticeable scouring and deposition pattern particularly located at the bend entrance until 90^{o}, this phenomenon was attributed to the existence of outward mass transport that makes maximum streamwise unit discharge shifts outward and horizontal flow circulation appeared at the point bar location (Blanckaert, 2010). The scouring located near the bend exit was attributed to the flow acceleration in the outer bank induced by the disappearance of water surface superelevation (Blanckaert, 2010; Zeng, Constantinescu, Blanckaert, et al., 2008). In the case of meandering channel, the location of scouring and deposition is found at the bend apex where a secondary flow structure reaches its peak.

The advantage of BVC models were confirmed in reproducing the slope and location of scouring and deposition. GBVC and SBVC3 model show similar results indicating that non-hydrostatic considerations do not have a significant effect on reproducing scouring and deposition. The absence of horizontal momentum equation in SBVC2 leads to the large results of scouring and deposition. While for 2D, the flow tends to follow the channel shape due to the lack of considering vertical velocity distribution thus causing its inability to represent scouring and deposition. Nays2DH model shows an underestimation of the result, it might be caused by the incorrect boundary conditions setting.

Figure 5.6 shows a cross-sectional comparison of bed level between experimental dataset and model results in curved and meandering channels. The magnitude of bed level for each model can be observed more clearly. Although the BVC models result failed to reproduce the scouring,

the results shown at the downstream of the channels are better compared to the upstream ones. These phenomena can be attributed to the strength of secondary flow where the upstream secondary flow is larger than the downstream. The result shown by 2D model indicated that the model failed in all cross-sections in reproducing bed level. Nays2DH model is able to reproduce the location of scouring and deposition, however the magnitude is still underestimated.

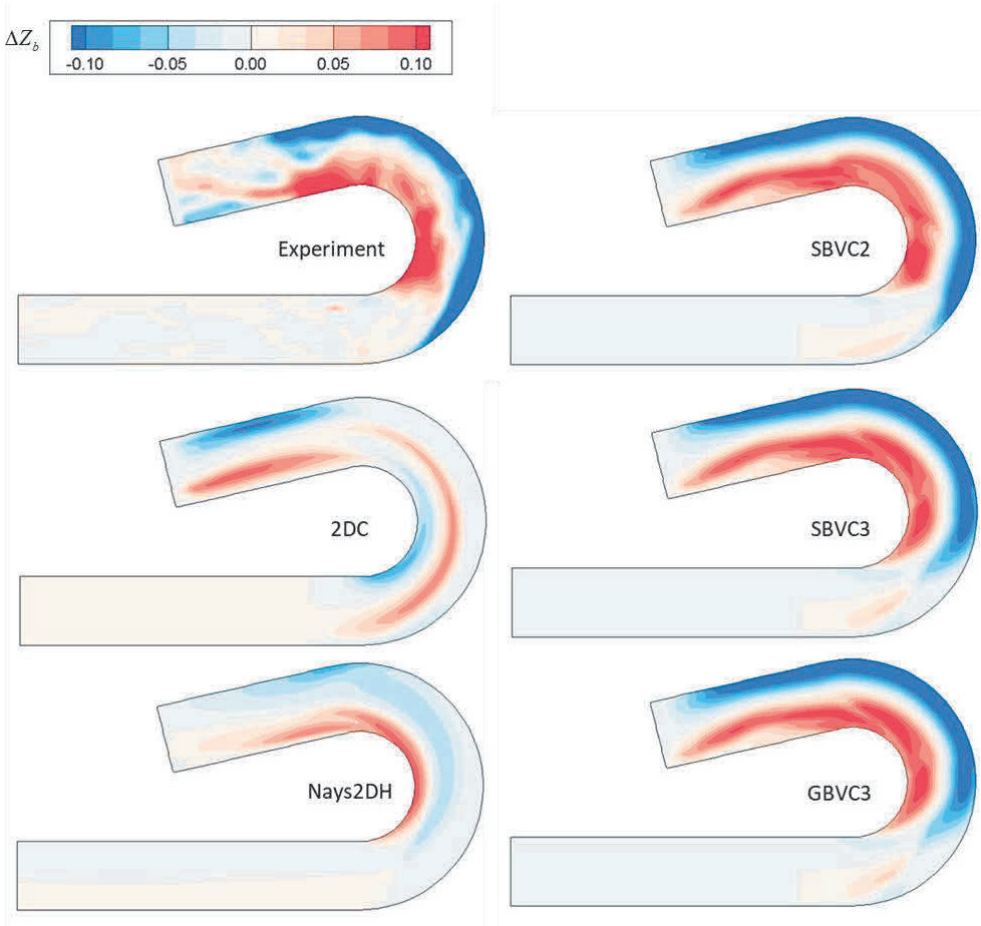

Figure 5.3 Bed level comparison in curved channel.

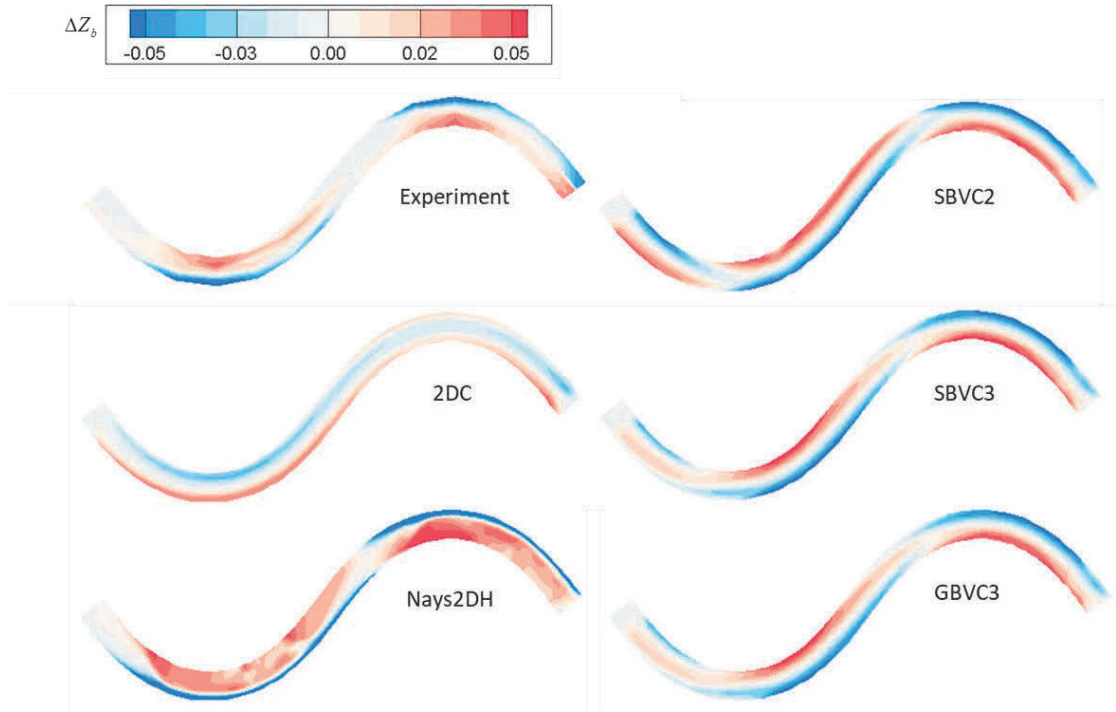

Figure 5.4 Bed level comparison in steep-meandering channel.

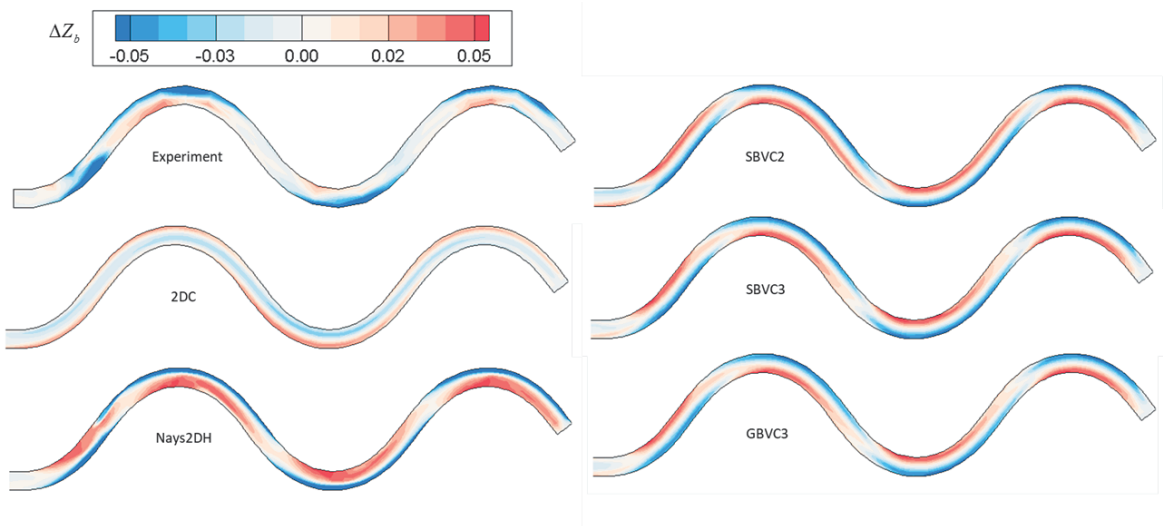

Figure 5.5 Bed level comparison in mild-meandering channel.

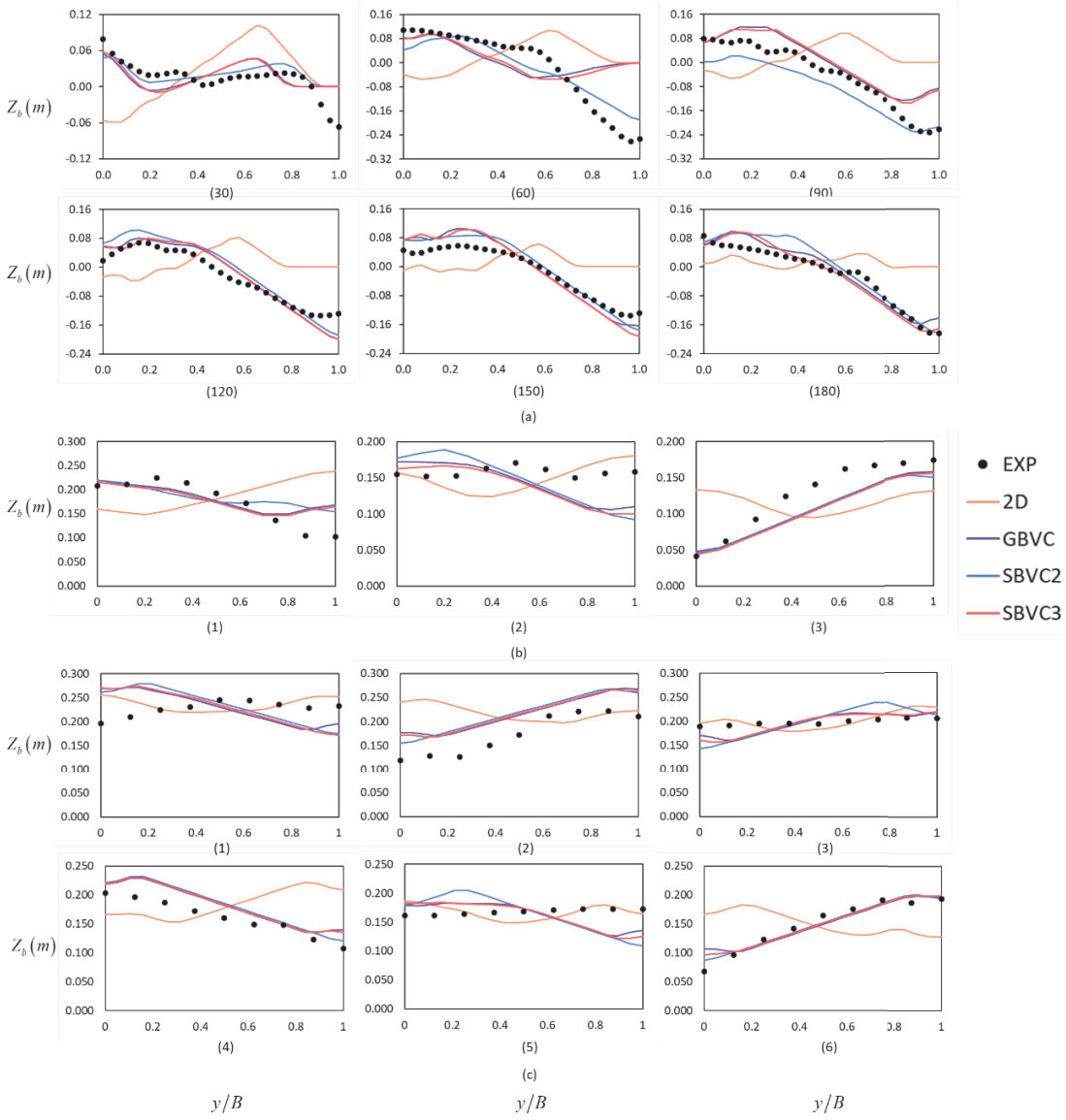

Figure 5.6 Cross-sectional comparison of bed level in (a) curved channel, (b) steep-meandering channel, (c) mild-meandering channel. The horizontal axis shows distance from left (0) to right (1) banks.

5.5 Conclusion

This paper investigates the applicability of BVC models in reproducing bed topography in curved and meandering channels by considering sediment supply at the upstream end. The BVC models' results are in good agreement with experiment dataset in terms of predicting the location of scouring and deposition, however they failed to represent the magnitude of scouring and deposition. GBVC and SBVC3 model show similar results indicating that non-hydrostatic considerations do not have a significant effect on reproducing scouring and deposition. The absence of horizontal momentum equation in SBVC2 leads to the large results of scouring and deposition. While for 2D, the flow tends to follow the channel shape due to the lack of considering vertical velocity distribution thus causing its inability to represent scouring and deposition.

Chapter 6 Conclusion and future research

6.1 Conclusion

This research aims to investigate flow resistance and sediment transport dynamics in meandering rivers and to develop a numerical model with both efficient calculation time and high accuracy. First, we investigated flow dynamics in curved channels and developed a numerical discretization method to overcome nonphysical phenomena resulted from shallow water assumptions. Second, we conducted laboratory and numerical experiments to study the effect of channel shape, bed characteristic, aspect ratio, and sinuosity on flow resistance and applied the proposed method to evaluate those channel resistance. Finally, we included sediment transport model to predict bed deformation in curved and meandering channels.

The specific conclusions and contributions of this study can be summarized as follows:

- The proposed dispersion method can avoid excessively high velocities along the wall that is a drawback that has been overlooked in advanced depth-integrated models. By incorporating the dispersion term, it is demonstrated that the BVC method can reproduce the experimental water levels and velocity profiles in the channel bend, including those along the outer bank, with the same accuracy as that of the full three-dimensional model.
- Meandering channels display higher friction factors in comparison to straight channels, indicating a greater level of resistance in meandering channels. This rise in friction factor can be attributed to two factors: the presence of an additional transverse bed shear stress component and the advective momentum transport in the vertical direction resulting from

secondary flow. These factors contribute to an increase in velocity near the bed and subsequently elevate bed shear stress.

- There is an observed trend of decreasing friction factor as aspect ratios increase in smooth bed conditions. This can be attributed to the fact that smaller aspect ratios result in higher shear stress acting on the sidewall.
- In the case of a rough bed condition, there is a tendency for the friction factor to increase as the aspect ratio increases. This can be explained by the rise in relative roughness height associated with the increasing aspect ratio. The intensification of bed roughness leads to higher levels of bed shear stress and turbulence, especially in shallow water depths with rough surfaces.
- Generally, the BVC models were in good agreement to replicate both water surface elevation and flow resistance caused by secondary flow. Meanwhile, the 2D model cannot predict well the water surface elevation and flow resistance because of the inability to consider the increase in flow resistance due to secondary flow.
- The numerical investigation demonstrated that as sinuosity increased, flow resistance also increased until reaching a sinuosity value of 1.75. However, beyond this point, flow resistance started to decrease. This phenomenon can be attributed to the strengthening of secondary flow, whereby a smaller value resulted in a more pronounced secondary flow.

The BVC models' results are in good agreement with experiment dataset in terms of predicting the location of scouring and deposition, however they failed to represent the magnitude of scouring and deposition.

6.2 Future research

Based on the findings, the following can be recommended:

- All the cases in this study were conducted in laboratory channel experiments, to investigate the applicability of BVC models it will be necessary to apply the model to real river cases.
- The investigation of flow resistance in this study can have significant contributions into its mechanism understanding, however further research is needed to obtain more comprehensive knowledge like study on the effects of vegetation and sediment dynamics in flow resistance.

References

Abad, J. D., & Garcia, M. H. (2009a). Experiments in a high-amplitude Kinoshita meandering channel: 1. Implications of bend orientation on mean and turbulent flow structure. *Water Resources Research*, *45*(2), 1–19. https://doi.org/10.1029/2008WR007016

Abad, J. D., & Garcia, M. H. (2009b). Experiments in a high-amplitude Kinoshita meandering channel: 2. Implications of bend orientation on bed morphodynamics. *Water Resources Research*, *45*(2), 1–14. https://doi.org/10.1029/2008wr007017

Amoros, C. (2001). The Concept of Habitat Diversity Between and Within Ecosystems Applied to River Side-Arm Restoration. *Environmental Management*, *28*(6), 805–817. https://doi.org/10.1007/s002670010263

Ashida, K., & Michiue, M. (1972). STUDY ON HYDRAULIC RESISTANCE AND BED-LOAD TRANSPORT RATE IN ALLUVIAL STREAMS. *Proceedings of the Japan Society of Civil Engineers*, *1972*(206), 59–69. https://doi.org/10.2208/jscej1969.1972.206_59

Begnudelli, L., Valiani, A., & Sanders, B. F. (2010). A balanced treatment of secondary currents, turbulence and dispersion in a depth-integrated hydrodynamic and bed deformation model for channel bends. *Advances in Water Resources*, *33*(1), 17–33. https://doi.org/10.1016/j.advwatres.2009.10.004

Binns, A. D., & da Silva, A. M. (2009). On the Quantification of the Bed Development Time of Alluvial Meandering Streams. *Journal of Hydraulic Engineering*, *135*(5), 350–360. https://doi.org/10.1061/(asce)hy.1943-7900.0000025

Binns, A. D., & da Silva, A. M. F. (2015). Meandering bed development time: Formulation and related experimental testing. *Advances in Water Resources*, *81*, 152–160. https://doi.org/10.1016/j.advwatres.2014.11.007

Blanckaert, K. (2009). Saturation of curvature-induced secondary flow, energy losses, and turbulence in sharp open-channel bends: Laboratory experiments, analysis, and modeling. *Journal of Geophysical Research*, *114*(F3), F03015. https://doi.org/10.1029/2008JF001137

Blanckaert, K. (2010). Topographic steering, flow recirculation, velocity redistribution, and bed topography in sharp meander bends. *Water Resources Research*, *46*(9). https://doi.org/10.1029/2009WR008303

Blanckaert, K., & De Vriend, H. J. (2003). Nonlinear modeling of mean flow redistribution in curved open channels. *Water Resources Research*, *39*(12), 1–14. https://doi.org/10.1029/2003WR002068

Blanckaert, K., & De Vriend, H. J. (2004). Secondary flow in sharp open-channel bends. *Journal of Fluid Mechanics*, *498*, 353–380. https://doi.org/10.1017/S0022112003006979

Blanckaert, K., & de Vriend, H. J. (2005). Turbulence characteristics in sharp open-channel bends. *Physics of Fluids*, *17*(5), 1–15. https://doi.org/10.1063/1.1886726

Blanckaert, K., & De Vriend, H. J. (2010). Meander dynamics: A nonlinear model without curvature restrictions for flow in open-channel bends. *Journal of Geophysical Research*, *115*(F4), F04011. https://doi.org/10.1029/2009JF001301

Blanckaert, K., & Graf, W. H. (2001). Mean Flow and Turbulence in Open-Channel Bend. *Journal of Hydraulic Engineering*, *127*(10), 835–847. https://doi.org/10.1061/(ASCE)0733-9429(2001)127:10(835)

Blanckaert, K., & Graf, W. H. (2004). Momentum transport in sharp open-channel bends. *Journal of Hydraulic Engineering*, *130*(3), 186–198. https://doi.org/10.1061/(asce)0733-9429(2004)130:3(186)

Bora, K., & Kalita, M. (2020). A Semi-Coupled Model for Morphological Flow Simulation in River Bend. *Journal of Applied Fluid Mechanics*, *13*(05). https://doi.org/10.36884/jafm.13.05.30842

Chanson, H. (2004). *The hydraulics of open channel flow: An introduction basic principles, sediment motion, hydraulic modelling, design of hydraulic structures* (2nd ed). Elsevier.

Chaudhry, M. H. (2007). *Open-channel flow* (2nd ed). Springer.

Chow, V. T. (2009). *Open-channel hydraulics*. Blackburn Press.

Constantinescu, G., Kashyap, S., Tokyay, T., Rennie, C. D., & Townsend, R. D. (2013). Hydrodynamic processes and sediment erosion mechanisms in an open channel bend of strong curvature with deformed bathymetry. *Journal of Geophysical Research*, *118*(2), 480–496. https://doi.org/10.1002/jgrf.20042

Constantinescu, G., Koken, M., & Zeng, J. (2011). The structure of turbulent flow in an open channel bend of strong curvature with deformed bed: Insight provided by detached eddy simulation. *Water Resources Research*, *47*(5), 1–17. https://doi.org/10.1029/2010WR010114

Da Silva, A. M. F., & Ebrahimi, M. (2017). Meandering Morphodynamics: Insights from Laboratory and Numerical Experiments and Beyond. *Journal of Hydraulic Engineering*, *143*(9), 03117005. https://doi.org/10.1061/(ASCE)HY.1943-7900.0001324

da Silva, A. M. F., & El-Tahawy, T. (2008). On the location in flow plan of erosion-deposition zones in sine-generated meandering streams. *Journal of Hydraulic Research*, *46*(1), 49–60. https://doi.org/10.1080/00221686.2008.9521939

De Vriend, H. J. (1979). *Flow measurements in a curved rectangular channel* (Institutional Repository 9–79). TU Delft, Department of Hydraulic Engineering. http://resolver.tudelft.nl/uuid:7a35d722-1373-447d-af50-f3aed341c02b

Dietrich, W. E., & Smith, J. D. (1983). Influence of the point bar on flow through curved channels. *Water Resources Research*, *19*(5), 1173–1192.

Dietrich, W. E., Smith, J. D., & Dunne, T. (1979). Flow and Sediment Transport in a Sand Bedded Meander. *The Journal of Geology*, *87*(3), 305–315.

D'Ippolito, A., Calomino, F., Alfonsi, G., & Lauria, A. (2021). Flow Resistance in Open Channel Due to Vegetation at Reach Scale: A Review. *Water*, *13*(2), 116. https://doi.org/10.3390/w13020116

Doocy, S., Daniels, A., Murray, S., & Kirsch, T. D. (2013). The Human Impact of Floods: A Historical Review of Events 1980-2009 and Systematic Literature Review. *PLoS Currents*. https://doi.org/10.1371/currents.dis.f4deb457904936b07c09daa98ee8171a

Duan, J. G. (2004). Simulation of Flow and Mass Dispersion in Meandering Channels. *Journal of Hydraulic Engineering*, *130*(10), 964–976. https://doi.org/10.1061/(ASCE)0733-9429(2004)130:10(964)

Duc, B. M., Wenka, T., & Rodi, W. (2004). Numerical Modeling of Bed Deformation in Laboratory Channels. *Journal of Hydraulic Engineering*, *130*(9), 894–904. https://doi.org/10.1061/(ASCE)0733-9429(2004)130:9(894)

Engel, F. L., & Rhoads, B. L. (2017). Velocity profiles and the structure of turbulence at the outer bank of a compound meander bend. *Geomorphology*, *295*, 191–201. https://doi.org/10.1016/j.geomorph.2017.06.018

Falcon, M. (1984). Secondary Flow in Curved Open Channels. *Annual Review of Fluid Mechanics*, *16*(1), 179–193. https://doi.org/10.1146/annurev.fl.16.010184.001143

Ferguson, R. I. (2010). Time to abandon the Manning equation? *Earth Surface Processes and Landforms*, *35*(15), 1873–1876. https://doi.org/10.1002/esp.2091

Finnie, J., Donnell, B., Letter, J., & Bernard, R. S. (1999). Secondary Flow Correction for Depth-Averaged Flow Calculations. *Journal of Engineering Mechanics*, *125*(7), 848–863. https://doi.org/10.1061/(ASCE)0733-9399(1999)125:7(848)

Garssen, A. G., Baattrup-Pedersen, A., Riis, T., Raven, B. M., Hoffman, C. C., Verhoeven, J. T. A., & Soons, M. B. (2017). Effects of increased flooding on riparian vegetation: Field experiments

simulating climate change along five European lowland streams. *Global Change Biology*, *23*(8), 3052–3063. https://doi.org/10.1111/gcb.13687

Ghaderi, A., Abbasi, S., & Di Francesco, S. (2021). Numerical Study on the Hydraulic Properties of Flow over Different Pooled Stepped Spillways. *Water*, *13*(5), 710. https://doi.org/10.3390/w13050710

Ghamry, H. K., & Steffler, P. M. (2005). Two-dimensional depth-averaged modeling of flow in curved open channels. *Journal of Hydraulic Research*, *43*(1), 44–55. https://doi.org/10.1080/00221680509500110

Gladkov, G., Habel, M., Babiński, Z., & Belyakov, P. (2021). Sediment Transport and Water Flow Resistance in Alluvial River Channels: Modified Model of Transport of Non-Uniform Grain-Size Sediments. *Water*, *13*(15), 2038. https://doi.org/10.3390/w13152038

Graziano, M. P., Deguire, A. K., & Surasinghe, T. D. (2022). Riparian Buffers as a Critical Landscape Feature: Insights for Riverscape Conservation and Policy Renovations. *Diversity*, *14*(3), 172. https://doi.org/10.3390/d14030172

Hashimoto, R., Tsuchida, T., Moriwaki, T., & Kano, S. (2020). Hiroshima Prefecture geo-disasters due to Western Japan Torrential rainfall in July 2018. *Soils and Foundations*, *60*(1), 283–299. https://doi.org/10.1016/j.sandf.2019.11.010

He, L., Chen, D., Termini, D., Zhang, S., & Zhu, Z. (2021). Experiments on longitudinal and transverse bedload transport in sine-generated meandering channels. *Applied Sciences*, *11*(6560). https://doi.org/10.3390/app11146560

Henderson, F. M. (1966). *Open channel flow*. MacMillan Publishing Co., Inc.

Hermeline, F. (2000). A Finite Volume Method for the Approximation of Diffusion Operators on Distorted Meshes. *Journal of Computational Physics*, *160*(2), 481–499. https://doi.org/10.1006/jcph.2000.6466

Hodge, R. A. (2017). Sediment processes in bedrock-alluvial rivers: Research since 2010 and modelling the impact of fluctuating sediment supply on sediment cover. In *Gravel-Bed Rivers: Process and Disasters* (pp. 639–669). Wiley.

Jia, Y., & Wang, S. S. Y. (1999). Numerical Model for Channel Flow and Morphological Change Studies. *Journal of Hydraulic Engineering*, *125*(9), 924–933. https://doi.org/10.1061/(ASCE)0733-9429(1999)125:9(924)

Jin, Y., & Steffler, P. M. (1993). Predicting Flow in Curved Open Channels by Depth-Averaged Method. *Journal of Hydraulic Engineering*, *119*(1), 109–124. https://doi.org/10.1061/(ASCE)0733-9429(1993)119:1(109)

Jing, S., Yang, W., & Chen, Y. (2019). Smooth Open Channel with Increasing Aspect Ratio: Influence on Secondary Flow. *Water*, *11*(9), 1872. https://doi.org/10.3390/w11091872

Jonkman, S. N. (2005). Global Perspectives on Loss of Human Life Caused by Floods. *Natural Hazards*, *34*(2), 151–175. https://doi.org/10.1007/s11069-004-8891-3

Kang, S., & Sotiropoulos, F. (2011). Flow phenomena and mechanisms in a field-scale experimental meandering channel with a pool-riffle sequence: Insights gained via numerical simulation. *Journal of Geophysical Research*, *116*(F3), F03011. https://doi.org/10.1029/2010JF001814

Kashyap, S., Constantinescu, G., Rennie, C. D., Post, G., & Townsend, R. (2012). Influence of Channel Aspect Ratio and Curvature on Flow, Secondary Circulation, and Bed Shear Stress in a Rectangular Channel Bend. *Journal of Hydraulic Engineering*, *138*(12), 1045–1059. https://doi.org/10.1061/(ASCE)HY.1943-7900.0000643

Khatua, K. K., Patra, K. C., Nayak, P., & Sahoo, N. (2012). Stage–discharge prediction for meandering channels. *International Journal of Computational Methods and Experimental Measurements*, *1*(1), 80–92. https://doi.org/10.2495/CMEM-V1-N1-80-92

Khosronejad, A., Rennie, C. D., Neyshabouri, S. A. A., & Townsend, R. D. (2007). 3D numerical modeling of flow and sediment transport in laboratory channel bends. *Journal of Hydraulic Engineering*, *133*(10), 1123–1134. https://doi.org/10.32508/stdjsee.v3i1.508

Kimura, I. (2020). *iRIC NaysCUBE* (Ver.3.1) [Computer software]. https://i-ric.org/en/solvers/nayscube/

Kimura, I., Uijttewaal, W. S., Hosoda, T., & Ali, Md. S. (2009). URANS Computations of Shallow Grid Turbulence. *Journal of Hydraulic Engineering*, *135*(2), 118–131. https://doi.org/10.1061/(ASCE)0733-9429(2009)135:2(118)

Kobayashi, S., Kantoush, S. A., Al-mamari, M. M., Tazumi, M., Takemon, Y., & Sumi, T. (2022). Local flow convergence, bed scour, and aquatic habitat formation during floods around wooden training structures placed on sand-gravel bars. *Science of The Total Environment*, *817*, 152992. https://doi.org/10.1016/j.scitotenv.2022.152992

Lane, S. N. (1998). Hydraulic modelling in hydrology and geomoprhology: A review of high resolution approaches. *Hydrological Processes*, *12*(8), 1131–1150. https://doi.org/10.1002/(SICI)1099-1085(19980630)12:8<1131::AID-HYP611>3.0.CO;2-K

Langendoen, E. J. (2001). *Evaluation of the effectiveness of selected computer models of depth-average free surface flow and sediment transport to predict the effects of hydraulic structures on river morphology* [Rep., prepared for WES Vicksburg]. National Sedimentation Laboratory, Agricultural Research Service, U.S. Department of Agriculture.

Latosinski, F. G., Amsler, M. L., Vionnet, C. A., Heredia Ligorria, A. I., Szupiany, R. N., Diaz Lozada, J. M., García, C. M., & García, M. H. (2022). The role of dunes in flow resistance in a large and a small river. The case of the Paraná and Tercero rivers, Argentina. *Journal of Hydraulic Research*, *60*(3), 389–407. https://doi.org/10.1080/00221686.2021.2001588

Lave, R., Doyle, M., & Robertson, M. (2010). Privatizing stream restoration in the US. *Social Studies of Science*, *40*(5), 677–703. https://doi.org/10.1177/0306312710379671

Lazzarin, T., & Viero, D. P. (2023). Curvature-induced secondary flow in 2D depth-averaged hydro-morphodynamic models: An assessment of different approaches and key factors. *Advances in Water Resources*, *171*, 104355. https://doi.org/10.1016/j.advwatres.2022.104355

Leopold, L. B., Bagnold, R. A., Wolman, M. G., & Brush Jr., L. M. (1960). *Flow resistance in sinuous or irregular channels* (Professional Paper) [Professional Paper]. U.S. Government Printing Office.

Lin, B., & Falconer, R. A. (1996). Numerical modelling of three-dimensional suspended sediment for estuarine and coastal waters. *Journal of Hydraulic Research*, *34*(4), 435–456. https://doi.org/10.1080/00221689609498470

Lugina, F. P., Uchida, T., & Hatono, M. (2021). Effect of channel meander on flow resistance. *Journal of Japan Society of Civil Engineers, Ser. B1 (Hydraulic Engineering)*, *77*(No. 2), I_865-I_870.

Lugina, F. P., Uchida, T., & Kawahara, Y. (2020). Study on numerical simulation of flow structures in a curved open channel. *Proceedings of the 22nd IAHR-APD Congress*.

Lugina, F. P., Uchida, T., & Kawahara, Y. (2022). Study on numerical calculation of flow structures in a curved open channel with advanced depth-integrated models. *IOP Conference Series: Earth and Environmental Science*, *1065*(1), 012004. https://doi.org/10.1088/1755-1315/1065/1/012004

Manzini, G., & Russo, A. (2008). A finite volume method for advection–diffusion problems in convection-dominated regimes. *Computer Methods in Applied Mechanics and Engineering*, *197*(13–16), 1242–1261. https://doi.org/10.1016/j.cma.2007.11.014

Motta, D., Abad, J. D., Langendoen, E. J., & Garcia, M. H. (2012). A simplified 2D model for meander migration with physically-based bank evolution. *Geomorphology*, *163–164*, 10–25. https://doi.org/10.1016/j.geomorph.2011.06.036

Naiman, R. J., Decamps, H., & Pollock, M. (1993). The Role of Riparian Corridors in Maintaining Regional Biodiversity. *Ecological Applications*, *3*(2), 209–212. https://doi.org/10.2307/1941822

Nanson, G. C. (1980). Point bar and floodplain formation of the meandering Beatton River, northeastern British Columbia, Canada. *Sedimentology*, *27*(1), 3–29. https://doi.org/10.1111/j.1365-3091.1980.tb01155.x

Nelson, J. M., Shimizu, Y., Abe, T., Asahi, K., Gamou, M., Inoue, T., Iwasaki, T., Kakinuma, T., Kawamura, S., Kimura, I., Kyuka, T., McDonald, R. R., Nabi, M., Nakatsugawa, M., Simões, F. R., Takebayashi, H., & Watanabe, Y. (2016). The international river interface cooperative: Public domain flow and morphodynamics software for education and applications. *Advances in Water Resources*, *93*, 62–74. https://doi.org/10.1016/j.advwatres.2015.09.017

Nezhad, H. M., Mohammadi, M., Ghaderi, A., Bagherzadeh, M., Ricardo, A. M., & Kuriqi, A. (2022). Flow resistance and velocity distribution in a smooth triangular channel. *Water Supply*, *22*(5), 5253–5264. https://doi.org/10.2166/ws.2022.142

Nezu, I., & Nakagawa, H. (1993). *Turbulence in open-channel flows*. CRC Press.

Nicholas, A. P. (2001). Computational fluid dynamics modelling of boundary roughness in gravel-bed rivers: An investigation of the effects of random variability in bed elevation. *Earth Surface Processes and Landforms*, *26*(4), 345–362. https://doi.org/10.1002/esp.178

Nikora, V., & Roy, A. G. (2012). Secondary Flows in Rivers: Theoretical Framework, Recent Advances, and Current Challenges. In M. Church, P. M. Biron, & A. G. Roy (Eds.), *Gravel-Bed Rivers* (1st ed., pp. 1–22). Wiley. https://doi.org/10.1002/9781119952497.ch1

Nistoran, D. G., Ionescu, C., Pătru, G., Armaş, I., & Omrani, Ş. G. (2017). One Dimensional Sediment Transport Model to Assess Channel Changes along Olteniţa-Călăraşi Reach of Danube River, Romania. *Energy Procedia*, *112*, 67–74. https://doi.org/10.1016/j.egypro.2017.03.1062

Olsen, N. R. B. (2003). Three-Dimensional CFD Modeling of Self-Forming Meandering Channel. *Journal of Hydraulic Engineering*, *129*(5), 366–372. https://doi.org/10.1061/(asce)0733-9429(2003)129:5(366)

Ottevanger, W., Blanckaert, K., & Uijttewaal, W. S. J. (2012). Processes governing the flow redistribution in sharp river bends. *Geomorphology*, *163–164*, 45–55. https://doi.org/10.1016/j.geomorph.2011.04.049

Palmer, M. A., Bernhardt, E. S., Allan, J. D., Lake, P. S., Alexander, G., Brooks, S., Carr, J., Clayton, S., Dahm, C. N., Follstad Shah, J., Galat, D. L., Loss, S. G., Goodwin, P., Hart, D. D., Hassett, B., Jenkinson, R., Kondolf, G. M., Lave, R., Meyer, J. L., … Sudduth, E. (2005). Standards for ecologically successful river restoration: Ecological success in river restoration. *Journal of Applied Ecology*, *42*(2), 208–217. https://doi.org/10.1111/j.1365-2664.2005.01004.x

Palucis, M. C., Ulizio, T. P., Fuller, B., & Lamb, M. P. (2018). Flow resistance, sediment transport, and bedform development in a steep gravel-bedded river flume. *Geomorphology*, *320*, 111–126. https://doi.org/10.1016/j.geomorph.2018.08.003

Pan, Y., Liu, X., & Yang, K. (2022). Effects of discharge on the velocity distribution and riverbed evolution in a meandering channel. *Journal of Hydrology*, *607*, 127539. https://doi.org/10.1016/j.jhydrol.2022.127539

Poff, N. L., Allan, J. D., Bain, M. B., Karr, J. R., Prestegaard, K. L., Richter, B. D., Sparks, R. E., & Stromberg, J. C. (1997). The Natural Flow Regime. *BioScience*, *47*(11), 769–784. https://doi.org/10.2307/1313099

Poole, G. C. (2002). Fluvial landscape ecology: Addressing uniqueness within the river discontinuum: Fluvial landscape ecology. *Freshwater Biology*, *47*(4), 641–660. https://doi.org/10.1046/j.1365-2427.2002.00922.x

Powell, D. M. (2014). Flow resistance in gravel-bed rivers: Progress in research. *Earth-Science Reviews*, *136*, 301–338. https://doi.org/10.1016/j.earscirev.2014.06.001

Qin, X., Motley, M., Leveque, R., Gonzalez, F., & Mueller, K. (2018). A comparison of a two-dimensional depth-averaged flow model and a three-dimensional RANS model for predicting tsunami inundation and fluid forces. *Natural Hazards and Earth System Sciences*, *18*(9), 2489–2506. https://doi.org/10.5194/nhess-18-2489-2018

Rhoads, B. L. (2020). *River Dynamics: Geomorphology to Support Management* (1st ed.). Cambridge University Press. https://doi.org/10.1017/9781108164108

Roache, P. J. (1998). *Verification and validation in computational science and engineering*. Hermosa Publishers.

Rodriguez, J. F., Bombardelli, F. A., García, M. H., Frothingham, K. M., Rhoads, B. L., & Abad, J. D. (2004). High-resolution numerical simulation of flow through a highly sinuous river reach. *Water Resources Management*, *18*(3), 177–199. https://doi.org/10.1023/B:WARM.0000043137.52125.a0

Rouse, H. (1978). *Elementary mechanics of fluids*. Dover Publications.

Rozovskii, I. L. (1957). *Flow of water in bends of open channels*. The Academy of Sciences of the Ukranian SSR.

Rüther, N., & Olsen, N. R. B. (2007). Modelling free-forming meander evolution in a laboratory channel using three-dimensional computational fluid dynamics. *Geomorphology*, *89*(3–4), 308–319. https://doi.org/10.1016/j.geomorph.2006.12.009

Saghebian, S. M., Roushangar, K., Ozgur Kirca, V. S., & Ghasempour, R. (2020). Modeling total resistance and form resistance of movable bed channels via experimental data and a kernel-based approach. *Journal of Hydroinformatics*, *22*(3), 528–540. https://doi.org/10.2166/hydro.2020.094

Schumm, S. A., & Khan, H. R. (1971). Experimental study of channel patterns. *Nature*, *233*, 407–409.

Schwenk, J., & Foufoula-Georgiou, E. (2016). Meander cutoffs nonlocally accelerate upstream and downstream migration and channel widening. *Geophysical Research Letters*, *43*(24). https://doi.org/10.1002/2016GL071670

Shaheed, R., Mohammadian, A., & Yan, X. (2021). A Review of Numerical Simulations of Secondary Flows in River Bends. *Water*, *13*(7), 884. https://doi.org/10.3390/w13070884

Shimizu, Y., Nelson, J., Arnez Ferrel, K., Asahi, K., Giri, S., Inoue, T., Iwasaki, T., Jang, C., Kang, T., Kimura, I., Kyuka, T., Mishra, J., Nabi, M., Patsinghasanee, S., & Yamaguchi, S. (2020). Advances in computational morphodynamics using the International River Interface Cooperative (iRIC) software. *Earth Surface Processes and Landforms*, *45*(1), 11–37. https://doi.org/10.1002/esp.4653

Shinneeb, A.-M., Nasif, G., & Balachandar, R. (2021). Effect of the aspect ratio on the velocity field of a straight open-channel flow. *Physics of Fluids*, *33*(8), 085110. https://doi.org/10.1063/5.0057343

Singer, M. B. (2010). Transient response in longitudinal grain size to reduced gravel supply in a large river: TRANSIENT RESPONSE IN GRAIN SIZE. *Geophysical Research Letters*, *37*(18), n/a-n/a. https://doi.org/10.1029/2010GL044381

Sisinggih, D., Wahyuni, S., & Rasyid, A. (2021). Flow and sediment transport in a sharp river bend using a 3D-RANS model. *IOP Conference Series: Earth and Environmental Science*, *930*(1), 012033. https://doi.org/10.1088/1755-1315/930/1/012033

Slater, L. J., Khouakhi, A., & Wilby, R. L. (2019). River channel conveyance capacity adjusts to modes of climate variability. *Scientific Reports*, *9*(1), 12619. https://doi.org/10.1038/s41598-019-48782-1

Slater, L. J., & Singer, M. B. (2013). Imprint of climate and climate change in alluvial riverbeds: Continental United States, 1950-2011. *Geology*, *41*(5), 595–598. https://doi.org/10.1130/G34070.1

Slater, L. J., Singer, M. B., & Kirchner, J. W. (2015). Hydrologic versus geomorphic drivers of trends in flood hazard. *Geophysical Research Letters*, *42*(2), 370–376. https://doi.org/10.1002/2014GL062482

Song, C. G., Seo, I. W., & Kim, Y. D. (2012). Analysis of secondary current effect in the modeling of shallow flow in open channels. *Advances in Water Resources*, *41*, 29–48. https://doi.org/10.1016/j.advwatres.2012.02.003

Song, T., & Graf, W. H. (1994). Non-uniform open-channel flow over a rough bed. *Journal of Hydroscience and Hydraulic Engineering*, *12*(1), 1–25.

Stover, S. C., & Montgomery, D. R. (2001). Channel change and flooding, Skokomish River, Washington. *Journal of Hydrology*, *243*(3–4), 272–286. https://doi.org/10.1016/S0022-1694(00)00421-2

Suzuki, Kimura, I., Shimizu, Y., Iwasaki, T., & Hosoda, T. (2014). Numerical study on secondary currents of the second kind in wide shallow open channel flows. *Proceedings of River Flow 2014*, 179–187.

Takakua, Y., & Fukuoka, S. (2020). *Three-dimensional flow structures of straight rough-bed channels with different aspect ratios*. River Flow 2020.

Termini, D. (2009a). Experimental Observations of Flow and Bed Processes in Large-Amplitude Meandering Flume. *Journal of Hydraulic Engineering*, *135*(7), 575–587. https://doi.org/10.1061/(ASCE)HY.1943-7900.0000046

Termini, D. (2009b). Experimental Observations of Flow and Bed Processes in Large-Amplitude Meandering Flume. *Journal of Hydraulic Engineering*, *135*(7), 575–587. https://doi.org/10.1061/(asce)hy.1943-7900.0000046

Tominaga, A., Nezu, I., Ezaki, K., & Nakagawa, H. (1989). Three-dimensional turbulent structure in straight open channel flows. *Journal of Hydraulic Research*, *27*(1), 149–173. https://doi.org/10.1080/00221688909499249

Uchida, T. (2018). An Enhanced Depth-integrated Model for Flows over a Negative Step with Hydraulic Jump. *E3S Web of Conferences*, *40*, 05017. https://doi.org/10.1051/e3sconf/20184005017

Uchida, T., Akamatsu, Y., Suzuki, Y., Moriguchi, S., Oikawa, Y., Shirahata, H., & Izumi, N. (2021). Special issue on the heavy rain event of July 2018 in western Japan. *Journal of Japan Society of Civil Engineers*, *9*(1), 1–7. https://doi.org/10.2208/JOURNALOFJSCE.9.1_1

Uchida, T., & Fukuoka, S. (2014). Numerical calculation for bed variation in compound-meandering channel using depth integrated model without assumption of shallow water flow. *Advances in Water Resources*, *72*, 45–56. https://doi.org/10.1016/j.advwatres.2014.05.002

Uchida, T., & Fukuoka, S. (2015). A NEW CALCULATION METHOD FOR LOCAL THREE DIMENSIONAL FLOWS BY USING THE NON-HYDROSTATIC DEPTH INTEGRATED MODEL (BVC METHOD) WITH DYNAMIC WALL-LAW FOR ROUGH BED. *Journal of Japan Society of Civil Engineers, Ser. B1 (Hydraulic Engineering)*, *71*(2), 43–62. https://doi.org/10.2208/jscejhe.71.43

Uchida, T., & Fukuoka, S. (2019). Quasi-3D two-phase model for dam-break flow over movable bed based on a non-hydrostatic depth-integrated model with a dynamic rough wall law. *Advances in Water Resources*, *129*, 311–327. https://doi.org/10.1016/j.advwatres.2017.09.020

Uchida, T., Fukuoka, S., & Ishikawa, T. (2014). 2D numerical computation for flood flow in upper river basin with tributary inflows by using water level hydrographs observed at the main stream. *Journal of Flood Risk Management*, *7*, 81–88.

Uchida, T., Fukuoka, S., Papanicolaou, A. (Thanos) N., & Tsakiris, A. G. (2016). Nonhydrostatic Quasi-3D Model Coupled with the Dynamic Rough Wall Law for Simulating Flow over a Rough Bed with Submerged Boulders. *Journal of Hydraulic Engineering*, *142*(11), 04016054. https://doi.org/10.1061/(ASCE)HY.1943-7900.0001198

Uijttewaal, W. S. J. (2014). Hydrodynamics of shallow flows: Application to rivers. *Journal of Hydraulic Research*, *52*(2), 157–172. https://doi.org/10.1080/00221686.2014.905505

Van Balen, W., Blanckaert, K., & Uijttewaal, W. S. J. (2010). Analysis of the role of turbulence in curved open-channel flow at different water depths by means of experiments, LES and RANS. *Journal of Turbulence*, *11*, N12. https://doi.org/10.1080/14685241003789404

Van Balen, W., Uijttewaal, W. S. J., & Blanckaert, K. (2009). Large-eddy simulation of a mildly curved open-channel flow. *Journal of Fluid Mechanics*, *630*, 413–442. https://doi.org/10.1017/S0022112009007277

Vasquez, J. A., Millar, R. G., & Steffler, P. M. (2006). Vertically-averaged and moment of momentum model for alluvial bend morphology. *River,Coastal and Estuarine Morphodynamics:RCEM 2005*, 711–718.

Vasquez, J. A., Millar, R. G., & Steffler, P. M. (2011). Vertically-averaged and moment model for meandering river morphology. *Canadian Journal of Civil Engineering*, *38*(8), 921–931. https://doi.org/10.1139/l11-063

Vasquez, J. A., Steffler, P. M., & Millar, R. G. (2008). Modeling Bed Changes in Meandering Rivers Using Triangular Finite Elements. *Journal of Hydraulic Engineering*, *134*(9), 1348–1352. https://doi.org/10.1061/(ASCE)0733-9429(2008)134:9(1348)

Vinuesa, R., Schlatter, P., & Nagib, H. M. (2018). Secondary flow in turbulent ducts with increasing aspect ratio. *Physical Review Fluids*, *3*(5), 054606. https://doi.org/10.1103/PhysRevFluids.3.054606

Wang, S. S. Y., Roache, P. J., Schmalz, R. A., Jia, Y., & Smith, P. E. (2009). Verification and validation of 3D free-surface flow models. In *Verification and Validation of 3D Free-Surface Flow Models*. https://doi.org/10.1061/9780784409572

Wang, Z.-Q., & Cheng, N.-S. (2006). Time-mean structure of secondary flows in open channel with longitudinal bedforms. *Advances in Water Resources*, *29*(11), 1634–1649. https://doi.org/10.1016/j.advwatres.2005.12.002

Watanabe, A., Fukuoka, S., Mutasingwa, A. G., & Ota, M. (2002). The unsteady 2D flow analysis on the deformation of hydrograph and the flood flow storage in compound meandering channels. *PROCEEDINGS OF HYDRAULIC ENGINEERING*, *46*, 427–432. https://doi.org/10.2208/prohe.46.427

Whiting, P. J., & Dietrich, W. E. (1993a). Experimental studies of bed topography and flow patterns in large-amplitude meanders: 1. Observations. *Water Resources Research*, *29*(11), 3605–3614. https://doi.org/10.1029/93WR01756

Whiting, P. J., & Dietrich, W. E. (1993b). Experimental studies of bed topography and flow patterns in large-amplitude meanders: 2. Mechanisms. *Water Resources Research*, *29*(11), 3615–3622. https://doi.org/10.1029/93WR01756

Wu, W. (2004). Depth-Averaged Two-Dimensional Numerical Modeling of Unsteady Flow and Nonuniform Sediment Transport in Open Channels. *Journal of Hydraulic Engineering*, *130*(10), 1013–1024. https://doi.org/10.1061/(ASCE)0733-9429(2004)130:10(1013)

Wu, W. (2008). *Computational river dynamics*. Taylor & Francis.

Wu, W., Rodi, W., & Wenka, T. (2000). 3D numerical modeling of flow and sediment transport in open channels. *Journal of Hydraulic Engineering*, *126*(1), 4–15.

Yagi, F., Uchida, T., & Kawahara, Y. (2022). NUMERICAL INVESTIGATION OF THREE-DIMENSIONAL FLOW STRUCTURES AND TURBULENCE ENERGY DISTRIBUTIONS IN BANK EROSION REACHES DURING LARGE FLOOD EVENTS. *Journal of JSCE*, *10*(1), 136–144. https://doi.org/10.2208/journalofjsce.10.1_136

Yan, X., Rennie, C. D., & Mohammadian, A. (2020). A three-dimensional numerical study of flow characteristics in strongly curved channel bends with different side slopes. *Environmental Fluid Mechanics*, *20*(6), 1491–1510. https://doi.org/10.1007/s10652-020-09751-9

Yang, S.-Q., Tan, S. K., & Wang, X.-K. (2012). Mechanism of secondary currents in open channel flows: SECONDARY CURRENTS, SAND RIDGES, FLOWS. *Journal of Geophysical Research: Earth Surface*, *117*(F4), n/a-n/a. https://doi.org/10.1029/2012JF002510

Ye, J., & McCorquodale, J. A. (1997). Depth-Averaged Hydrodynamic Model in Curvilinear Collocated Grid. *Journal of Hydraulic Engineering*, *123*(5), 380–388. https://doi.org/10.1061/(ASCE)0733-9429(1997)123:5(380)

Ye, J., & McCorquodale, J. A. (1998). Simulation of curved open channel dlows by 3D hydrodynamic model. *Journal of Hydraulic Engineering*, *124*(7), 687–698. https://doi.org/10.1061/(asce)0733-9429(1998)124:7(687)

Yeh, K., & Kennedy, J. F. (1993). Moment Model of Nonuniform Channel-Bend Flow. II: Erodible Beds. *Journal of Hydraulic Engineering*, *119*(7), 796–815. https://doi.org/10.1061/(ASCE)0733-9429(1993)119:7(796)

Yen, B. C. (2002). Open Channel Flow Resistance. *Journal of Hydraulic Engineering*, *128*(1), 20–39. https://doi.org/10.1061/(ASCE)0733-9429(2002)128:1(20)

Zeng, J., Constantinescu, G., Blanckaert, K., & Weber, L. (2008). Flow and bathymetry in sharp open-channel bends: Experiments and predictions: FLOW AND BATHYMETRY IN SHARP OPEN-CHANNEL BENDS. *Water Resources Research*, *44*(9). https://doi.org/10.1029/2007WR006303

Zeng, J., Constantinescu, G., & Weber, L. (2008). A 3D non-hydrostatic model to predict flow and sediment transport in loose-bed channel bends. *Journal of Hydraulic Research*, *46*(3), 356–372. https://doi.org/10.3826/jhr.2008.3328

Zhang, H.-T., Dai, W.-H., Da Silva, A. M. F., & Tang, H.-W. (2022). Numerical Study on Resistance to Flow in Meandering Channels. *Journal of Hydraulic Engineering*, *148*(2), 04021059. https://doi.org/10.1061/(ASCE)HY.1943-7900.0001946